Distributed Six-Port Reflectometer Based Vector Network Analyzer with Multiple Measurement Techniques and Applications for Microwave Imaging

Muhammad Hashir

A Thesis submitted to the Faculty of Graduate Studies of
The University of Manitoba
for the partial fulfillment of the requirements of the degree of

Master of Science

Department of Electrical and Computer Engineering
University of Manitoba
Winnipeg, Manitoba, Canada

Abstract

This thesis presents the design and measurement of a distributed six-port reflectometer-based vector network analyzer. The design has been proven to operate with two independent RF power sources. This novel approach makes our system the first-of-its-kind in the world having the capability for accurate phase measurements of distant antennas and other devices which previously required long coaxial cables incurring high-cost and loss of accuracy due to resulting long cable losses. The specific distributed network analyzer reported on herein has a bandwidth of 0.6-1.2 GHz. The study also evaluates three characterization-based measurement techniques, and two calibration-based measurement techniques reported in the literature and draws a comparison based on their performance when used with the current hardware. A test case has been proven for applications of the current hardware to measure the path characteristics in Microwave Imaging applications. A novel approach for determining the reflection and transmission coefficients of the device under test (DUT) has been introduced and validated, utilizing two characterization-based techniques based on non-linear optimization and a geometrical solution. The results were confirmed using a simulation software (ADS) as well as full experimental results using a custom-built measurement hardware. The novel approach allows accurate S-parameter measurements while increasing computational efficiency and using a lesser number of calibration loads as compared to many previously proposed techniques. Although measurement techniques requiring the full S-parameters of the six-port circuit as well as those not requiring the full S-parameters have been tested, our study found that the characterization-based techniques using S-parameters to be more accurate when performed using our custom measurement hardware.

Acknowledgments

I would like to thank my supervisors Prof. Joe LoVetri and Prof. Colin Gilmore for all the support and guidance throughout my research. Their unwavering encouragement in times of need is something that would last with me forever. I would also like to thank them for letting me explore opportunities outside the lab such as my Lab2Market internship and Mitacs Accelerate internship along with the grant for funding my degree.

I express my gratitude towards the examining committee Prof. Puyan Mojabi and Prof. Dustin Isleifson for their valuable time and feedback. Also, Prof. Gregory Bridges for letting me use his equipment and the beneficial insights. Saif Aboud played a vital role in my initial work by providing his hardware and explaining his approach towards the related work he did, so I am indebted to him for this support.

I would like to express my gratitude for my lab members Amir Attar, Seth Cathers, Lucas Banting, Ben Martins and Vijaya Channa for making this journey memorable. I would also appreciate University of Manitoba for the IGSE scholarship and all the support during the research.

Lastly, I want to thank my friends and family without which none of this would have been possible.

Contents

List of Abbreviations:

I2C: Inter-Integrated Circuit (Serial Communication Bus)

DUT: Device under test

DSPR-VNA: Distributed Six-port Reflectometer based Vector Network Analyzer

RF: Radio Frequency

SPR: Six-Port Reflectometer

SPC: Six-Port Circuit

VNA: Vector Network Analyzer

PCB: Printed Circuit Board

List of Figures

1 Introduction:

This chapter provides the motivation and the key contributions along with an overview of the research that was conducted.

1.1 Motivation:

In the rapidly evolving landscape of RF and microwave technologies, accurate characterization of multi-port networks is very important because it allows us to design, analyze and configure these systems. The Vector Network Analyzer (VNA) is the standard measurement tool used for characterizing multi-port networks. It is a microwave transceiver that analyzes both the amplitude and phase of transmitted and reflected waves at the ports of a microwave network. These waves are represented by incident and reflected voltage waves, and the relationship between these waves is characterized by the scattering parameters of the system [1]. Typically, cables are used to provide the VNA access to the ports of the device-under-test (DUT). These not only provide access to the ports but also facilitate the phase synchronization required so as to obtain accurate magnitude and phase measurements. However, this method of accessing the ports is particularly inconvenient when the ports of multi-port systems, such as the ports on imaging chambers used in biomedical and food storage monitoring, are long distance apart. The primary issues arise from the losses and noise introduced into the system by the cables.

In the 1970's, researchers proposed the use of six-port-reflectometer (SPR) to measure the S-parameters of a DUT. These techniques only require power detectors to measure the power at particular ports but from these measurements one can obtain both the magnitude and phase of the S-parameters as can be obtained using a conventional VNA [5], [6]. Since the original work done on SPR’s in the 1970s [6], improvements have been made to make such systems compact, robust and with an increasing bandwidth. Researchers [4] also outlined how two SPRs can be combined to obtain measurements of through-parameters, e.g. S21 (not just reflections, S11), these devices have been referred to as Six-port Network Analyzers (SPNA) in the literature [4] but we will refer to them as the SPR-VNA.

Some of the advantages of using six-port circuits to make S-parameter measurements include:

- Simplicity of microwave hardware which ensures long-term operational stability and less need for frequent calibration, which is beneficial for integrated devices.
- Customization for specific application needs and ability to be designed as specific sensors.
- No Requirement for Phase-Locked signal sources at the input ports.

The development of a distributed SPR-VNA not only removes the need for a common excitation signal source but also enables the potential for multi-port measurements without the reliance on complex switching matrices. This can help make the multi-port characterization measurements low-cost.

It should be mentioned that in 2019, Aboud [2] simulated the use of independent RF sources to make a distributed six-port based network analyzer, but not having access to a hardware-based system, his approach was not verified in a practical measurement setting so he could not test and compare the different characterization and calibration techniques.

By eliminating the need for a common phase synchronized RF source at the SPRs connected with each port of a DUT, or the path we want to characterize, we open up new possibilities for long-distance transmission path measurements through a portable system.

Commercial solutions to measure such RF-paths where the two ports of the path are far apart, require extra hardware, such as fibre-optic cables connecting the two ports (which provides the required phase reference) [3]. These systems are very high cost (approximately 100,000 USD).

This thesis reports on the developed measurement hardware and analyzes the performance of various characterization techniques tried with our specific distributed six-port network analyzer. This work can be extended to other large-scale sensing applications, including grain bin moisture monitoring and biomedical imaging [2]. An important potential application of a distributed SPR-VNA is to collect S-parameters used to image moisture of grain stored within a grain. Such silos can be 40-meters in diameter [62] and the antennas which collect the S-parameters are mounted on the interior walls of the silo. Installing such an imaging system using a traditional VNA requires RF cables going to each antenna, each connected centrally to the VNA (this could mean the use of one cable per antenna , each ~60 meters long in some cases). A distributed SPR-VNA would make the same S-parameter measurements but would not require a cabled connection to each of the antennas. In fact, each antenna could be backed by a battery powered SPR-VNA device, making the whole system portable and more commercially viable. Thus, our approach offers a practical solution for distributed S-parameter measurements providing a compact and cable-free system.

1.2 Contribution:

The main contribution of this thesis is the first experimental verification of a distributed SPR-VNA for accurate S-parameter measurements. The second major contribution of this thesis is the evaluation of different calibration techniques and introducing different characterization methods based only on power measurements to find the full scattering parameters of a DUT. The use of independent RF sources for creating a six-port network analyzer has been proved for the first time in hardware. A comparative analysis based on several characterization and calibration techniques is reported. Two characterization-based approaches are tested and validated to find the reflection and transmission coefficient using the six-port network analyzer. We also apply 3 widely used calibration techniques [1],[53],[13] on our hardware, though the in-house approach of using characterization algorithms outperform the calibration techniques proposed in previous studies. The distributed SPR-VNA is successfully applied to the case of S-parameter measurements between two antennas opening up the possibilities for microwave imaging as well.

1.3 Overview

Chapter 2 describes the underlying theoretical principles of SPRs. It provides details of the mathematical foundations and fundamental equations that establish the relation between power detector measurements and the reflection coefficient at the port of a DUT measurement plane. The chapter also provides a brief history of SPR architecture designs and provides an analysis of the selected configuration.

Chapter 3 explores the theoretical aspects of Six-Port Network Analyzers (SPR-VNAs) and presents a brief literature review of SPR-VNA design topologies, all assuming a common RF source. Chapter 4 examines two prevalent calibration methodologies and discusses the utilization of multiple calibration standards. It introduces a novel approach towards characterization of the system without calibration loads using the S-parameters of the SPR. Chapter 5 focuses on simulation and hardware results of the selected six-port design and evaluates the performance of different characterization and calibration techniques, accompanied by simulation outcomes and their subsequent analysis.

Chapter 6 analyzes our hardware distributed six-port vector network analyzer (DSPR-VNA) performance, provides a comparison of the different characterization techniques, and introduces a novel approach of using time-delay in the input signals to implement the required phase shifts. It also validates the technique for and using the DSPR-VNA in microwave imaging applications.

Chapter 7 concludes the thesis, highlighting key findings and insights. It also outlines potential avenues for future research.

2 Six-Port Reflectometers:

This chapter provides the theoretical foundations, design criteria and architecture of six-port networks. It discusses the historical evolution of SPN-based reflectometers and highlights their use in the prominent application of making S-parameter measurements. In addition, a descriptive overview of several techniques used to retrieve the S-parameters of a DUT is provided. These are divided into two classes: so-called "calibration-based" techniques where the S-parameters of the SPN being used are not required, and "characterization-based" techniques where one relies on an accurate characterization of the S-parameters of the SPN.

As the literature on SPNs is wide-ranging and has evolved since the early 1970s, it is important to define the terms used for SPN-based systems. The SPR, which evolved from the 'Six-Port Correlator' [1], is a circuit comprising six-ports, with four of these ports permanently equipped with external power detectors. One port is connected to a primary RF source (a device outputting a sinusoidal wave voltage at a particular frequency), while the second port interfaces with the DUT. Through scalar power measurements at the remaining four ports of the SPR, one is able to infer the Γ_{DUT} (phase and magnitude) of the DUT connected at port two. Theoretically, a six-port circuit (sometimes referred to as a six-port junction) that is used to create a SPR can have virtually any internal topology. As later described in this thesis, SPRs are typically built using only passive components: such as co-planar waveguides or microstrip transmission lines. Thus, the key advantage of the SPR lies in its ability to determine the complex reflection coefficient of a DUT using only scalar measurements of power levels at the detector ports of a simple passive circuit.

2.1 Theoretical Analysis of Six-port Reflectometers

As shown in Figure 1 the typical six-port reflectometer consists of four power detectors attached to the four ports of the six-port circuit while the device under test is connected at another port. One port is connected with the RF source which is usually a signal generator. An *N*-port device or a microwave network can be characterized using a scattering matrix, denoted by S, which relates the incident voltage waves, when normalized are referred to as a, and the reflected voltage waves , which when normalized are referred to as b, at any particular frequency. The relationship is written in matrix form as.

$$b = Sa \tag{2.1}$$

Consider a_i are the incident normalized voltages and b_i are the reflected normalized voltages, i = 1…6. The ratio of incident to the reflected voltage waves at each port is known as reflection coefficient (Γ).

$$\Gamma_i = \frac{a_i}{b_i} \qquad \text{where } \; i = 1\ldots6 \tag{2.2}$$

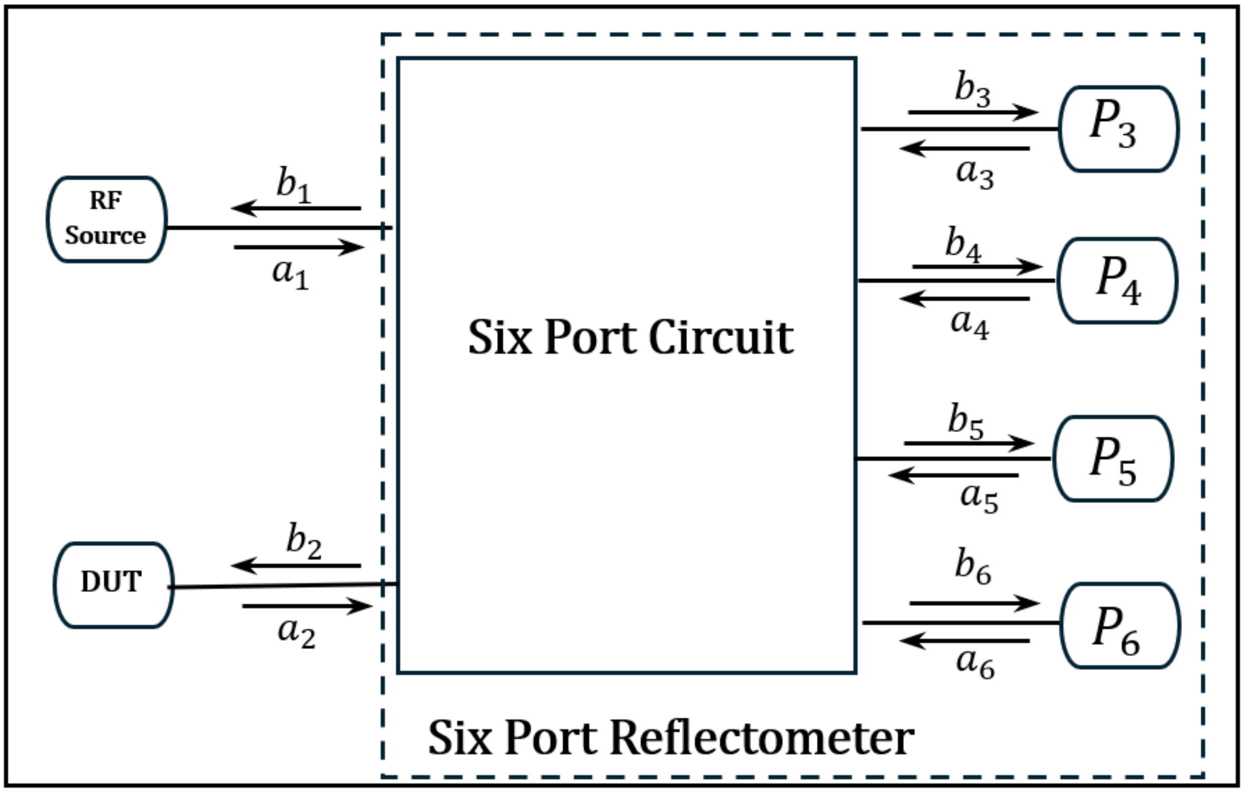

Figure 1 Block diagram of a Six-Port Reflectometer

To analyze the working of our reflectometer, we first need to consider the S-parameter matrix for our full system. Writing the full 6×6 S-parameter matrix:

$$\begin{bmatrix} b_1 \\ b_2 \\ b_3 \\ b_4 \\ b_5 \\ b_6 \end{bmatrix} = \begin{bmatrix} S_{11} & S_{12} & S_{13} & S_{14} & S_{15} & S_{16} \\ S_{21} & S_{22} & S_{23} & S_{24} & S_{25} & S_{26} \\ S_{31} & S_{32} & S_{33} & S_{34} & S_{35} & S_{36} \\ S_{41} & S_{42} & S_{43} & S_{44} & S_{45} & S_{46} \\ S_{51} & S_{52} & S_{53} & S_{54} & S_{55} & S_{56} \\ S_{61} & S_{62} & S_{63} & S_{64} & S_{65} & S_{66} \end{bmatrix} \begin{bmatrix} a_1 \\ a_2 \\ a_3 \\ a_4 \\ a_5 \\ a_6 \end{bmatrix} \tag{2.3}$$

Since we are measuring the powers at ports 3 to 6, so (2.4) explicitly states

$$b_3 = S_{31}a_1 + S_{32}a_2 + S_{33}a_3 + S_{34}a_4 + S_{35}a_5 + S_{36}a_6 \tag{2.4a}$$
$$b_4 = S_{41}a_1 + S_{42}a_2 + S_{43}a_3 + S_{44}a_4 + S_{45}a_5 + S_{46}a_6 \tag{2.4b}$$
$$b_5 = S_{51}a_1 + S_{52}a_2 + S_{33}a_3 + S_{44}a_4 + S_{55}a_5 + S_{56}a_6 \tag{2.4c}$$
$$b_6 = S_{61}a_1 + S_{62}a_2 + S_{63}a_3 + S_{64}a_4 + S_{56}a_6 + S_{66}a_6 \tag{2.4d}$$

Using the reflection coefficients at the power measurement ports (2.2) and re-arranging the equations for the voltage waves for ports 3 to 6 we get

$$0 = S_{31}a_1 + S_{32}a_2 + (S_{33}\Gamma_3 - 1)b_3 + S_{34}\Gamma_4 b_4 + S_{35}\Gamma_5 b_5 + S_{24}\Gamma_6 b_6 \quad (2.5a)$$
$$0 = S_{41}a_1 + S_{42}a_2 + S_{43}a_3 + (S_{44}\Gamma_4 - 1)b_4 + S_{45}\Gamma_5 b_5 + S_{46}\Gamma_{b6} \quad (2.5b)$$
$$0 = S_{51}a_1 + S_{52}a_2 + S_{53}a_3 + S_{54}a_4 + (S_{55}\Gamma_5 - 1)b_5 + S_{56}\Gamma_{66} \quad (2.5c)$$
$$0 = S_{61}a_1 + S_{62}a_2 + S_{63}a_3 + S_{64}a_4 + S_{55}a_5 + \ (S_{56}\Gamma_6 - 1)b_6 \quad (2.5d)$$

Now, putting these back into the full S-matrix, we have

$$\begin{bmatrix} b_1 \\ b_2 \\ 0 \\ 0 \\ 0 \\ 0 \end{bmatrix} = \begin{bmatrix} S_{11} & S_{12} & S_{13}\Gamma_3 & S_{14}\Gamma_4 & S_{15}\Gamma_5 & S_{16}\Gamma_6 \\ S_{21} & S_{22} & S_{23}\Gamma_3 & S_{24}\Gamma_4 & S_{25}\Gamma_5 & S_{26}\Gamma_6 \\ S_{31} & S_{32} & S_{33}\Gamma_3 - 1 & S_{34}\Gamma_4 & S_{35}\Gamma_5 & S_{36}\Gamma_6 \\ S_{41} & S_{42} & S_{43}\Gamma_3 & S_{44}\Gamma_4 - 1 & S_{45}\Gamma_5 & S_{46}\Gamma_6 \\ S_{51} & S_{52} & S_{53}\Gamma_3 & S_{54}\Gamma_4 & S_{55}\Gamma_5 - 1 & S_{56}\Gamma_6 \\ S_{61} & S_{62} & S_{63}\Gamma_3 & S_{64}\Gamma_4 & S_{65}\Gamma_5 & S_{66}\Gamma_6 - 1 \end{bmatrix} \begin{bmatrix} a_1 \\ a_2 \\ b_3 \\ b_4 \\ b_5 \\ b_6 \end{bmatrix} \quad (2.6)$$

Eq. 2.6 forms the starting point of how performing four power measurements at ports 3-6 can be used to measure the reflection coefficient at port 2. Let's call the matrix defined in (2.6), $\overline{S}$. There are two cases [5], [4] considered in the literature, those assuming that the power detectors at port 3-6 are perfectly matched so $\Gamma_{3\cdots6} = 0$, or those wherein no assumption is made regarding the power detectors at port 3-6, they are not assumed to be matched so $\Gamma_{3\cdots6} \neq 0$. Both cases are discussed in Section 2.2 and Section 2.3.

2.2 Derivation of Six-Port Procedure for Perfectly Matched Power Detectors

The approach that is now described was originally proposed by Hoer[6]. First, we express the power absorbed at each port as

$$P_i = |b_i|^2 - |a_i|^2 \quad (2.7)$$

Since we are considering matched ports, $a_i = 0$, we can write (2.7) as

$$P_i = |b_i|^2 \tag{2.8}$$

The parameters we measure are $|b_i|^2$ and our ultimate desire is to use these power measurements to find $\Gamma_2 = \frac{a_2}{b_2}$. Therefore, the goal is to build a relationship between Γ_2 and $|b_i|^2$ using (2.6).

For the case of matched ports $\Gamma_{3\ldots6} = 0$, (2.6) can be written as

$$\begin{bmatrix} b_1 \\ b_2 \\ 0 \\ 0 \\ 0 \\ 0 \end{bmatrix} = \begin{bmatrix} S_{11} & S_{12} & 0 & 0 & 0 & 0 \\ S_{21} & S_{22} & 0 & 0 & 0 & 0 \\ S_{31} & S_{32} & -1 & 0 & 0 & 0 \\ S_{41} & S_{42} & 0 & -1 & 0 & 0 \\ S_{51} & S_{52} & 0 & 0 & -1 & 0 \\ S_{61} & S_{62} & 0 & 0 & 0 & -1 \end{bmatrix} \begin{bmatrix} a_1 \\ a_2 \\ b_3 \\ b_4 \\ b_5 \\ b_6 \end{bmatrix} \tag{2.9}$$

From which we get the following equations, where $i = 3{,}4{,}5{,}6$

$$b_1 = S_{11}\, a_1 + S_{12}\, a_2 \tag{2.10}$$
$$b_2 = S_{21}\, a_1 + S_{22}\, a_2 \tag{2.11}$$
$$b_{i=3..6} = S_{i1}\, a_1 + S_{\mathrm{i}2} a_2 \tag{2.12}$$

By isolating a_1 in (2.11), and then placing a_1 into (2.12) we get

$$b_i = S_{i1}\left(\frac{b_2 - S_{22}a_2}{S_{21}}\right) + (S_{i2})a_2 \tag{2.13}$$

$$b_i = \frac{S_{i1}}{S_{21}} b_2 - \frac{S_{i1}S_{22}a_2}{S_{21}} + S_{i2}a_2 \tag{2.14}$$

$$b_i = \left(\frac{S_{i1}}{S_{21}}\right) b_2 + \left(\frac{-S_{i1}S_{22} + S_{i2}S_{21}}{S_{21}}\right) a_2 \tag{2.15}$$

We can define $A_i = \left(\frac{S_{i1}}{S_{21}}\right)$ and $B_i = \frac{-S_{i1}S_{22}+S_{i2}S_{21}}{S_{21}}$ and write (2.15) in the following form:

$$b_i = A_i b_2 + B_i a_2 \tag{2.16}$$

Noting that the square of the absolute value of the b_i is equal to the measured power, from (2.8), (2.16) can be written as

$$|b_i|^2 = |A_i b_2 + B_i a_2|^2 \tag{2.17}$$

It is typical in the design of SPRs to isolate one of the power measurement ports from the remaining power measurement ports. Usually, port 3 is designed as the reference port. The powers measured at this port P_3 represents the property of the SPR and does not dependent on the DUT. Thus P_3 is used to normalize powers at ports 4,5,6 and allows us to obtain three power independent equations [14]. Using these normalized powers we write (2.17) as

$$\frac{P_i}{P_3} = \frac{|A_i b_2 + B_i a_2|^2}{|A_3 b_2 + B_3 a_2|^2} \tag{2.18}$$

Dividing all terms by b_2 in (2.18) we can write

$$\frac{P_i}{P_3} = \frac{|A_i + B_i \Gamma_L|^2}{|A_3 + B_3 \Gamma_L|^2} \tag{2.19}$$

where the reflection coefficient at port 2 is, $\Gamma_L = \frac{a_2}{b_2}$, and is the unknown we are interested in finding. So we can write (2.19) as

$$\frac{P_i}{P_3} = \frac{|B_i|^2}{|B_3|^2} \left| \frac{\frac{A_i}{B_i} + \Gamma_L}{\frac{A_3}{B_3} + \Gamma_L} \right|^2 \tag{2.20}$$

We can further simplify our equations by introducing four complex constants q_i for *i=3…6* and three real constants M_i for *i=4…6* to get

$$q_i = \frac{-A_i}{B_i} = \frac{-S_{i1}}{S_{i2}S_{21} - S_{i1}S_{22}} \qquad (2.21)$$

and

$$M_i = \frac{|B_i|^2}{|B_3|^2} \qquad (2.22)$$

We can write (2.20) as

$$\frac{P_i}{P_3 M_i} = \frac{|\Gamma_L - q_i|^2}{|\Gamma_L - q_3|^2} \qquad (2.23)$$

Let $k_i = \frac{P_i}{P_3 M_i}$, a scalar, we can write (2.23) as

$$|\Gamma_L - q_3|^2 k_i = |\Gamma_\mathrm{L} - q_i|^2 \qquad i=4\ldots6 \qquad (2.24)$$

As will be described Section 2.4 , Equation (2.24) can be manipulated and written as an equation of a circle in the complex Γ_L plane. That is, three circles, the intersection of which determines the correct Γ_L. This is a nonlinear mathematical problem that we must solve. Since there will inevitably be noise in the power measurements it can become a difficult nonlinear optimization problem to find theΓ_L. But notice that the variables q_i depend only on the S-parameters of the SPR and therefore can be controlled by appropriate design of the SPR, independent of the DUT that will be measured. The non-linear optimization algorithms that will be discussed in the subsequent parts of this thesis will differ with respect to their sensitivity to the input measurements. That is, different ways of solving these equations can lead to different answers. We discuss different methods of finding gamma in Chapter 5.

2.3 Derivation of Six-Port Procedure for Unmatched Power Detectors

In this Section we follow the approach proposed by Ghannouchi et al. and Mohammadi [4] . Considering our ports connected with the power meters are not matched, we solve (2.6) by first inverting the matrix $\bar{S}$. The inverse of the 6x6 $\bar{S}$-matrix in (2.6) gives us similar equations to (2.10 – 2.12) as

$$a_1 = m_{11}b_1 + m_{12}b_2 \quad (2.25)$$
$$a_2 = m_{21}b_1 + m_{22}b_2 \quad (2.26)$$
$$b_{\mathrm{i}\,=\,3..6} = m_{\mathrm{i}1}b_1 + m_{\mathrm{i}2}b_2 \quad (2.27)$$

where m_{ij} are the entries of the inverse matrix. Take b_1 out from (2.27), we get

$$b_1 = \frac{b_i - m_{i2}b_2}{m_{i1}} \quad (2.28)$$

Taking b_2 out from (2.25) and (2.26) gives

$$\frac{a_1 - m_{11}b_1}{m_{12}} = b_2 \quad (2.29)$$

and

$$\frac{a_2 - m_{21}b_1}{m_{22}} = b_2 \quad (2.30)$$

Subtracting (2.29) from (2.30) we get

$$\frac{a_1 - m_{11}b_1}{m_{12}} - \frac{a_2 + m_{21}b_1}{m_{22}} = 0 \quad (2.31)$$

$$a_1m_{22} - m_{11}m_{22}b_1 - a_2m_{12} - m_{21}m_{12}b_1 = 0 \quad (2.32)$$

Replacing a_1 in (2.32) with (2.25) we get

$$(m_{11}b_1 + m_{12}b_2)m_{22} - m_{11}m_{22}b_1 - a_2m_{12} \ - m_{21}m_{12}b_1 = 0 \tag{2.33}$$

$$m_{12}m_{22}b_2 - a_2m_{12} - m_{21}m_{12}b_1 = 0 \tag{2.34}$$

Replacing b_1 in (2.34) with (2.28) we get

$$m_{12}b_2m_{22} - a_2m_{12} - m_{21}m_{12}\left(\frac{b_i - m_{i2}b_2}{m_{i1}}\right) = 0 \tag{2.35}$$

Solving (2.35) for b_{i}:

$$\frac{m_{12}m_{21}b_i}{m_{i1}} = \frac{m_{\mathrm{i}2}m_{21}m_{12}b_2}{m_1} + a_2m_{12} - m_{12}b_2m_{22} \tag{2.36}$$

Simplifying (2.36) we get

$$b_i = m_{\mathrm{i}2}b_2 + \frac{a_2m_{\mathrm{i}1}}{m_{21}} - \frac{m_{22}b_2m_{\mathrm{i}1}}{m_{21}} \tag{2.37}$$

Taking common $\frac{m_{\mathrm{i}1}}{m_{21}}b_2$ in (2.37)

$$b_i = \frac{m_{\mathrm{i}1}}{m_{21}}b_2\left(-m_{22} + \frac{a_2}{b_2} + \frac{m_{i2}m_{21}}{m_{i1}}\right) \tag{2.38}$$

Let $B_i = \frac{m_{i1}}{m_{21}}$ and $\Gamma_2 = \frac{a_2}{b_2}$ $\ and\ q_i = \frac{m_{\mathrm{i}2}m_{21}}{m_{i1}} - m_{22}$ we can write $-q_i = \frac{-m_{22}m_{i1}+m_{\mathrm{i}2}m_{21}}{m_{i1}}$

Substituting in (2.38) we get:

$$b_i = B_i(\Gamma_2 - q_i)b_2 \tag{2.39}$$

We can obtain a simplified set of equations by defining four complex constants q_i for *i=3…6* and three real constants M_i for *i=4…6*.

$$-q_i = \frac{A_i}{B_i} \Rightarrow q_i = \frac{-A_i}{B_i} \tag{2.40}$$

Plugging in the formulas for '*q*' and '*B*' we can drive an expression for '*A*' in terms of 'm':

$$A = -qB \ = \ \frac{-m_{22}m_{11}+m_{i2}m_{21}}{m_{i1}} \times \frac{m_{i1}}{m_{21}} \tag{2.41}$$

$$\mathrm{A} \ = \frac{-m_{22}m_{i1}}{m_{21}} + m_{i2} \tag{2.42}$$

Using (2.8) we can write (2.39) as

$$\frac{P_i}{P_3} = \frac{|b_i|^2}{|b_3|^2} = \frac{|B_i|^2(\Gamma_2 - q_i)^2 b_2}{|B_3|^2|\Gamma_2 - q_3|^2 b_2} \tag{2.43}$$

Letting $M_i = \frac{|B_i|^2}{|B_3|^2}$, (2.43) becomes,

$$\frac{P_i}{P_3 M_i} = \frac{|\Gamma_2 - q_i|^2}{|\Gamma_2 - q_3|^2} \tag{2.44}$$

Defining $k_i = \frac{P_i}{P_3 M_i}$ we get the equation

$$|\Gamma_2 - q_3|^2 k_i = |\Gamma_2 - q_i|^2 \tag{2.45}$$

We can observe that this is same as (2.24) and, as we suggested previously, we can manipulate it to find the equations of the circles. Details of this manipulation are discussed in Section 2.4. Note that here we have used the same variables as in the previous case that is applicable only to the case of matched power detectors. No confusion should arise as the context will make clear which variable definitions we are using. Also note that, this case which utilizes $\bar{S}$ is also applicable to the matched detector case.

2.4 Geometrical Derivation of Circles

So far we have derived the equations representing the SPR in the form of powers at the ports and S-parameter dependent variables in Section 2.2 (matched ports) and Section 2.3 (unmatched ports). We can now interpret equations (2.24) or (2.45) as the equations of circles in the Γ_L-plane. Rewriting these here:

$$|\Gamma_2 - q_3|^2 k_i = |\Gamma_2 - q_i|^2 \text{ , } i = 4,5,6$$

We know the algebraic formula:

$$|x - y|^2 = x^* x + y^* y - x y^* - x^* y \tag{2.46}$$

Using the formula in (2.46) to expand our equation, we get:

$$(\Gamma_2^* \Gamma_2 + q_3^* q_3 - \Gamma_2 q_3^* - \Gamma_2^* q_3) k_i = \Gamma_2^* \Gamma_2 + q_i q_i^* - \Gamma_2^* q_i - \Gamma_2 q_i^* \tag{2.47a}$$

$$\Gamma_2^* \Gamma_2 (k_i - 1) + k_i (q_3^* q_3) - q_i q_i^* + \Gamma_2 (q_\mathrm{i}^* - q_3^* k_i) + \Gamma_2^* (q_\mathrm{i} - q_3 k_i) = 0 \tag{2.47b}$$

$$|\Gamma_2|^2 (k_i - 1) + k_i |q_3|^2 - |q_i|^2 + \Gamma_2 (q_\mathrm{i}^* - q_3^* k_i) + \Gamma_2^* (q_\mathrm{i} - q_3 k_i) = 0 \tag{2.47c}$$

$$|\Gamma_2|^2 - \Gamma_2 \left(\frac{q_3^* k_i - q_\mathrm{i}^*}{k_i - 1} \right) - \Gamma_2^* \left(\frac{q_3 k_i - q_i}{k_i - 1} \right) + \frac{k_i |q_3|^2 - |q_i|^2}{k_i - 1} = 0 \tag{2.47d}$$

The standard equation of a circle in the complex plane can be written as: $|z - c|^2 = R^2$

$$z z^* + c c^* - z c^* - z^* c = R^2 \tag{2.48}$$

Comparing (2.47d) with (2.48) we know that the center is

$$C_{i=4..6} = \frac{q_3 k_i - q_i}{k_i - 1} \tag{2.49}$$

To get the radius, we again compare (2.47d) with (2.48)

$$R_i{}^2 - cc^* = \frac{|q_i|^2 - k_i|q_3|^2}{k_i - 1} \tag{2.50}$$

$$R_i{}^2 = \frac{|q_i|^2 - k_i|q_3|^2}{k_i - 1} + \frac{|q_3 k_i - q_i|^2}{|k_i - 1|^2} \tag{2.51}$$

$$R_i{}^2 = \frac{1}{|k_i - 1|^2}[(|q_i|^2 - k_i|q_3|^2)(k_i - 1) + |q_3 k_i - q_i|^2] \tag{2.52}$$

$$R_i{}^2 = \frac{1}{|k_i - 1|^2}[|q_i|^2 k_i - |q_i|^2 - k_i^2|q_3|^2 + k_i|q_3|^2 + |q_3|^2 k_i^2 + |q_i|^2 - q_3 q_i^* k_i - q_3 k_i^* q_i \tag{2.53}$$

$$R_i{}^2 = \frac{k_i}{|k_i - 1|^2}\left[\left|q_i\right|^2 + \left|q_3\right|^2 - q_3 k_i q_i^* - q_3^* k_i^* q_i\right] \tag{2.54}$$

$$R_i{}^2 = \frac{k_i}{|k_i - 1|^2}\left|q_i - q_3\right|^2 \tag{2.55}$$

$$R_{i=4..6} = \frac{\sqrt{k_i}}{|k_i - 1|}|q_i - q_3| \tag{2.55a}$$

$$|\Gamma_{DUT} - C_i|^2 = R_{i=4..6}{}^2 \tag{2.56}$$

Hence, we have derived the radii and centers of the 3 circles in the complex Γ plane. Theoretically their common point of intersection defines the reflection coefficient Γ_{DUT} in the complex plain if a termination with Γ_{DUT} is connected with the SPR, details of which are in Section 4.1. Figure 2 shows the intersection of the 3 circles for an ideal six-port reflectometer.

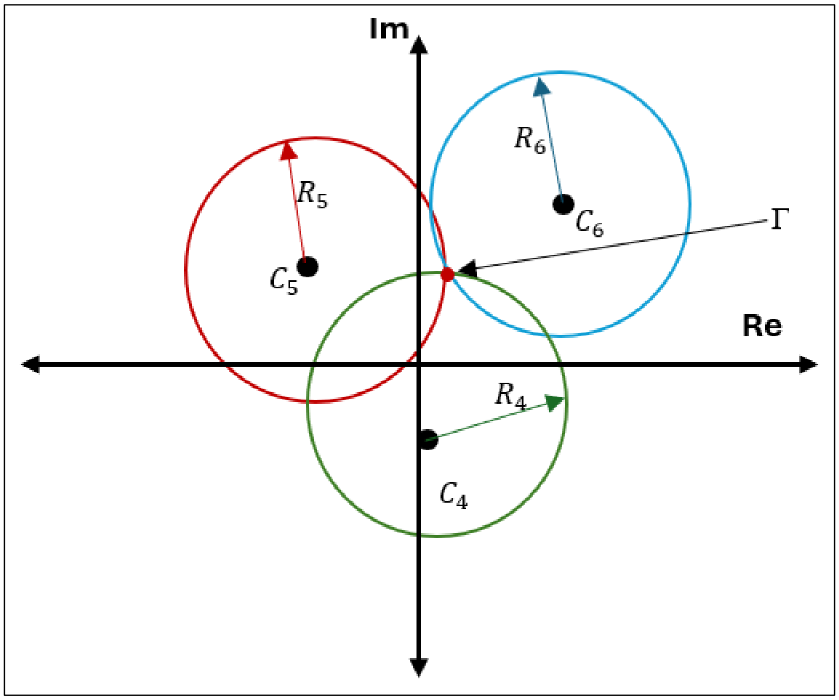

Figure 2: Graphical representation of ideal SPR

As was mentioned previously, the q_i depend only on the S-parameters of the designed six-port circuit. The transformation to the centers of the circles, C_i, is applied uniformly to each of the q_i. This means that if we want to keep the centers equally spaced on an equilateral triangle in the complex plane, we have the ability to do that by making sure the original q_i are so placed. The transformation given by (2.49) from the q_i to the C_i does not deform the triangle on which the q_i are placed. We explore some graphical scenarios in Appendix (A.2). It only enlarges or compresses, and rotates the triangle based on the measurements of the DUT (via k). This leads to the design criteria for the six-port circuit.

2.5 Design Criteria of a Six-port Reflectometer

A six-port reflectometer comprises of three main components: a signal source usually a RF signal generator, a six-port circuit, and power detectors attached at the four ports [4]. Since we typically normalize by the power $|b_3|$ in the six-port equations, port 3 is usually designed as a reference port. The power measured at this port (P_3) is not dependent on the DUT instead it represents the property of the six-port circuit and the power input of the RF source.

The critical design consideration lies in the selection of the q_i points as illustrated in Figure 3. This geometric interpretation provides a visual representation of the six-port equations, where each circle is determined by the power measurement at one of the detector ports. The overdetermined nature of this system (2.56), with three complex-valued equations for two unknowns (the real and imaginary parts of the reflection coefficient), contributes to the measurement accuracy.

The ideal positioning of the q_i points for measurements performed using an SPR should be spread equally across the entire complex plane [5]. This is achieved when the q_i points are located at the vertices of an equilateral triangle, which is centered at the origin of the Γ-plane. For this optimal configuration the magnitudes of the q_i points should be the same:

$$|q_4| = |q_5| = |q_6| \tag{2.57}$$

Furthermore, the relative phase separations between the q_i points should be equal to 120°. The importance of proper q_i positioning becomes evident when considering how the reflection coefficient Γ_{DUT} is determined. Γ_{DUT} is calculated from the intersection of three circles in the complex plane.

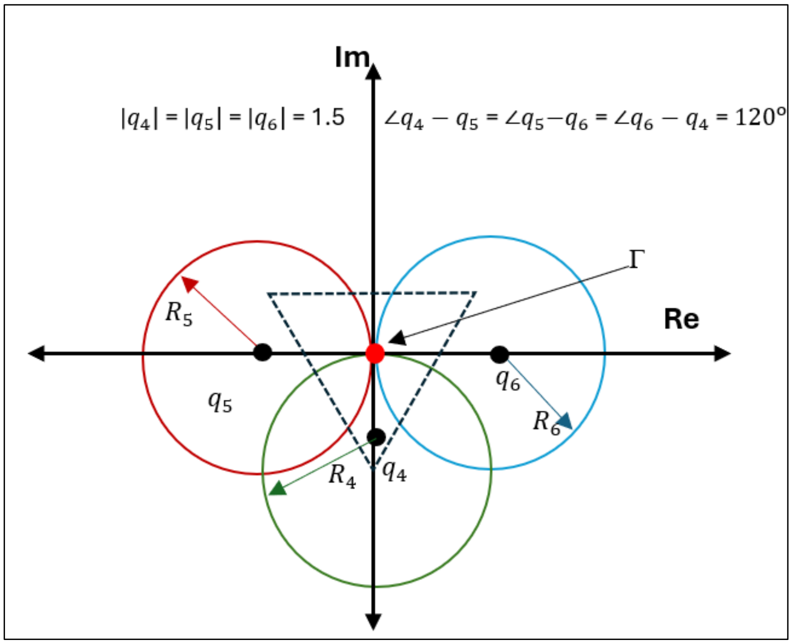

Figure 3: Graphical interpretation for determining reflection coefficient.

To achieve optimal performance, the recommended design for the six-port circuit that will be used as an SPR [4] is:

$$q_4 \approx 1.5\angle\theta_o^{\circ} \tag{2.58a}$$

$$q_5 \approx 1.5\angle(\theta_o + 120^{\circ}) \tag{2.58b}$$

$$q_6 \approx 1.5\angle(\theta_o - 120^{\circ}) \tag{2.58c}$$

Where θ_0 is an arbitrary phase reference value. This configuration ensures that the q_i points are equally separated, and maintain the desired 120° phase separation, thereby optimizing the reflectometer's measurement accuracy and reliability across a wide range of DUTs and operating conditions.

2.6 Six-Port Architecture Review

Various six-port architectures have been documented in the literature [14]. This section will explore different architectures of six-port reflectometers, highlighting their unique characteristics and the rationale behind their respective configurations. By examining these structures, we can gain insight into the evolution of six-port technology and the trade-offs involved in the unique design approaches. As discussed in Section 2.5, the ideal six-port reflectometer design, according to Engen, should have $|q_4| = |q_5| = |q_6|$, with q_i points separated by ±120° relative phase separation in the complex Γ-plane, forming an equilateral triangle centered at the origin of the reflection coefficient plane.

In 1972, Hoer [5] proposed a design that incorporated hybrid junctions and a power divider to construct a six-port reflectometer, capable of measuring complex impedance, phase angle, voltage, current, and power. Hoer later proposed an enhanced circuit for complex voltage ratio measurements [6], which was subsequently adapted for S-parameter measurements in a dual six-port system [7]. In 1977, the design proposed by Engen [8] proved to be a reference for other design modifications done till date. Engen's "preferred" six-port reflectometer design, as illustrated in Figure 4, utilizes port 4 as the normalizing (reference) power port. This configuration aims to optimize the application of six-port technique for microwave parameter measurements. The proposed design modifies the ideal separations of q_i points with a phase separation of ±135°, and $|q_5| = |q_6| = 2$, $|q_4| = \sqrt{2}$ (following Engen's analogy since he is using port 4 as reference port). Engen argued that this design compromise offered optimal performance for its time, with minimal deviation from the "ideal" configuration compared to potential performance degradation from non-ideal components [14].

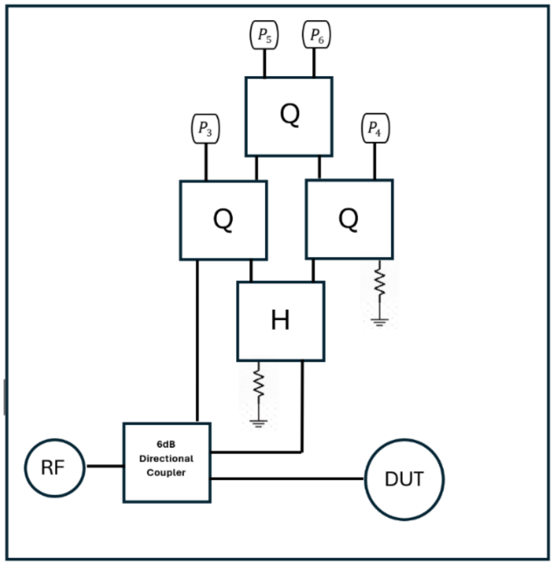

Figure 4: Schematic of Engen's Preferred Six-port Design [5]

The structure comprises three quadrature hybrid couplers and one 180° hybrid coupler with a terminated arm acting as a power divider, assumed to be lossless. In this configuration, one-quarter of the input power reaches the measurement port and is absorbed, while the remainder is equally distributed among ports three to six when the device under test (DUT) is a matched load. The drawback of this design was that slight changes in the hardware implementation (couplers, power dividers) added enough noise to affect the position of q_i points and eventually the complex reflection co-efficient Γ_2 [14]. Another drawback was that absolute power calibration of the diode detectors was required for accurate measurements [14].

Researchers have proved that standard power dividers and couplers are not capable to achieve an optimal six-port junction [14], [51]. To achieve optimal accuracy, couplers of very specific coupling factors suitable for each frequency are required along with very high dynamic range of power detectors, which is a non-feasible and high-cost solution. The term "frequency compensated quasi-optimal" refers to a design strategy that mitigates the frequency-dependent variations in the positions of $q_{i=4\ldots6}$ within the reflection coefficient plane. Instead of controlling these variations by using more optimized components which is not a convenient way as stated above, we optimize the electrical length of interconnecting lines within the six-port reflectometer. This quality makes these designs low-cost and robust. To achieve frequency compensation, the electrical lengths of the internal transmission lines must satisfy specific relationships. When these conditions are met, the values and locations of q_i remain stable across the frequency range of operation, thereby maintaining measurement accuracy.

Ghannouchi et al. [4] proposed a design for a quasi-optimal six-port reflectometer consisting of directional quadrature hybrid 3 dB and 10 dB couplers, a power divider and a 3 dB attenuator in the delay line as shown in Figure 5.

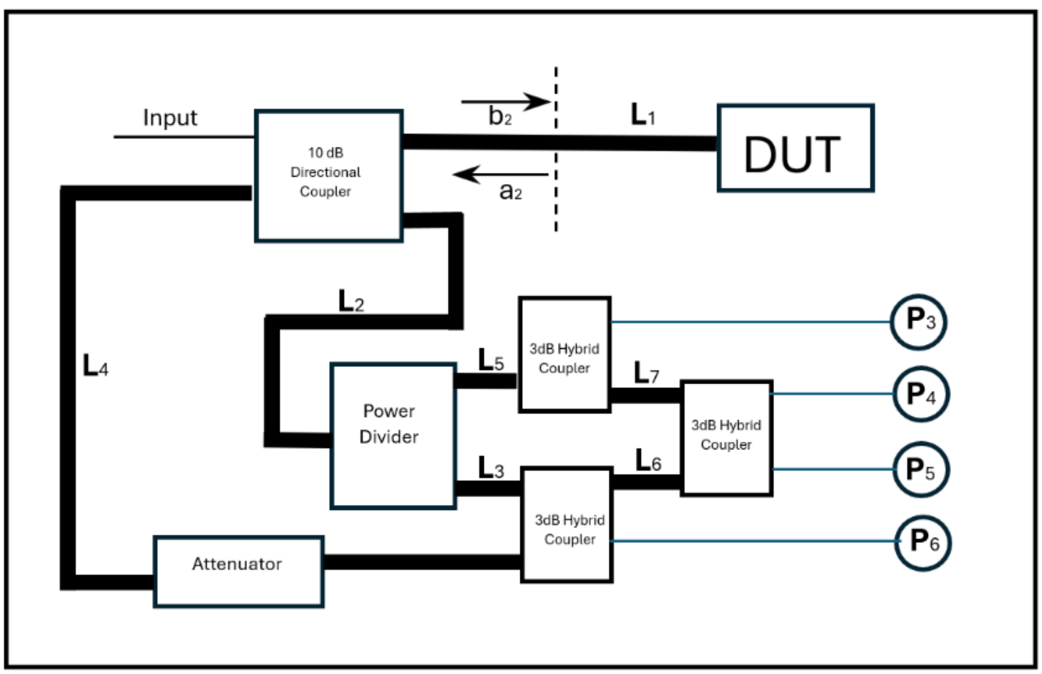

Figure 5: Quasi-Optimal Six-port Reflectometer [14]

While we don't go over the math here, and leave it to Ghannouchi et al. [4], the requisite electrical length relationships for frequency compensated quasi-optimal design can be expressed as follows:

$$2L_1 + L_4 + L_q = L_2 + L_3 + L_p \tag{2.59a}$$

$$L_7 + L_5 = L_6 + L_3 \tag{2.59b}$$

Where L_i represents the electrical length of the i-th transmission line segment, while L_p is the electrical length of the power divider and L_q is the electrical length of the quadrature hybrid couplers. By adhering to these equations, the six-port reflectometer design ensures that the critical q_i-points maintain their optimal positions in the reflection coefficient (Γ) plane, independent of frequency variations. This compensation technique enhances the broa dBand performance and measurement reliability of the six-port reflectometer [14]. Frequency compensated designs help minimize the requirement for high dynamic range of power detectors.

In 1991, Ghannouchi et al. improved his design (as shown in Figure5). He proposed a wideband mm Wave SPR. According to Ghannouchi et al., it is the ‘optimum design’ for a frequency compensated quasi-optimal six-port reflectometer [9]. The design includes four 3 dB hybrid couplers, an attenuator and a power divider. The SPR was designed for mm-Wave frequency applications, 18-40 GHz frequency bandwidth and tested for a 3 dB attenuator. Schottky diode detectors were used for power measurements. The operating frequency range of the SPR can be adjusted by using hybrid couplers and transmission lines for any particular bandwidth. The Schottky diodes for power measurement need to be linearized for the respective design and this linearization is sufficient for calculation of the complex reflection coefficient (Γ), hence absolute power calibration of diodes is not necessary in this design. The linearization of all detectors at each frequency point in the dynamic range (40 dB) was required. A detailed description of basic components of an SPR is presented in Appendix A.1.

Other designs for frequency-compensated quasi-optimal six-port junction have been developed using Miniature Hybrid Microwave Integrated Circuit (MHMIC) technology, implemented on a 10-mil alumina substrate in microstrip configuration. This design incorporates branch-line couplers, a Wilkinson power divider, and a 3 dB attenuator [4]. Additionally, a second frequency-compensated quasi-optimal six-port junction has been designed and fabricated using Monolithic Microwave Integrated Circuit (MMIC) technology on a 500 µm GaAs substrate, employing coplanar waveguide structures. This design features four branch-line couplers, a Wilkinson power divider, and a 3 dB attenuator. Notably, this junction integrates four power detectors within its structure, achieving a compact footprint of $3 \times 3.5\ mm^2$ [4].

2.7 Selected Six-port Reflectometer Design

Our study uses a modified version of the frequency compensated quasi-optimal design proposed by Ghannouchi et al. in 1991 [9] details of which have been discussed in the section above. This design was proposed by Aboud [2] in his work done in 2022. The modification lies in the selection of components and co-planar waveguides used for fabrication of the SPR in our desired frequency range (0.6-1.4 GHz). Figure 6 shows the design topology of our selected SPR.

Since our aim is to design a low-cost, portable and robust SPR therefore a quasi optimal six-port reflectometer is suitable for our application. We used 3 dB quadrature hybrid couplers with a frequency range of 1 to 2 GHz with 0.45 dB insertion loss and 20 dB isolation. Power dividers used had a bandwidth of 0.9-2.1 GHz. These were the readily available surface mount, high isolation components which met our design requirements. Our reflectometer has a bandwidth of 0.6-1.4 GHz, and this limitation is only due to the frequency limit of the readily available components used (power detectors, hybrid couplers). More precise components might be utilized in the future for larger bandwidths, but this setup is sufficient for proof of concept. The connections were made using co-planar waveguide transmission lines of 50-ohm impedance and electrical lengths adjusted according to the design requirements. FR-4 substrate with relative permittivity of 4.3 was used.

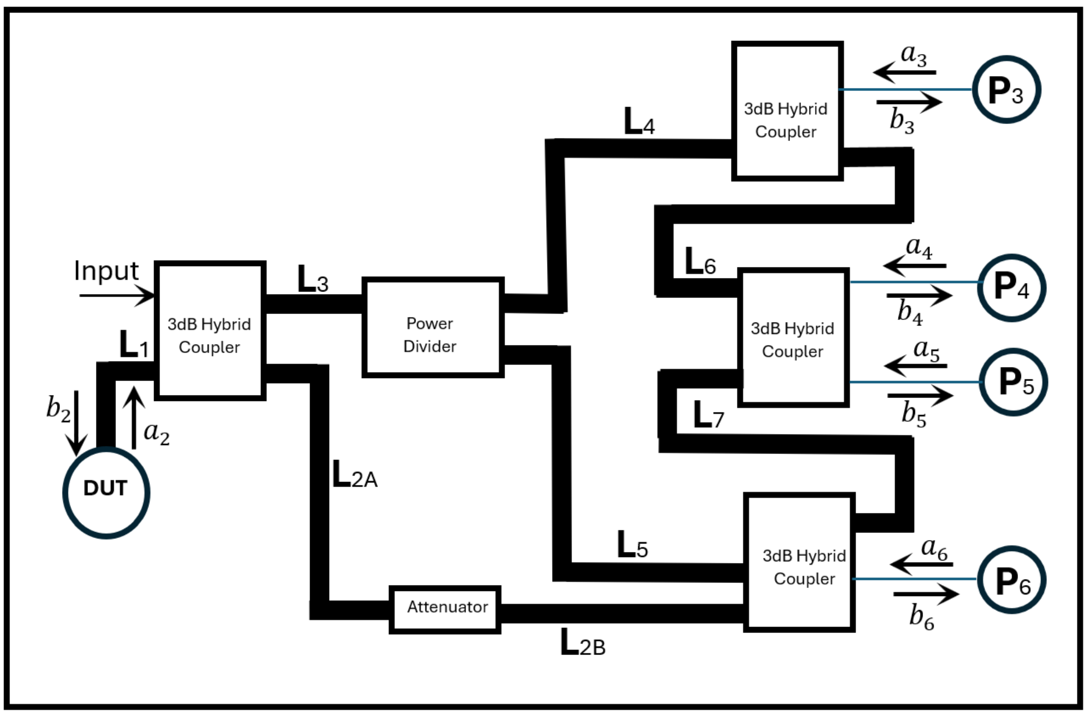

Figure 6: Chosen Six-port Reflectometer Design [2]

To make the position of q_i-points, independent of the frequency in the Gamma plane, the following equations for the electrical lengths of the transmission lines must meet[9]:

$$L_q + L_4 + 2L_1 = (L_{2A} + L_{2B}) + L_3 + L_p \tag{2.60a}$$

and
$$L_5 + L_7 = L_3 + L_6 \tag{2.60b}$$

L_q is the electrical length of the 3 dB Hybrid coupler while L_p is the electrical length of the power divider and $L_{1..7}$ are the electrical lengths of the transmission lines. Using the same algebraic derivation as in [4] we get the following nominal values of q_i-points, these are same as the Engen's proposed 'optimal' values [5].

$$q_4 \approx 2\angle 0° \tag{2.61a}$$
$$q_5 \approx 2\angle 270° \tag{2.61b}$$
$$q_6 \approx \sqrt{2}\angle 135° \tag{2.61c}$$

Details about the design have been discussed in Chapter 5. Figure 7 shows the q_i points of the SPR used in this thesis.

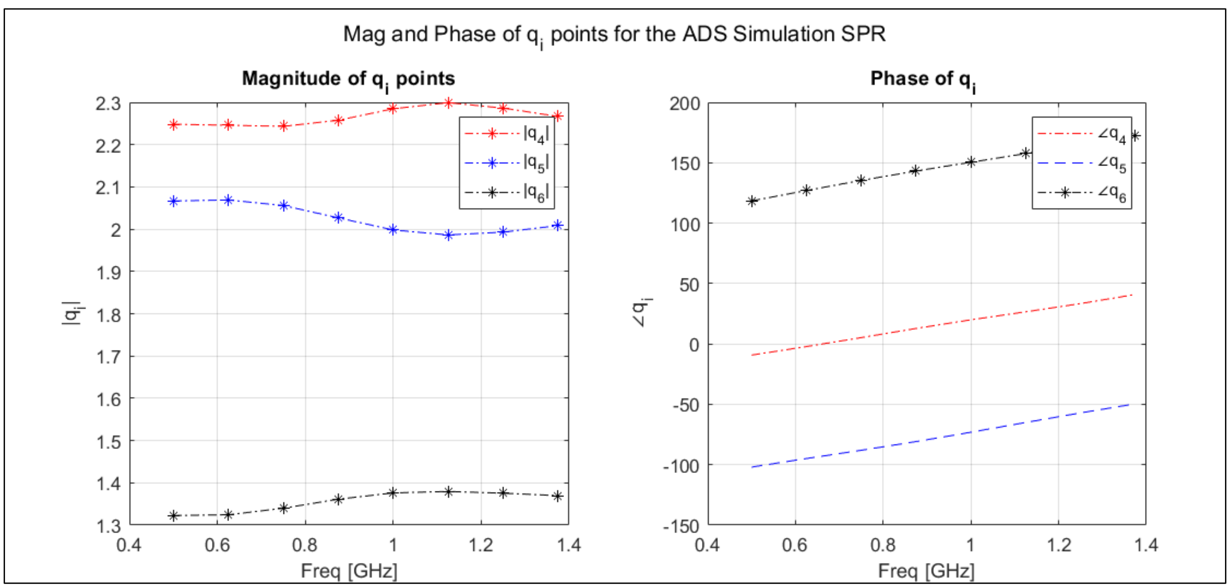

Figure 7: Magnitude and Phase of q_i points of the selected SPR

2.8 A Brief History of Six-port Reflectometers

The foundational work on six-port junctions was initiated in the 1970s by Engen and Hoer at the National Bureau of Standards [6], [10] paving the way for numerous six-port configurations in subsequent literature [5], [7], [8], [11], [12], [13], [14], [15], [16]. The six-port technique can be generally described as a method of analyzing reflection coefficient parameters.

Recent advancements in six-port technology have yielded several innovative designs across various frequency ranges. Qayyum and Negra [13] developed a compact six-port junction employing broadside-coupled waveguide technology for the 1.5-2.5 GHz range. Their design exhibited an amplitude and phase error of 2.8 dB and ±10°, respectively, making it suitable for six-port receiver applications. In 2017, Zhang et al. [14] introduced a novel dual-band six-port receiver operating in the 2-3 GHz range, utilizing a real time-delay neural network. In 2018, Sun et al. [17] proposed a wideband six-port correlator with integrated filtering functionality, covering 1.6-2.6 GHz. Their measurements revealed robust wideband performance, with transmission coefficients of -8.1 ± 1.6 dB and return loss below -10 dB across the entire operating band. In 1989, Ghannouchi et al. et al. [18] used power transistors to measure the power received and impedance of the load. In 1990, Bilik et al. [19] proposed a wideband MMIC design using lumped elements in the SPR, but it had high losses. In 1997, Wiedemann[20] improved the MMIC design with lower losses and attenuation of 6-10 dB. A compact microstrip based six-port design was proposed in 2011 by Fang et al. [21] using Wilkinson Power Dividers and quadrature hybrid couplers, the system had a return loss of -10 dB.

Research in the 1980s concentrated on expanding the frequency range of six-port systems [9], [18], [19], [22], [23], [24], [25], [26], [27], [28], [29], [30], [31], [32], [33], [34], [35], [36], [37],

[38], [39] , once the technique was well-established the 1990s witnessed growing interest in developing new applications and improved hardware for six-port technology [9], [12], [15], [16], [19], [20], [22], [23], [24], [25], [40], [41], [42], [43], [44]. A comparison of different six-port hardware designs and their applications is presented in Appendix A.3.

2.9 Applications for Six-Port Based Circuits

After 40 years of development researchers have not been able to compete the six-port techniques with the conventional automatic network analyzers. Efforts have been made to design and develop the SPRs for specific applications and consider them as compact, portable and low-cost solutions with low hardware complexity.

The six-port technique has been applied to measure dielectric characterization of materials [45], collision avoidance radar sensors [15] , and direction-finding antenna systems [16]. In 2017, Jurlat and Tarabelsi [46] applied the six-port reflection coefficient technique to determine moisture content in a biomass chamber. In the same year, Staszek [47] also proved the application of a SPR to measure scattering parameters for gas detection and breath analyzing applications.

Six-Port reflectometers have been used for Microwave Imaging as well. This imaging technique has seen progress in recent years due to its non-invasive nature and low-cost. The basic principle for this imaging is the contrast between the dielectric permittivity between two materials, this can be either due to difference in moisture content of grains, tumors in human body causing blood clots to increase permittivity or any other application where the scattered waves help realize the difference in complex permittivity of the device under test. In 2013, Kissinger et al. [48] used a six-port reflectometer to measure the reflection coefficient of the material under test for microwave applications. In 2016, Lee [45] proposed the use of six-port reflectometers with dielectric probes and evaluated the system by comparing malignant tumor and healthy breast tissues, the results showed differences in magnitude measurements of the powers of the four ports.

Six-port receivers have been used in telecommunications as well. In 2017, Zhang et al. [14] proposed a time-delay neural network based six-port receivers, it worked between 2-3GHz and had a low error vector modulation value. In the same year Qayyum [13] proposed a SPR based broad side coupled wave guide with a wide bandwidth of 1.5 to 2.5 GHz.

Ibrahim et al. (2016) [49] presented a six-port interferometer designed for direction of arrival detection in the 5-8 GHz frequency range. The simulated performance of the six-port network demonstrated favorable characteristics within the operational bandwidth of 5.5-7.8 GHz. Additionally, the phase shifts between the relevant ports-maintained values close to ±90° across the broader 5-8 GHz bandwidth. These results suggest that the proposed six-port interferometer exhibits suitable performance metrics for direction of arrival applications within the specified frequency range.

Some prominent six-port reflectometer characterization techniques and the proposed hardware, along with applications of the designs are provided in Table 1. in Appendix.

3 Six-Port Reflectometer based Vector Network Analyzer:

In this Chapter we discuss how researchers have used SPRs to create Vector Network Analyzers (VNAs). VNAs are sophisticated devices used to measure the network parameters in electrical circuits for RF and microwave applications. They are used to measure the magnitude and phase of the full S-parameters of an arbitrary device under test. Note that S-parameters can be converted to any other network parameters of interest (Impedance, Admittance, Return Loss, Group Delay) [1]. The six-port reflectometer-based vector network analyzer (SPR-VNA) that will now be described, performs similar to a conventional VNA but instead of using the complex active circuits it just uses a combination of SPRs.

In 1977 Hoer [7] proposed the design of the first microwave network analyzer which was able to measure the transmission coefficients of the DUT by using two identical SPRs and connecting them with a single local oscillator acting as a signal generator. Attenuators and phase shifters were used to shift the phase of the input signals among the two SPRs being used, as shown in Figure 8. He proved that we could measure transmission coefficients using scalar powers. In 1984, Hoer [26] proposed the use of diode detectors for measuring powers at the ports. This setup was then improved over time for different applications and accuracy of the measurements [14].

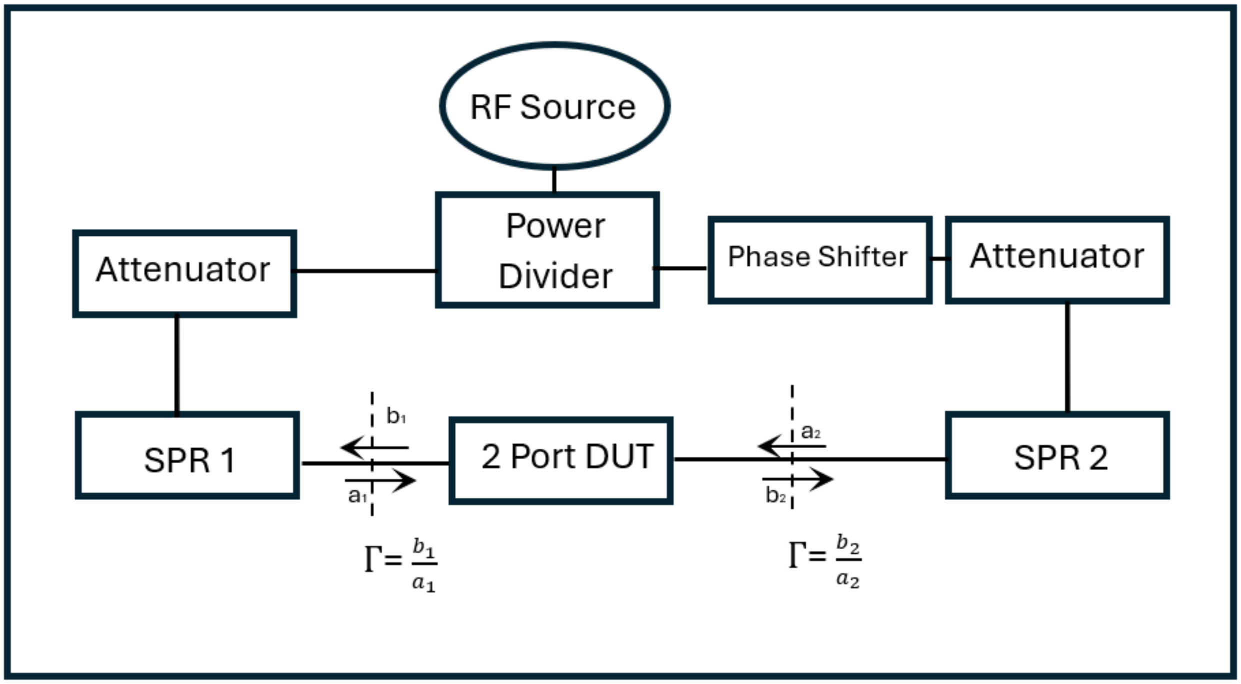

Figure 8: Hoer's [4] topology of a Six-port Network Analyzer

3.1 SPR-VNA Theory:

The theory behind the dual six-port network analyzer was introduced by Hoer [7]. His proposed design is shown in Figure 8 above. The system employs two SPRs to measure the complex ratios $\Gamma_1 = b_1/a_1$ and $\Gamma_2 = b_2/a_2$, b_1 and b_2 are the waves emanating from the DUT while a_1 and a_2 are the waves impinging on the DUT respectively. These ratios are related to the (two-port) S-parameters of the DUT through the following equations:

$$b_1 = S_{11}a_1 + S_{12}a_2 \tag{3.1a}$$
$$b_2 = S_{21}a_1 + S_{22}a_2 \tag{3.1b}$$

Dividing (3.1) by a_1 and (3.2) by a_2 and using $\Gamma_1 = \frac{b_1}{a_1}$ and $\Gamma_2 = \frac{b_2}{a_2}$, gives

$$\Gamma_1 = S_{11} + S_{12}\frac{a_2}{a_1} \tag{3.3}$$

$$\Gamma_2 = S_{22} + S_{21}\frac{a_1}{a_2} \tag{3.4}$$

Adding (3.3) and (3.4) we get

$$\Gamma_1 + \Gamma_2 = S_{11} + S_{22} + S_{12}\frac{a_2}{a_1} + S_{21}\frac{a_1}{a_2} \tag{3.5}$$

Multiply (3.3) with Γ_2 on both sides

$$\Gamma_1\Gamma_2 = \left(S_{11} + S_{12}\frac{a_2}{a_1}\right)\Gamma_2 \tag{3.6}$$

From (3.4) we can replace Γ_2 in (3.6)

$$\Gamma_1\Gamma_2 = \left(S_{11} + S_{12}\frac{a_2}{a_1}\right)\left(S_{22} + S_{21}\frac{a_1}{a_2}\right) \tag{3.7a}$$

$$\Gamma_1\Gamma_2 = S_{11}S_{22} + S_{11}S_{21}\frac{a_1}{a_2} + S_{22}S_{12}\frac{a_2}{a_{11}} + S_{12}S_{21}\left(\frac{a_2}{a_1}\right)\left(\frac{a_1}{a_2}\right) \tag{3.7b}$$

$$\Gamma_1\Gamma_2 = S_{11}\left(S_{22} + S_{21}\frac{a_1}{a_2}\right) + S_{22}S_{12}\left(\frac{a_2}{a_1}\right) + S_{12}S_{21} \tag{3.7c}$$

$$\Gamma_1\Gamma_2 = S_{11}\Gamma_2 + S_{22}S_{12}\frac{a_2}{a_1} + S_{12}S_{21} \tag{3.8}$$

If we multiply (3.3) by S_{22} on both sides, we get:

$$\Gamma_1 S_{22} = S_{11}S_{22} + S_{22}S_{12}\frac{a_2}{a_1} \tag{3.9}$$

Subtracting (3.9) from (3.8)

$$\Gamma_1\Gamma_2 - \Gamma_1 S_{22} = S_{11}\Gamma_2 + S_{22}S_{12}\frac{a_2}{a_1} + S_{12}S_{21} - S_{11}S_{22} - S_{22}S_{12}\frac{a_2}{a_1} \tag{3.10}$$

$$\Gamma_1\Gamma_2 - \Gamma_1 S_{22} = S_{11}\Gamma_2 + S_{12}S_{21} - S_{11}S_{22} \tag{3.11}$$

Denoting the determinant of a scattering matrix as Δ:

$$\Delta = \begin{vmatrix} S_{11} & S_{12} \\ S_{21} & S_{22} \end{vmatrix} = S_{11}S_{22} - S_{21}S_{12} \tag{3.12}$$

And incorporating (3.12) in (3.11) we can write

$$\Gamma_1\Gamma_2 = \Gamma_1 S_{22} + \Gamma_2 S_{11} \text{- } \Delta \tag{3.13}$$

This represents an equation in three complex-valued unknows S_{11}, S_{22}, and Δ, where the constants in the equation are Γ_1 and Γ_2 that depend on the DUT. These values of these constants can be obtained using the SPR. Notice that Γ_1 and Γ_2 depend not only on the DUT but also on the values of the incoming voltage waves a_1 and a_2. Therefore, Hoer's procedure says that we can measure Γ_1 and Γ_2 using a minimum of three different phase shifts (three for simplicity) between the input voltage waves being fed into the SPRs. Writing (3.13) in matrix form for each phase shift we get:

$$\begin{bmatrix} \Gamma_2^{\theta_1} & \Gamma_1^{\theta_1} & -1 \\ \Gamma_2^{\theta_2} & \Gamma_1^{\theta_2} & -1 \\ \Gamma_2^{\theta_3} & \Gamma_1^{\theta_3} & -1 \end{bmatrix} \begin{bmatrix} S_{11} \\ S_{22} \\ \Delta \end{bmatrix} = \begin{bmatrix} \Gamma_1^{\theta_1}\Gamma_2^{\theta_1} \\ \Gamma_1^{\theta_2}\Gamma_2^{\theta_2} \\ \Gamma_1^{\theta_3}\Gamma_2^{\theta_3} \end{bmatrix} \tag{3.14}$$

The number of phase shifts can be varied to obtain a better condition number of the over-determined matrix which can then be solved using the least-squares technique. Once S_{11}, S_{22}, and Δ are obtained we still need to determine S_{12}, S_{21}. For a reciprocal network, $S_{12} = S_{21}$ so using (3.12) we can write

$$|S_{12}|^2 = |S_{21}|^2 = |S_{11}S_{22} - \Delta|^2 \tag{3.15}$$

$$S_{12} = S_{21} = \sqrt{S_{11}S_{22} - \Delta} \tag{3.15a}$$

From (3.15a) we can find the magnitude and phase of the DUT.

For non-reciprocal networks, Hoer suggests that we first determine the magnitude $|S_{12}|$ from (3.3) and $|S_{21}|$ from (3.4):

$$|S_{12}| = \left|\frac{\Gamma_1 - S_{11}}{a_2/a_1}\right| \tag{3.16a}$$

$$|S_{21}| = \left|\frac{\Gamma_2 - S_{22}}{a_1/a_2}\right| \tag{3.16b}$$

The phases of S_{12} and S_{21} can then be found using:

$$\phi_{12} = \psi_1 - \psi_0 \tag{3.17a}$$
$$\phi_{21} = \psi_2 + \psi_0 \tag{3.17b}$$

Where $\psi_1 = \arg\,(\Gamma_2 - S_{11}), \psi_2 = \arg\,(\Gamma_2 - S_{22})$, and $\psi_0 = \arg\,(a_2/a_1)$.

For reciprocal networks, this simplifies to:

$$\phi_{12} = \phi_{21} = \frac{\psi_1 - \psi_2}{2} + n\pi \tag{3.18}$$

Where n is an integer determined by an estimate of φ_{12} or ψ_0.

Although Hoer [7], proposes the above phase retrieval method, for both reciprocal and non-reciprocal DUTs, in our case for reciprocal DUTs, we were able to get accurate phase of our $S_{12} = S_{21}$ without these additional corrections(3.17-3.18). We believe this is likely due to improved calibration procedures and accurate linearization of our diode power detectors which are described in later sections.

3.2 Review of SPR-VNA Designs:

Barakat[51] proposed a 2-port VNA based on two six-port correlators terminated with diode power detectors. His design consisted of modified ring power divider and quadrature hybrid couplers. He used a 3 dB attenuator as the device under test. Figure 9. shows the design of SPR-VNA proposed by Barakat[51].

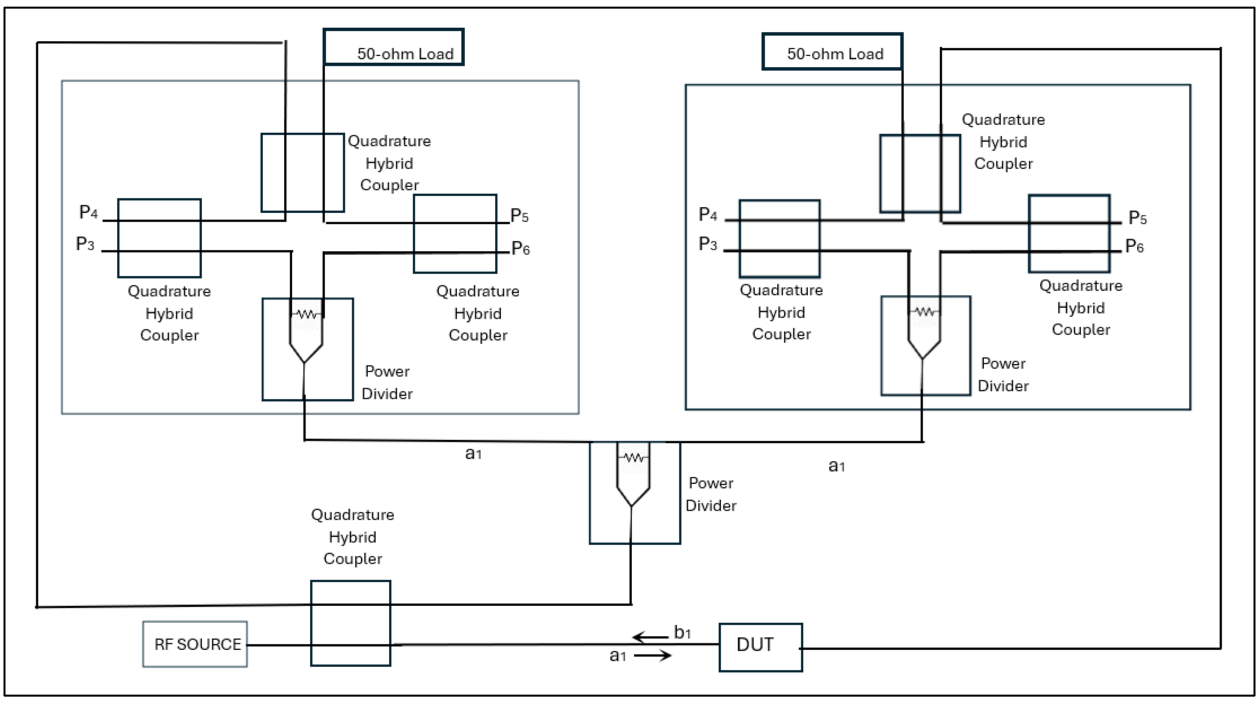

Figure 9: Barakat's proposed Six-port Network Analyzer[51]

In 2019, Sahoo.et al [52] proposed a SPR-VNA based on 2 different topologies of SPRs. He combined two different designs of the six-port reflectometers, one consisting of three hybrid couplers (3 dB) and the other consisting of four hybrid couplers. He designed his VNA for 1.8-2.1GHz frequency bandwidth. Since then, many researchers have used six-port network analyzers, but they all contain a single RF source with attenuators and phase shifters to operate.

In 2022, Yakabe et al. [50] proposed a six-port correlator based VNA, designed for 28GHz center frequency and 40 dB dynamic range. The bandwidth of the device was 4GHz, the author owes this to the frequency dependence of the components. The dynamic range of the system was improved from 30 dB to 40 dB by using better power measurement methods. He used a single six-port reflectometer with an isolator and power divider to measure transmission coefficients in his reciprocal DUT. A manual coaxial switch and other benchtop equipment was used in his setup.

The six-port network analyzer is usually a combination of two reflectometers in different configurations although a single reflectometer-based network analyzers have been proposed in recent literature [50].

3.3 Our Design of a Distributed SPR-VNA:

Notice that all the previous designs of the SPR-based VNA have used (required) a single RF source. Clearly, the mathematical foundations discussed in Section 3.1 do not impose that a single RF source be utilized. Only that we have the ability to vary the phase of the RF voltage waves a_1 and a_2 arriving at each port of the DUT. Therefore, the question of whether two independent sources could be used is an important because this would allow one to create a 'Distributed SPR-VNA' architecture where each SPR would have its own RF input source. The concept of such a design was first proposed and simulated by Aboud [2]. As discussed in the Introduction, he did not complete the analysis on the viability of such a design.

We now describe our distributed six-port based vector network analyzer design that uses two independent RF sources. This design basically follows Hoer's original design but decouples the RF inputs . A block diagram of our distributed six-port network analyzer is shown in Figure 10.

It consists of two separate Six-Port Reflectometers with nothing attached in between them, replacing the need of attenuators or power dividers. It consists of two separate Six-Port Reflectometers with nothing attached in between them, replacing the need of attenuators or power dividers. The phase shift is needed in one of the RF sources, it can be done through a separate RF device or using an internal phase shifter of the source.

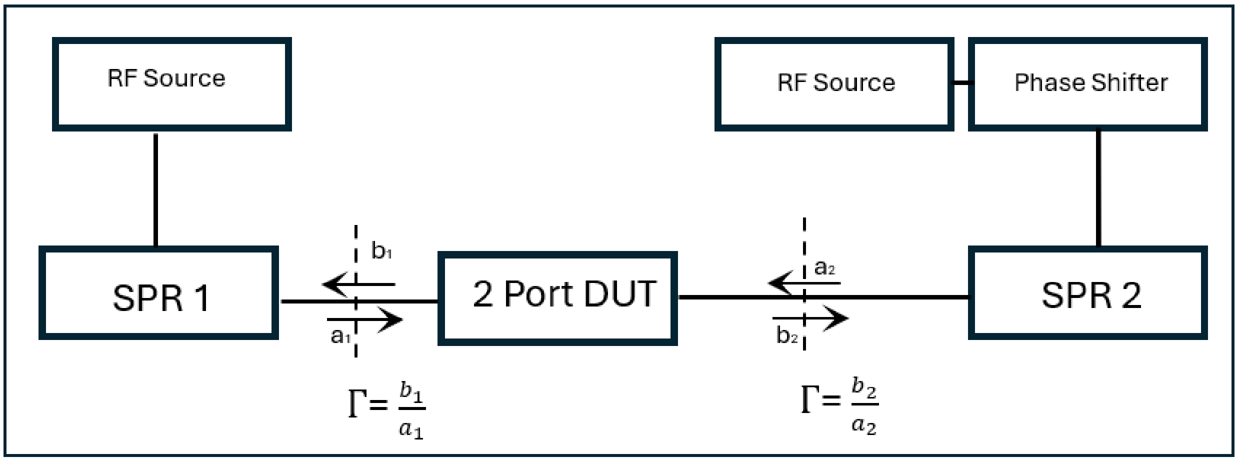

Figure 10: Block Diagram of the Distributed SPR-VNA [51]

This architecture forms the bases of all the experiments reported in the remaining parts of this thesis. Given that the use of independent RF sources in SPR-VNA is new and has not been proven in an experimental setting, the remaining part of this thesis reports on our evaluation of the viability of different techniques to find the S-parameters. Results and hardware of our Distributed SPR-VNA have been discussed in later Chapters 5 and Chapter 6.

4 SPR Measurement Techniques

We have already described the SPR mathematical foundations as well as the architecture of the SPR we will be investigating. Performing SPR reflection coefficient measurements is not simply a matter of measuring the scalar powers at four ports of the six-port circuit with one port attached to an RF source and the DUT attached to the remaining port. Looking back at the mathematical foundations we see that the straightforward method in going from power measurements to Γ is based on having the six-port parameters of the six-port circuit making up the SPR. This means that we would require an accurate characterization of the six-port parameters, which we call having an accurate characterization of S^6. Of course, some of the mathematical development utilizes the inverse of S^6, or $\bar{S}^6$ but that is not important. Given S^6 one develops the parameters of the three circles and then solves for the intersection point in the Γ-plane. This can be done in several ways, we investigate two: a geometrical approach and a full nonlinear equation solver approach. This whole track, we call a characterization-based approach because one first must accurately characterize the S^6 of the six-port circuit being used in the SPR.

Alternatively, when one reviews the literature (e.g., [14]) one sees various so-called ‘calibration’ techniques being referred to. These are specialized methods that have been developed by researchers to obtain the Γ of the DUT without actually knowing the S^6 of the six-port circuit. These calibration techniques are so-called because one requires known calibration standards, obtains the scalar power measurements for each of the calibration standards, and then, via several mathematical procedures obtains the intermediate variables or parameters that can then be used to obtain the Γ of the DUT from the power measurements.

We explore both types of methods. Those requiring the S^6 of the six-port circuit we will continue to call characterization-based techniques, whereas those using calibration standards and not requiring knowledge of the S^6, we will consistently refer to as calibration-based techniques.

The conventional Short-Open-Load (SOL) type of technique that is used in standard VNA measurements can be added to any of these procedures as will also be described. As the name implies, these require three calibration loads: a short, an open and a load. We will consistently refer to it as ‘SOL Error Correction’.

Although many calibration and characterization methods have been proposed and improved over the years, no procedure has been proved which relies solely on ‘SOL Error Correction’ as in the conventional benchtop network analyzers.

The initial work by Engen and Hoer [5], [6], [7], [8], [54] established that the six-port reflectometer operation can be quantified through a system of non-linear equations relating power detector ratios to the unknown reflection coefficient. Appropriate characterization and calibration procedures can also eliminate measurement errors caused by hardware imperfections [4]. Various calibration procedures have been proposed to date to determine the calibration coefficients [12], [22], [32], [39], [52], [55], with Engen's six-port to four-port reduction technique [10], widely regarded as one of the most robust methods [4]. In this technique we separate our SPR measurements into two steps, the calibration step using 9 unknown sliding loads followed by an SOL calibration using 3 known (short, open, load) loads. Details of this are discussed in Section 4.4. The advantage of using sliding loads or multiple on-board calibration loads offers the ability to re-calibrate the system in case of any external change if an automated system can be designed using on-board calibration terminations using a switch.

Since the development and availability of accurate multi-port network analyzers, researchers have proposed techniques which do not require multiple loads, but instead a S^6 of the six-port circuit used in the reflectometer in combination with the SOL calibration. This can be used for complete calibration and characterization of the system. This helped remove the inconvenience of using several loads, but the drawback of this technique lies in real-time applications where external environmental factors require the system to be calibrated repeatedly. Such factors include the changing temperature or humidity conditions in outdoor environments. The technique still is beneficial for application of SPRs in a controlled environment such as indoors.

Aboud [2] proposed such a 6-port S-parameter characterization technique for the reflectometer in combination with the SOL and showed that it can be used for complete calibration of the system. The use of a multi-port VNA for characterization of S^6 eliminates the need for utilizing multiple calibration test loads such as Engen's [1] 9-load and Haddadi's [54] 8-load methods (discussed in future sections).

In this thesis we report on our investigation of two calibration techniques that require loads (8 or 9) and three characterization-based techniques which require S^6. All of these can be used for achieving accurate reflection coefficient measurements of any DUTs. The multiple load methods differ in their requirements for the number of calibration standards and the computational complexity of the algorithms used to determine the calibration factors. In contrast, the methods employing S^6 of the SPR circuit, measured using a conventional multi-port VNA, combined with the DUT's power measurements require no external loads. This offers a novel methodology that demonstrates superior accuracy for our hardware as compared to conventional calibration techniques.

From Section 2.5 we have observed that, the centers of the three circles (2.49) which characterize the six-port junction, are functions of the power readings in the Γ-plane. These power readings are directly related to the DUT load connected to the measuring port (port 2). In other words, they depend not only on the six-port circuit but also the DUT being measured.

In this chapter, we will first explore the characterization-based techniques which require direct measurement of the S^6 that characterizes the six-port circuit used as the SPR to calculate the Γ_{DUT}. This includes Aboud's [2] approach, but we also present our two approaches using a geometrical and a non-linear optimization algorithm (Gauss-Newton Optimization). Since these approaches are dependent on the direct knowledge of S^6 which may change with environmental factors, and it would be inconvenient to get new S-parameters for each change in real scenarios, we also explore calibration techniques using 9-loads and 8-loads. The flow-chart shown in Figure 11 will help clarify all these approaches.

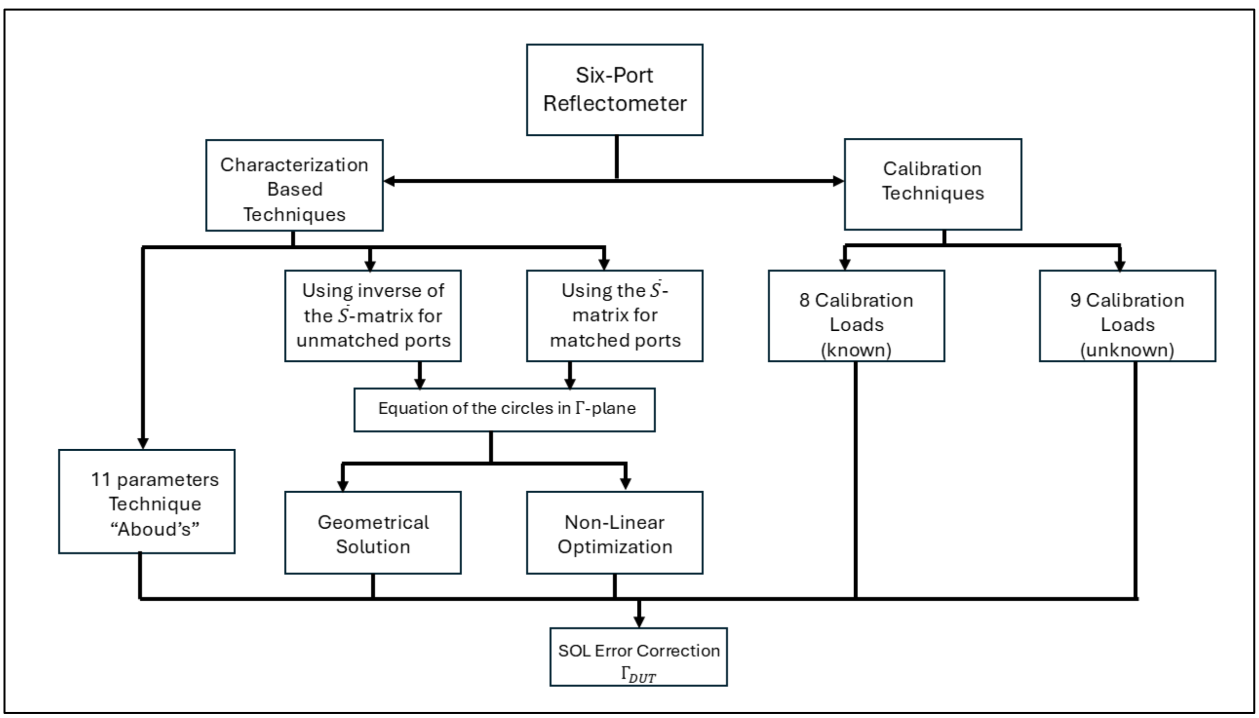

Figure 11: Flow Chart of SPR Measurement techniques

4.1 Characterization-Based Technique 1:

We refer to Characterization-based Technique 1 as using the Geometrical solution to find the intersection of the circles in the gamma-plane using either matched or unmatched loads. Once we get the equations of the circles (2.47) from the S-parameters of the six-port (S^6), we can use a geometrical approach towards calculating the point of intersection which represents the Γ_{DUT}. In chapter 2 we have derived the process to find the equations of the three circles from a S-parameter matrix. The result is equation (2.47):

$$|\Gamma_2|^2 - \Gamma_2\left(\frac{q_3^* k_i - q_i^*}{k_i - 1}\right) - \Gamma_2^*\left(\frac{q_3 k_i - q_i}{k_i - 1}\right) + \frac{k_i|q_3|^2 - |q_i|^2}{k_i - 1} = 0 \quad \text{where } i = 4..6$$

We also derived the centers and radii of these circles given by (2.49) and (2.56). The distance between any two points (x_1, y_1) and (x_2, y_2) is given by the Euclidean distance formula, thus the distance between any two centers is denoted by:

$$d = \sqrt{(x_2 - x_1)^2 + (y_2 - y_1)^2} \tag{4.1}$$

When the circles intersect, the coordinates of the intersection points (x, y) can be calculated using the following formulas [56]:

$$x = \frac{x_1 + x_2}{2} + \frac{r_1^2 - r_2^2}{2d^2}(x_2 - x_1) \pm \frac{y_2 - y_1}{2d}\sqrt{2(r_1^2 + r_2^2)/d^2 - (r_1^2 - r_2^2)^2/d^4 - 1} \tag{4.2}$$

$$y = \frac{y_1 + y_2}{2} + \frac{r_1^2 - r_2^2}{2d^2}(y_2 - y_1) \mp \frac{x_2 - x_1}{2d}\sqrt{2(r_1^2 + r_2^2)/d^2 - (r_1^2 - r_2^2)^2/d^4 - 1} \tag{4.3}$$

Where r_1 and r_2 are the radii of the circles. Equations (4.2) and (4.3) give the two intersection points for each pair of circles. Therefore, we may have a total of six intersection points given that we have three circles. We then choose the closest three of these intersection points and this defines the smallest triangle within which we must place the Γ_{DUT}. That is, the smaller the triangle the smaller the uncertainty in our prediction of Gamma_DUT.

There are certain conditions to check when we find the intersection of the circles; if they do not intersect, or all circles are within each other or two circles intersect instead of all three, this means our six-port circuit based SPR has failed for that particular frequency for the DUT. We have discussed in detail that the centers of the initial circles, q_i given by equation (2.24)(2.45), depend on the design of the six-port circuit used in the hardware SPR, and that it is very important to have those centers with similar magnitude and equal phase separation among them. On the other hand, the circles whose intersection we are actually solving for are defined by the C_i's and radii given by equations (2.49)(2.55), and those are dependent of the DUT.

The measured powers for any DUT are also affected by the accuracy of the power detectors. Thus, linearization and characterization of power detectors is important for an accurate measurement of powers. A schematic representation of this technique is shown in Figure 12. There are a total of twenty triangles that can be formed from the six intersection points (C_3^6). The triangle shown is the triangle with the smallest area. The Γ_{DUT} is chosen to be at the center of this triangle.

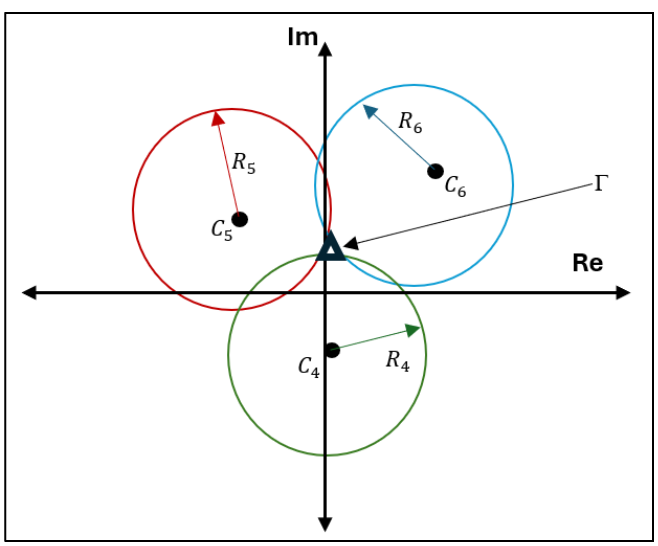

Figure 12: Graphical representation of 3 circles forming a triangle

4.2 Characterization-Based Technique 2

We refer to Characterization-Based Technique 2 that of following the block labelled Aboud in the flowchart of Figure 11. Aboud [2] proposed a characterization-based technique utilizing the S-parameters of a six-port circuit, measured via a multi-port benchtop VNA and the powers of the DUT. This method was inspired by a calibration approach proposed by Hoer [54] , which used three or more sliding shorts as calibration loads to compute the eleven calibration parameters. Subsequent researchers [32] , [55] adopted this technique. Notably, Aboud [2] innovatively eliminated the requirement for the sliding loads by deriving the calibration parameters directly from the S-parameters of the six-port circuit. The advantage of Aboud's technique is that we only need S^6 and powers at the four ports for the SPR for the DUT to measure Γ_{DUT}. Measuring the powers of different calibration loads is not required.

The method proceeds by obtaining eleven parameters. We first define the co-efficient γ_{i} as the real part of the q_{i} while δ_{i} as the imaginary part. From (2.52) we get

$$q_i = \frac{-A_i}{B_i} = \frac{S_{i1}}{S_{22}S_{i1} - S_{i2}S_{21}} = \gamma_i + j\delta_i \tag{4.5}$$

Thus, we see that we can obtaining the q_{i} directly from the S-parameters of the six-port circuit and then, from (2.56) we know that

$$p_i = \frac{P_i}{P_3} = \frac{|B_i|^2|\Gamma_{DUT} - q_i|^2}{|B_3|^2|\Gamma_{DUT} - q_3|^2} = M_i \frac{|\Gamma_{DUT} - q_i|^2}{|\Gamma_{DUT} - q_3|^2}$$

$$M_i = \frac{|B_i|^2}{|B_3|^2} = \frac{|S_{21}S_{i2} - S_{22}S_{i1}|^2}{|S_{21}S_{32} - S_{22}S_{31}|^2}$$

where $i = 4 \ldots 6$. The 11 parameters to characterize any arbitrary SPR are denoted, $F_{i=3\ldots6}$, $E_{i=3\ldots6}$ and $H_{i=4\ldots6}$. We don't go into the mathematical derivation of these parameters; it can be found in [51]. They final equations are:

$$k = \gamma_4(\delta_5 - \delta_6) + \gamma_5(\delta_6 - \delta_4) + \gamma_6(\delta_4 - \delta_5) \tag{4.6}$$

$$F_3 = \frac{-1}{2k}[|q_4|^2(\delta_5 - \delta_6) + |q_5|^2(\delta_6 - \delta_4) + |q_6|^2(\delta_4 - \delta_5)] \tag{4.7a}$$
$$F_4 = \frac{1}{2kM_4}[|q_3|^2(\delta_5 - \delta_6) + |q_5|^2(\delta_6 - \delta_3) + |q_6|^2(\delta_3 - \delta_5)] \tag{4.7b}$$
$$F_5 = \frac{-1}{2kM_5}[|q_3|^2(\delta_4 - \delta_6) + |q_4|^2(\delta_6 - \delta_3) + |q_6|^2(\delta_3 - \delta_4)] \tag{4.7c}$$
$$F_6 = \frac{1}{2kM_6}[|q_3|^2(\delta_4 - \delta_5) + |q_4|^2(\delta_5 - \delta_3) + |q_5|^2(\delta_3 - \delta_4)] \tag{4.7d}$$

$$E_3 = \frac{1}{2k}[|q_4|^2(\gamma_5 - \gamma_6) + |q_5|^2(\gamma_6 - \gamma_4) + |q_6|^2(\gamma_4 - \gamma_5)] \tag{4.8a}$$
$$E_4 = \frac{-1}{2kM_4}[|q_3|^2(\gamma_5 - \gamma_6) + |q_5|^2(\gamma_6 - \gamma_3) + |q_6|^2(\gamma_3 - \gamma_5)] \tag{4.8b}$$
$$E_5 = \frac{1}{2kM_5}[|q_3|^2(\gamma_4 - \gamma_6) + |q_4|^2(\gamma_6 - \gamma_3) + |q_6|^2(\gamma_3 - \gamma_4)] \tag{4.8c}$$
$$E_6 = \frac{-1}{2kM_6}[|q_3|^2(\gamma_4 - \gamma_5) + |q_4|^2(\gamma_5 - \gamma_3) + |q_5|^2(\gamma_3 - \gamma_4)] \tag{4.8d}$$

$$H_4 = \frac{1}{kM_4}[\gamma_3(\delta_5 - \delta_6) + \gamma_5(\delta_6 - \delta_3) + \gamma_6(\delta_3 - \delta_5)] \tag{4.9a}$$
$$H_5 = \frac{-1}{kM_5}[\gamma_3(\delta_4 - \delta_6) + \gamma_4(\delta_6 - \delta_3) + \gamma_6(\delta_3 - \delta_4)] \tag{4.9b}$$
$$H_6 = \frac{1}{kM_6}[\gamma_3(\delta_4 - \delta_5) + \gamma_4(\delta_5 - \delta_3) + \gamma_5(\delta_3 - \delta_4)] \tag{4.9c}$$

Now using these eleven parameters, and the powers measured from the four ports of the SPR with the DUT connected $P_{3..6}$, the reflection coefficient of the DUT can be calculated as:

$$\Gamma_{DUT} = \frac{\sum_{i=3}^{6}(F_i + jE_i)\frac{P_i}{P_3}}{1 + \sum_{i=4}^{6} H_i \frac{P_i}{P_3}} \tag{4.10}$$

4.3 Characterization-Based Technique 3:

We refer to Characterization-Based Technique 3 as that of using a nonlinear optimization technique to find Γ_{DUT} as the intersection point in the Γ-plane. Non-linear least squares optimization is applied to find the center point of three intersecting circles (2.47). We employ the Gauss-Newton method, an iterative method specifically designed for solving non-linear least squares optimization, to iteratively refine an initial estimate until an optimal solution is reached to determine the complex reflection coefficient. It approximates the Hessian matrix using the Jacobian, offering a balance between computational efficiency and convergence speed.

The Jacobian matrix plays a crucial role in the optimization process, it is the first-order partial derivatives of a vector-valued function. In non-linear optimization algorithms, such as the Gauss-Newton method mentioned, the Jacobian is used to approximate the Hessian, providing a computationally efficient way to iteratively solve non-linear least squares problems. This approach balances computational cost with convergence speed, making it particularly useful in complex optimization scenarios like determining reflection coefficients in electromagnetic problems.

The goal of the optimization is to determine a point γ, represented as a complex number, which minimizes the sum of squared differences between the radii of three circles and the distances from γ to the centers of these circles. This can be mathematically expressed as:

$$\min_{\gamma} \sum_{i=1}^{3} \left(R_i^2 - \left(\left(\mathrm{Re}(\gamma) - C_{x,i}\right)^2 + \left(\mathrm{Im}(\gamma) - C_{y,i}\right)^2\right)\right)^2 \tag{4.11}$$

where R_i are the radii, and $(C_{x,i}, C_{y,i})$ are the center coordinates of the three circles. The Jacobian matrix J is calculated as $J_1 = \frac{\partial F}{\partial x1}$ and $J_2 = \frac{\partial F}{\partial x2}$. It represents the first order partial derivatives of the residual functions with respect to the real and imaginary parts of γ:

$$J_{i,1} = -2\big(\mathrm{Re}(\gamma) - C_{x,i}\big) \tag{4.12}$$
$$J_{i,2} = -2\big(\mathrm{Im}(\gamma) - C_{y,i}\big) \tag{4.13}$$

The residual vector ΔY is computed, representing the difference between squared radii and squared distances:

$$\Delta Y_i = R_i^2 - \Big(\big(\mathrm{Re}(\gamma) - C_{x,i}\big)^2 + \big(\mathrm{Im}(\gamma) - C_{y,i}\big)^2\Big) \tag{4.14}$$

The current estimate of γ is then updated using Tikhonov regularization which reduces over-fitting and improves the conditioning of the problem by adding regularization parameter (λ) which controls the strength of the regularization. It is a very small value near to zero, in all results mentioned in this thesis we use $1e^{-10}$. We can optimize without it as well, but it might result in an overly complex solution which is not required so we add a regularization constant to prevent over-fitting and improve the stability by imposing an additional constraint:

$$\Delta\beta = (J^T J + \lambda I)^{-1} J^T \Delta Y \tag{4.15}$$

$$\gamma_{\text{new}} = \gamma_{\text{old}} - (\Delta\beta_1 + i\Delta\beta_2) \tag{4.16}$$

Then we check for convergence by evaluating the updated γ .The convergence level we selected was $|\gamma_{\text{new}} - \gamma_{\text{old}}|$< 1e-10. If this condition is met the optimization process stops. The point of convergence is Γ_{DUT}.

4.4 Calibration Technique 1

So far we have described characterization-based techniques which require an accurate measurement of S^6 for the six-port circuit upon which the SPR is built. Even when we have such a characterization, as has already been mentioned, the direct calculation of the reflection coefficient (Γ_{DUT}) is challenging due to the complex relation (2.49) between the C_i(center of the circles) points, power readings, and the device under test (DUT) connected to the six-port circuit's port 2. In a typical six-port reflectometer, the three C_i points that characterize the circuit are not fixed but vary based on the power readings in the Γ-plane. These readings are directly influenced by the load connected to the measuring port. The C_i points depend on the power readings (2.49), which in turn depend on the DUT's reflection coefficient. This interdependence makes solving the nonlinear equations for Γ_{DUT} impractical in real-world scenarios.

In addition, if the S^6 changes due to environmental considerations, it becomes very difficult to remeasure the S^6 in the field. To overcome this challenge, calibration techniques for the six-port reflectometer have been developed. One of the first calibration techniques to be proposed was that by Engen [10] and is widely known as "Six to Four Port Calibration technique". Over time researchers have introduced various improved versions but this remains one of the most robust techniques to-date [2], [4], [39], [42]. It breaks the process of obtaining the reflection co-efficient into two parts, first finding an embedded reflection coefficient 'w' followed by a determination of the actual reflection co-efficient 'Γ' which is the SOL error-box corrected version of 'w'. The SOL error-box correction is also known as that of performing a "Bi-Linear transformation" details of which are discussed in this Section.

For the first step of this calibration of the SPR (that of getting 'w') we don't need to know the values of the loads. We can use any set of 9 unknown but different loads. For the error-box calibration we still need the known SOL loads (with known short-open-load reflection coefficients). The SOL 'error-box' correction is applied to the obtained 'w' to find 'Γ'. Figure 13 shows the bi-linear transformation for the 9-load calibration technique.

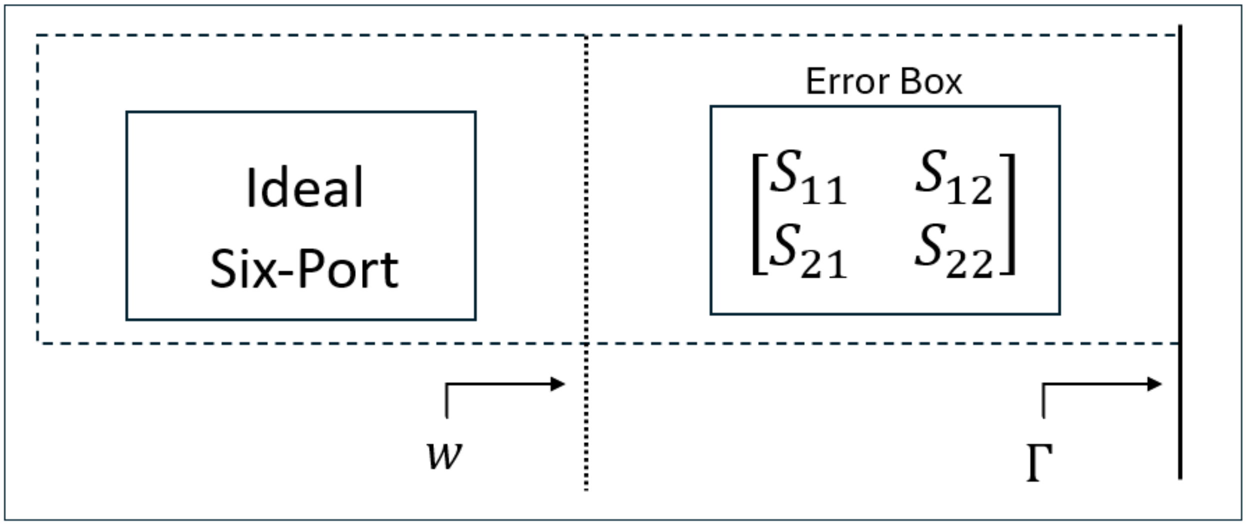

Figure 13: Bi-linear transformation for 9-load technique

Engen [10] shows that the ideal six-port (which he refers as a 4-port in his paper) can be represented by five real numbers, which we (following Ghannouchi et al. [[4], Section 4.4] call '*r, q, s, A5, A6*'. Ghannouchi et al. performs a set of mathematical manipulations that shows how we can obtain '*r, q, s, A5, A6'*. Using (4.17) and measuring nine different loads results in the matrix system (4.18) which relates the x_i-coefficients with the variables leading to calculation of 'w'. Once we have obtained the x_{i} , Ghannouchi et al. [4] shows that we can find '*r, q, s, A5, A6*' from the equations (4.19), the characterization process is complete for obtaining 'w'. However, this gets us only to 'w' (see Figure 8). We still need to perform calibration by obtaining the parameters of our error box (*c, d, e*). This is done through SOL calibration.

Consider normalized powers p_i's at port i=4,5,6 for all the 9 loads measured using the SPR

(4.17) shows the relation between x_i and p_i. This

$$x_1p_4^2 + x_2p_5^2 + x_3p_6^2 + x_4p_4p_5 + x_5p_5p_6 + x_6p_5p_6 + x_7p_4 + x_8p_5 + x_9p_6 = -1 \qquad (4.17)$$

Writing these nine equations in matrix form with nine equations and nine unknown linear variables x_i , we get:

$$\begin{bmatrix} p_{41}^2 & p_{51}^2 & p_{61}^2 & p_{41}p_{51} & p_{51}p_{61} & p_{41} & p_{51} & p_{61} \\ p_{42}^2 & p_{52}^2 & p_{62}^2 & p_{42}p_{52} & p_{52}p_{62} & p_{42} & p_{52} & p_{62} \\ p_{43}^2 & p_{53}^2 & p_{63}^2 & p_{43}p_{53} & p_{53}p_{63} & p_{43} & p_{53} & p_{63} \\ p_{44}^2 & p_{54}^2 & p_{64}^2 & p_{44}p_{54} & p_{54}p_{64} & p_{44} & p_{54} & p_{64} \\ p_{45}^2 & p_{55}^2 & p_{65}^2 & p_{45}p_{55} & p_{55}p_{65} & p_{45} & p_{55} & p_{65} \\ p_{46}^2 & p_{56}^2 & p_{66}^2 & p_{46}p_{56} & p_{56}p_{66} & p_{46} & p_{56} & p_{66} \\ p_{47}^2 & p_{57}^2 & p_{67}^2 & p_{47}p_{57} & p_{57}p_{67} & p_{47} & p_{57} & p_{67} \\ p_{48}^2 & p_{58}^2 & p_{68}^2 & p_{48}p_{58} & p_{58}p_{68} & p_{48} & p_{58} & p_{68} \\ p_{49}^2 & p_{59}^2 & p_{69}^2 & p_{49}p_{59} & p_{59}p_{69} & p_{49} & p_{59} & p_{69} \end{bmatrix} \begin{bmatrix} x_1 \\ x_2 \\ x_3 \\ x_4 \\ x_5 \\ x_6 \\ x_7 \\ x_8 \\ x_9 \end{bmatrix} = \begin{bmatrix} -1 \\ -1 \\ -1 \\ -1 \\ -1 \\ -1 \\ -1 \\ -1 \\ -1 \end{bmatrix} \qquad (4.18)$$

We can use more than 9 loads and solve (4.18) using least-squares to improve the result. From the $x_{1\ldots9}$, we can calculate our five real parameters (*r, q, s, A5, A6*) to find an initial guess of the 'w' in our linear system. These five parameters are obtained from the following equations

$$r = \frac{2x_5 - x_7x_9}{2x_1x_9 - x_5x_7} \qquad (4.19a)$$

$$q = \frac{2x_4 - x_7x_8}{2x_1x_8 - x_4x_7} \qquad (4.19b)$$

$$s = \frac{2x_5 - x_7x_9}{2x_1x_9 - x_5x_7} + \frac{2x_4 - x_7x_8}{2x_1x_8 - x_4x_7} + \frac{x_7}{x_1} \qquad (4.19c)$$

$$A_5 = \left(x_2 \left(\frac{2x_5 - x_7x_9}{2x_1x_9 - x_5x_7} + \frac{2x_4 - x_7x_8}{2x_1x_8 - x_4x_7} + \frac{x_7}{x_1} \right) \left(\frac{2x_5 - x_7x_9}{2x_1x_9 - x_5x_7} \right) \right)^{\frac{1}{4}} \qquad (4.19d)$$

$$A_6 = \left(x_3\left(\frac{2x_5 - x_7x_9}{2x_1x_9 - x_5x_7} + \frac{2x_4 - x_7x_8}{2x_1x_8 - x_4x_7} + \frac{x_7}{x_1}\right)\left(\frac{2x_4 - x_7x_8}{2x_1x_8 - x_4x_7}\right)\right)^{\frac{1}{4}} \quad (4.19e)$$

Once we have these 5 parameters we can find the real and imaginary of our embedded reflection coefficient 'w'. Note that the p_4, p_5, p_6 in (4.20) are the normalized powers (with p_3) of the DUT.

$$\mathrm{Re}(w) = \frac{p_4 - A_5^2 p_5 + \mathrm{r}}{2\sqrt{r}} \quad (4.20a)$$

$$\mathrm{Im}(w) = \frac{\pm 1}{\sqrt{1 - z^2}}\left(\frac{p_4 - A_6^2 p_6 + \mathrm{q}}{2\sqrt{q}} + \frac{z(p_4 - A_5^2 p_5 + \mathrm{r})}{2\sqrt{r}}\right) \quad (4.20b)$$

where $z = \frac{-q-r+s}{2\sqrt{qr}}$

The sign ambiguity can be resolved using a partially known reflection coefficient (although we tested in our simulation models, and it doesn't make any difference). This is followed by the SOL error-box correction.

4.5 SOL Error-box Correction Technique:

It is important to note here that the SOL correction technique can be performed in combination with any SPR characterization technique by replacing 'w' with the Γ calculated with that respective technique. In this section we continue with 'w' for simplicity. The ideal reflection coefficient 'w' can be related with the DUT's reflection coefficient Γ by the following linear transformation [14]:

$$w = \frac{d\Gamma + e}{c\Gamma + 1} \quad (4.21)$$

The complex correction coefficients *c*, *d* and *e*, model the transition between the measuring plane of an ideal six-port reflectometer (whose reflection coefficient is 'w') and the measuring plane at the DUT. To calculate the correction coefficients *c*, *d* and *e* we obtain three linear complex equations from (4.21) and write them in matrix form:

$$\begin{bmatrix} -w^{\text{short}} & \Gamma_{\text{short}} & -1 \\ -w^{\text{open}} & \Gamma_{\text{open}} & -1 \\ -w^{\text{load}} & \Gamma_{\text{load}} & -1 \end{bmatrix} \begin{bmatrix} c \\ d \\ e \end{bmatrix} = \begin{bmatrix} -w^{\text{short}} \\ -w^{\text{open}} \\ -w^{\text{load}} \end{bmatrix} \tag{4.22}$$

Here w^{short}, w^{open} and w^{load} are the reflection coefficients measured using any calibration or characterization-based method for a short, open and load as DUTs connected at port 2. The Γ_{short}, Γ_{open}, Γ_{load} are the reflection co-efficient of the ideal short, open and load DUTs measured using a benchtop conventional VNA. Once we have obtained the correction coefficients *c*, *d* and *e*, using (4.21), one can easily deduce

$$\Gamma_{DUT} = \frac{e-w}{cw-d} \tag{4.23}$$

Where Γ_{DUT} is the required reflection co-efficient of the DUT. The 'w' in (4.23) is the 'w_{DUT}'.

4.6 Calibration Technique 2

Haddadi et al. [57] proposed a six-port reflectometer-based calibration technique using Fourier analysis and a least square algorithm to incorporate non-linearity and mismatching effects of the power detectors. The technique requires prior knowledge of the real and imaginary parts of the reflection coefficients for eight calibration loads. We should emphasize that in this technique we require the reflection coefficient of the eight loads being used and this would succumb to the same disadvantages as the characterization-based techniques where environmental factors could change these reflection coefficients and therefore we would need to measure the possibly changing Gamma for the loads.

The method starts with the standard equations of the circles for a SPR where P_i are the powers measured at the 4 ports:

$$P_i = C_i|\Gamma_{dut} - q_i|^2 \; i = 3, \dots, 6 \tag{4.23}$$

where
$$C_i = |A_i|^2|b_2|^2 \tag{4.24}$$

and
$$q_i = -\frac{B_i}{A_i} \tag{4.25}$$

where q_i are the centers of the circles and radius $r_i = \sqrt{\frac{P_i}{C_i}}$.

Briefly, Haddadi's method first expands (4.23):

$$P_i = C_i\big(|q_i|^2 + |\Gamma|^2 - 2|q_i||\Gamma|\cos\left(\arg\left(q_i\right) - \arg\left(\Gamma\right)\right)\big) \tag{4.26}$$

Using (4.26) as inspiration, Haddadi expands the representation of the power measured to be dependent not only on |Γ| and $|\Gamma|^2$, but he also adds more terms to the expansion, with unknown weights in front of all terms of Γ^n. In the case of n = 3 (so the powers, Pi depend on |Γ|, $|\Gamma|^2$ and $|\Gamma|^3$, we can solve for the weights in front of each $|\Gamma|^{\mathrm{n}}$, by solving a matrix system. In this equation $|q_i|^2$ and $|\Gamma_{dut}|^2$ define the rectified signal while the last term $2|q_i||\Gamma|\cos\left(\arg\left(q_i\right) - \arg\left(\Gamma\right)\right)$ defines a relation between reflected signal (Γ_{dut}), arg (Γ_{dut}).

Now to create a mathematical model Haddadi et.al performs a spatial Fourier transform on (4.26) to incorporate mismatching and non-linear effects. Although higher order terms can be introduced in the system to account for non-linearities but for simplicity Haddadi considers a third-order model for Γ_{dut}. He splits Γ_{dut}, in the real part *I* and imaginary part Q . With appropriate mathematical manipulations we can write the non-linear model of the powers at each measurement port of the SPR, accounting for mismatching and non-linear effects given by:

$$P - Y \cdot \Gamma = 0 \tag{4.27}$$

This can be written in matrix form as:

$$P = \begin{bmatrix} P_3 \\ P_4 \\ P_5 \\ P_6 \end{bmatrix} \tag{4.28}$$

$$Y = \begin{bmatrix} y_{30} & y_{31} & y_{32} & y_{13} & y_{34} & y_{15} & y_{36} & y_{37} \\ y_{40} & y_{41} & y_{42} & y_{23} & y_{44} & y_{25} & y_{46} & y_{47} \\ y_{50} & y_{51} & y_{52} & y_{33} & y_{54} & y_{35} & y_{56} & y_{57} \\ y_{60} & y_{61} & y_{62} & y_{43} & y_{64} & y_{45} & y_{66} & y_{67} \end{bmatrix} \tag{4.29}$$

$$\Gamma = \begin{bmatrix} 1 \\ I \\ Q \\ I^2 \\ Q^2 \\ IQ \\ I^3 - 3IQ^2 \\ Q^3 - 3I^2Q \end{bmatrix} \tag{4.30}$$

The Y-matrix contains all the parameters ‘y’ which characterize the SPR. Our goal is to obtain the y-parameters for our SPR, and this can be done by measuring powers at the four ports of the SPR for 8 calibration loads. The key to this process is that we should know the true I and Q for these loads. Once we have the 8 sets of powers and Γ, solve the 32 y’s in (4.29). If we wanted to perform a higher-order approximation of Γ, or if we wanted to solve this matrix system in a least-squares sense, then we could add more calibration loads.

Once we have the y-parameters, the calibration process is complete. The next step is to solve for the Γ_{dut}. First, we measure the powers associated with the DUT. The process of going from powers to Γ_{dut} is not straight forward because of the non-linear relation to the I and Q. To do this Haddadi et.al suggest the use of Newton Raphson method. We use the first order model of (4.27) to find the initial guess Γ_0(I, Q), using (4.31).

$$P_i - y_{i0} + y_{i1}I + y_{i2}Q + \frac{y_{i3}+y_{i4}}{2}(I^2 + Q^2) = 0,\ i = 3, \ldots, 6. \tag{4.31}$$

This is first solved by treating I, Q , I^2, Q^2 as four independent variables to solve the linear matrix system. Next, we re-write (4.27) as:

$$P_i(I, Q) = y_{i0} + y_{i1}I + y_{i2}Q + y_{i3}I^2 + y_{i4}Q^2 + y_{i5}IQ + y_{i6}(I^3 - 3IQ^2) + y_{i7}(Q^3 - 3I^2Q)$$

(4.32)

Haddadi expands (4.32) in Taylor series as a function of partial derivatives.

$$P_i(I + \delta I, Q + \delta Q) = P_i(I, Q) + \frac{\partial P_i(I,Q)}{\partial I}\partial I + \frac{\partial P_i(I,Q)}{\partial Q}\partial Q + O(\partial I^2, \partial Q^2) \tag{4.33}$$

$$\frac{\partial P_i(I, Q)}{\partial I} = y_{i1} + 2y_{i3}I + y_{i5}Q + y_{i6}(3I^2 - 3Q^2) - 6y_{i7}IQ \tag{4.34}$$

$$\frac{\partial P_i(I, Q)}{\partial Q} = y_{i2} + 2y_{i4}Q + y_{i5}I - 6y_{i6}IQ + y_{i7}(3Q^2 - 3I^2) \tag{4.35}$$

We use Gauss-Newton method instead of Newton-Raphson to find the Γ(I, Q) from equations above. Equations (4.34) and (4.35) are the Jacobian. In Gauss-Newton method, we use the 2nd order Taylor expansion where we approximate the 2nd order derivative with $J^{\mathrm{T}} * J$.

$$\delta I = \frac{\left(P_3(I,Q)\frac{\partial P_5(I,Q)}{\partial Q} - P_5(I,Q)\frac{\partial P_3(I,Q)}{\partial Q}\right)}{\det} \tag{4.36}$$

$$\delta Q = \frac{\left(P_5(I,Q)\frac{\partial P_3(I,Q)}{\partial I} - P_3(I,Q)\frac{\partial P_5(I,Q)}{\partial I}\right)}{\det} \tag{4.37}$$

$$\det = \frac{\partial P_5(I,Q)}{\partial I}\frac{\partial P_3(I,Q)}{\partial Q} - \frac{\partial P_3(I,Q)}{\partial I}\frac{\partial P_5(I,Q)}{\partial Q} \tag{4.38}$$

$$\Gamma_{n+1} = I_{n+1+}jQ_{n+1} \tag{4.39}$$

$$I_{n+1} = I_n + \delta I \tag{4.40}$$

$$Q_{n+1} = Q_n + \delta Q \tag{4.41}$$

We keep repeating the iteration process until we reach a local minimum, and the answers don't change anymore. We do this by measuring the difference between the last two computed values and once the difference is close to our criteria (1e-8 in our case) we stop iterating.

5 Six-port Reflectometer Simulation and Hardware

In this Chapter we validate the design and testing of the six-port reflectometer architecture we selected (Figure 6) and the performance of the characterization and calibration techniques described in Chapter 4. First, we verify the results in simulation and then on our custom hardware. Keysight Advanced Design System ADS software is used for simulation along with MATLAB software.

5.1 Simulation of the SPR:

The schematic of the SPR simulated in the Advanced Design System (ADS) software from Keysight Technologies is shown in Figure 14. As can be observed in Figure 14 the design consists of four quadrature hybrid couplers, a Wilkinson power divider and an attenuator [2]. The co-planar waveguides have been optimized for appropriate electrical length to manage our q_i points as we explained in Section 2.7 and plotted them in Figure 7.

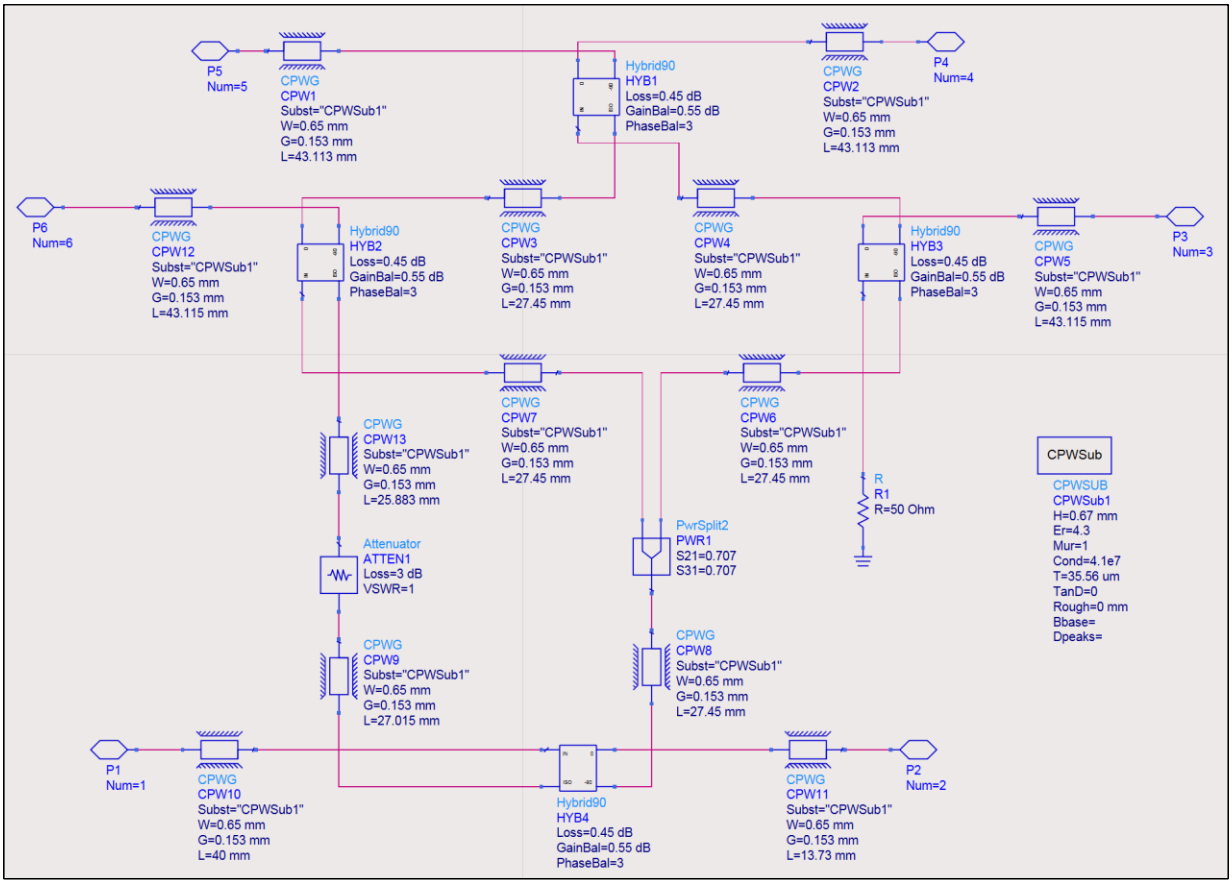

Figure 14: ADS schematic of the SPR design architecture

To compare the performance of all the measurement techniques mentioned in this thesis (Chapter 4) to find the reflection co-efficient (Γ_{dut}) of our DUT, we compare them to the true magnitude and phase of the Γ_{dut} as simulated using ADS. To implement characterization-based techniques in ADS for each Γ_{dut}, we first record the S-parameters of the SPR using the s-parameter simulator and also record the true reflection coefficient of the DUT to be used as a comparison.

Then we record the power measurements $P_{3..6}$ at each port of the SPR using power measurement probes in ADS. Figure 15 shows the power measurement setup of the SPR in ADS.

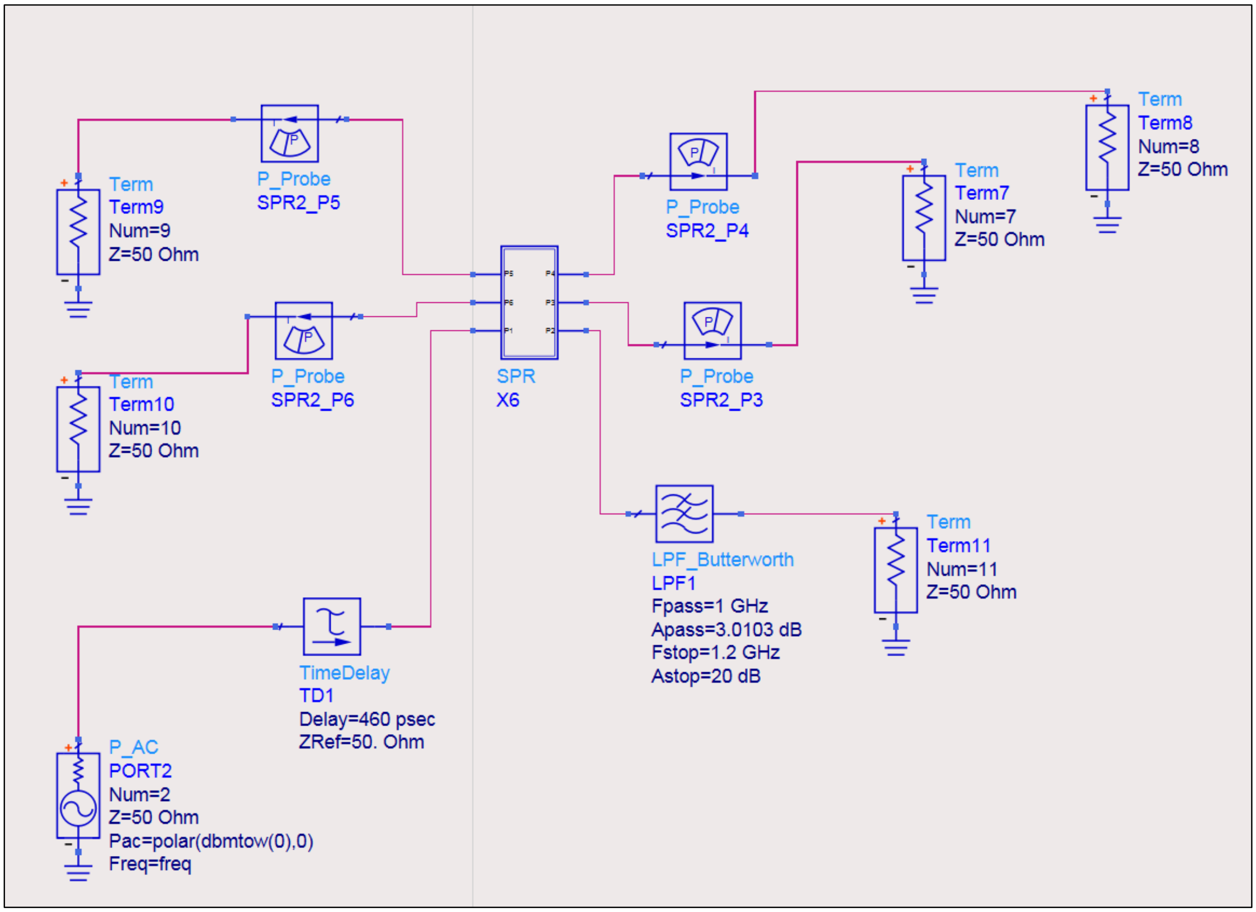

Figure 15: Power and S6 measurement setup of the SPR in ADS

We have tested the performance on various DUT's and the performance of the different techniques have been similar among all of them. Some example DUT's are transmission lines, attenuators and different high-pass and low-pass filters. For simplicity we only present the results of a low-pass filter terminated with a 50-ohm load as the DUT. Figure 16 shows the comparison between the performance of calibration technique 1 (9-loads) and calibration technique 2 (8loads) with SOL error correction in ADS.

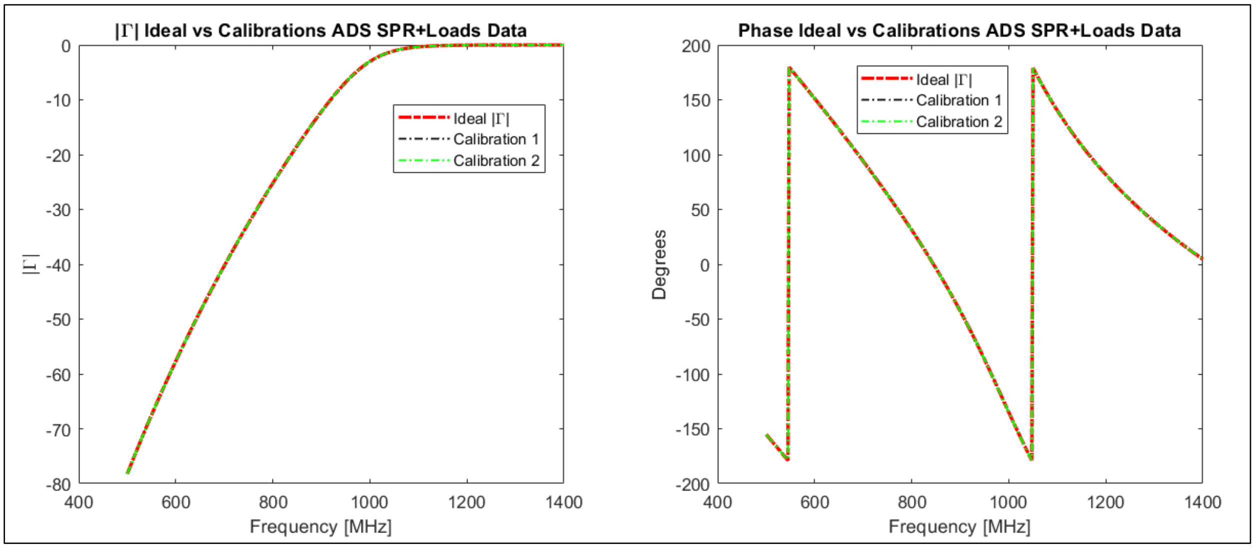

Figure 16: Comparison of Calibration 1,2 for SLP1000 in ADS Simulation

We can observe that both the calibration techniques perform well on simulation data. Figure 17 shows the comparison between the magnitude and phase of the Γ_{dut} for the calculated using the Characterization techniques 1 (Geometrical solution), 2 (Aboud's 11 parameters solution) and 3 (Non-linear optimization).

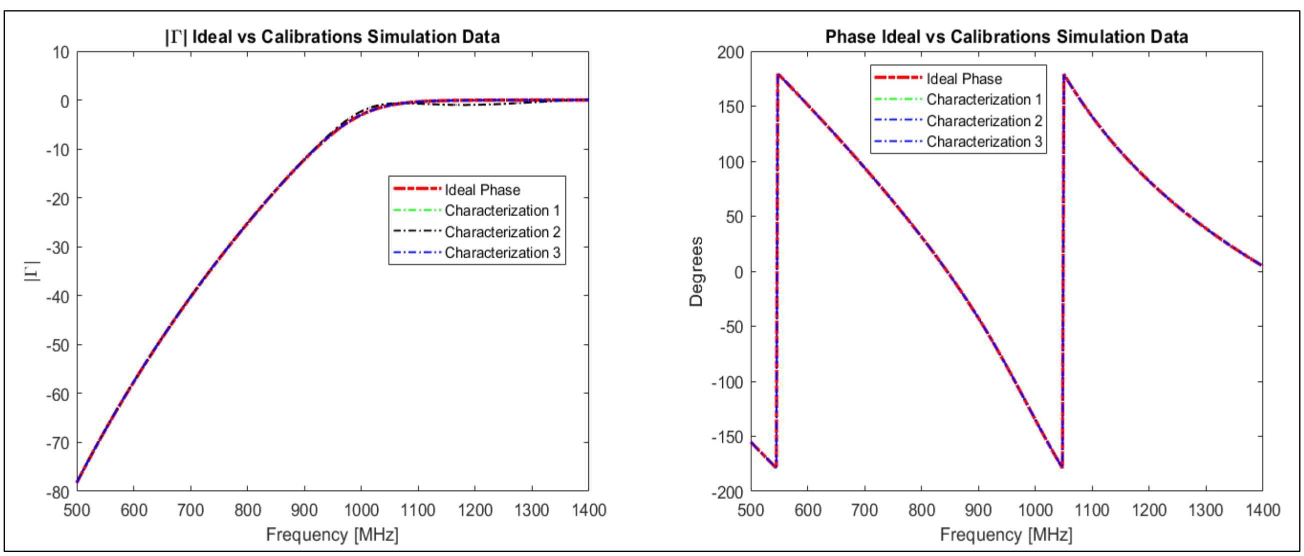

Figure 17: Simulation Data Comparison for a low-pass filter DUT using Techniques 1, 2, 3

It can be observed that all the techniques provide similarly good results in a simulation environment which match with the S_{11} measured using the VNA simulator in ADS software labelled as 'Ideal' in the plots. While characterization techniques 1(geometrical) and 3(non-linear optimization) shows perfect results, we can observe that in characterization technique 2 (Aboud's method) there is a magnitude error of ±0.1 dB. Apart from this, we can observe from the results in Figure 16 and Figure 17, that all the calibration and characterization techniques have similar performance.

5.2 Hardware of Six-port Reflectometer

Six-port Junctions can be manufactured using various fabrication technologies depending on the application. Since these are microwave passive circuit elements so we can use techniques such as microwave integrated circuits, monolithic microwave integrated circuits or monolithic hybrid microwave integrated circuits.

In the microwave integrated circuits (MIC), we mount the passive devices onto the substrate. The substrate is a low-loss, non-conducting material such as FR4 or RTR Droid. As compared to other fabrication techniques (MMIC, HMIC), these circuits are usually more robust, low-cost and easy to fabricate. This fabrication technique is ideal for applications requiring frequencies less than 20GHz [4].

The monolithic microwave integrated circuit (MMIC) technology has the passive devices printed on the substrate and the active devices are fabricated. It has smaller circuit size and high cost of manufacturing as compared to MIC and HMIC fabrication technologies. It supports designs up to 100 GHz [4].

In this thesis we are reporting on using the hardware SPR module designed by Aboud [2] in our lab, and the focus is to verify and validate the performance of the different SPR schemes that have been described. The SPR module has been designed for the frequency bandwidth of 0.6 to 1.2 GHz. Microwave integrated circuit-based components were used to fabricate the SPR. Altium Design software was used to design the circuit on FR4 substrate. The substrate thickness is 1.6mm, relative dielectric constant 4.3 and conductor thickness 35.56 um. For transmission lines Aboud used the co-planar waveguides (CPWGs) having an impedance of 53 ohms. The co-planar waveguides were designed with a center conductor width of 0.815 mm and gap of 0.2mm. The lengths of the different CPWGs were set according to their required electrical lengths as per the design requirements for optimal q_i-points discussed in Section 2.3 of this thesis.

The MIC components used for building the SPR include a 3 dB quadrature hybrid coupler (Anaren 11035-3s) with 1-2GHz frequency range, 20 dB isolation and 0.45 dB insertion loss with 1.3:1 VSWR (voltage standing wave ratio). A Wilkinson's Power Divider (Anaren PD0922J5050S2HF) was used with a 0.95-2.15 GHz frequency range and with 12 dB isolation and 0.7 dB insertion loss. The 3 dB attenuator (Analog Devices HMC653LP2E) used had a tolerance of ±0.3% with a frequency range from DC-10GHz. A testing CPWG transmission line was added in the hardware to test the impedance to be 53 ohms, this was to check the manufacturers fabrication accuracy. Measurement showed that it is actually 53.6 ohms so the SPR's performance should match the simulation. Figure 18 shows the hardware SPR used in this thesis. The size of our SPR board is 10*10cm.

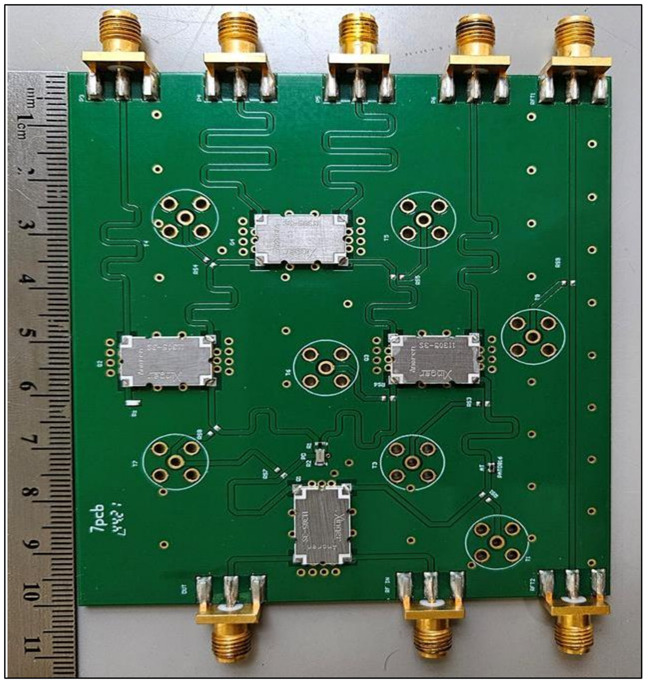

Figure 18: Hardware SPR board

Figure 19 shows the magnitude and phase of the q_i-points of the hardware SPR used in this thesis. Comparing this with the simulation q_i-points in Figure 7 and equation 2.61, we can observe that the magnitude of the q_i-points is not equal as ideally expected for a SPR design and it fluctuates between 1 and 3.5 instead of being a consistent 2. The phase however is very close to the simulated phase. This can be attributed to the imperfections in the fabrication process and the hardware components used.

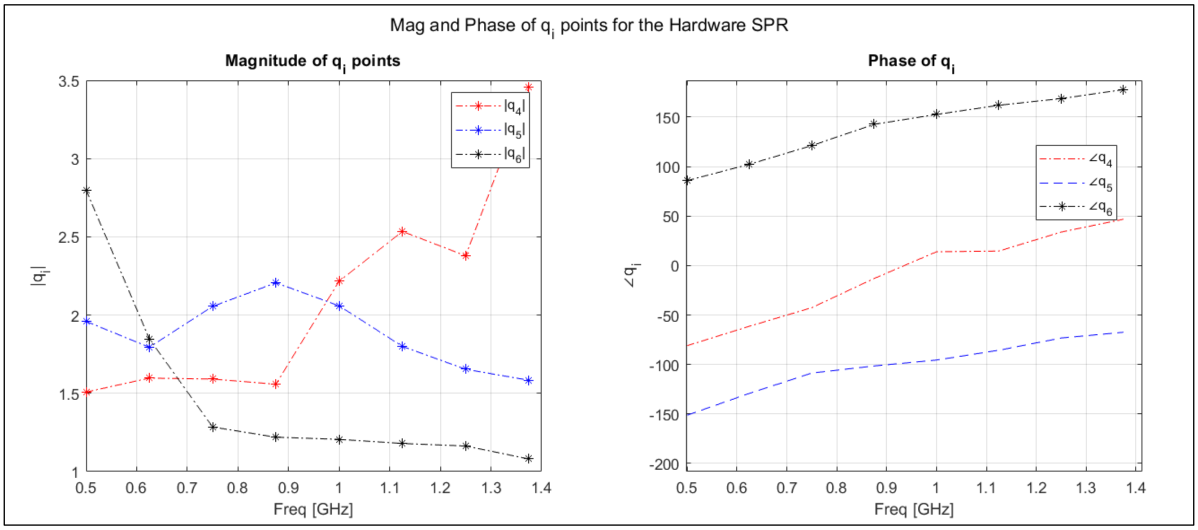

Figure 19: q_i-points of the hardware SPR used in this thesis

For the measurement of our powers at the four ports of SPRs we developed a power detector PCB. The power detector PCB uses four logarithmic voltage detectors (AD8313) configured in their standard configuration (as suggested by the data sheet [58]). The output of these four power detectors is routed to a multi-channel analog to digital converter (MCP3424) along with some resistors and capacitors for noise filtering. Figure 20 shows the schematic of the power detector board. Note that for simplicity, the figure only depicts one power detector, others have been connected similarly with the same ADC converter (MCP3424).

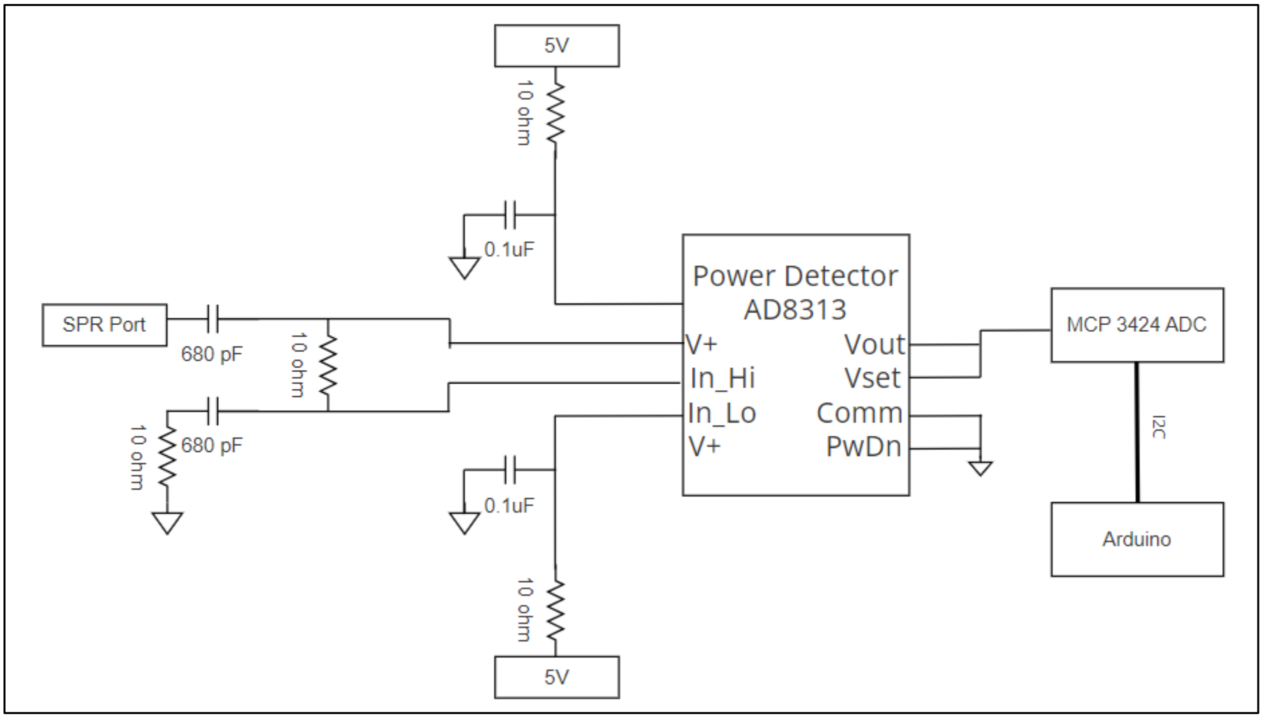

Figure 20: Schematic of Power Measurement Board

It is important to note that the ADC converter (MCP3424) is an 18-bit multi-channel analog to digital converter. We used the 12-bit resolution mode, but the performance was not as good as when we switched to the full 18-bit high accuracy for the power measurements.

The power detectors AD8313 are logarithmic voltage detectors that convert the detected RF signal to an equivalent log-scaled dc value. The power measured by the power detector is calibrated using the power generated by a benchtop RF source at different power output settings. This creates a mapping table of digital numerical values to power values at discrete levels where the calibration was performed. Interpolation is then used to obtain power measurements at intermediary values not found in the table. We used the Agilent E8267D Vector RF signal generator and swept over several powers at frequency points in 2.5 MHz steps in the frequency band of interest using power outputs from -10 to -70 dBm in 5 dB steps. This power range is the limit of our power detectors.

Communication with the ADC is performed using I2C communication protocol through an Arduino UNO microcontroller connected with a laptop. Our power measurement solution is a low-cost alternate to other power detectors used in the literature [17], [48], [61] making our system more affordable than previously developed systems. The power detector board is shown in Figure 21.

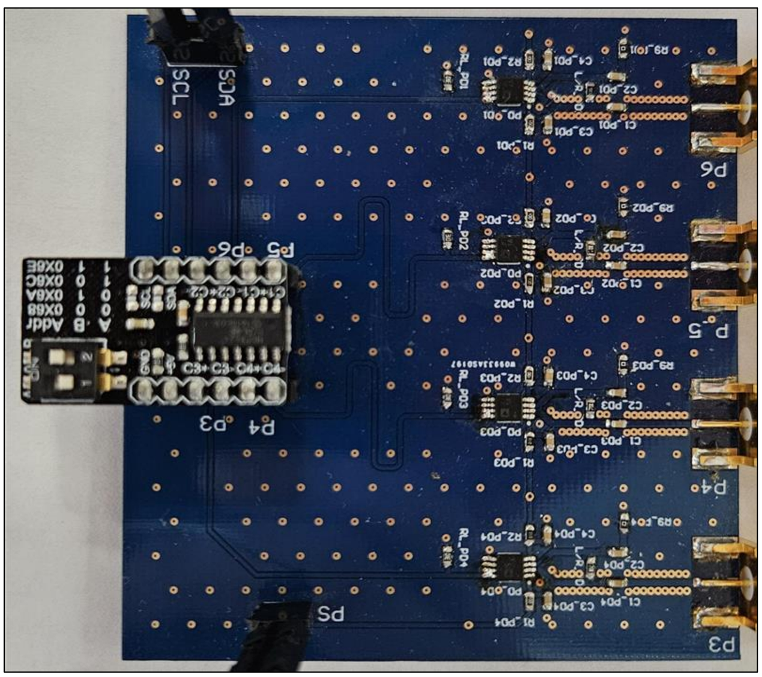

Figure 21: Power Detector Board Hardware prototype

With this hardware setup, we have compared the performance of our SPR measurement techniques. We first compare the characterization techniques for a low-pass filter and a high-pass filter as DUTs. We are using Mini-circuits SHP1000 high pass filter and Mini-circuits LPF1000 low-pass filter terminated with a 50-ohm load.

Recall that characterization technique 1 is the geometrical solution, 2 is the Aboud's method (11 parameters) and 3 is the non-linear least square solution to find the Γ_{dut} as discussed in Chapter 4. The results in Figure 22 shows the comparison of all three characterization-based techniques without SOL and their comparison with the benchtop VNA measured results (labelled as Gamma True) for the SLP 1000 as device under test.

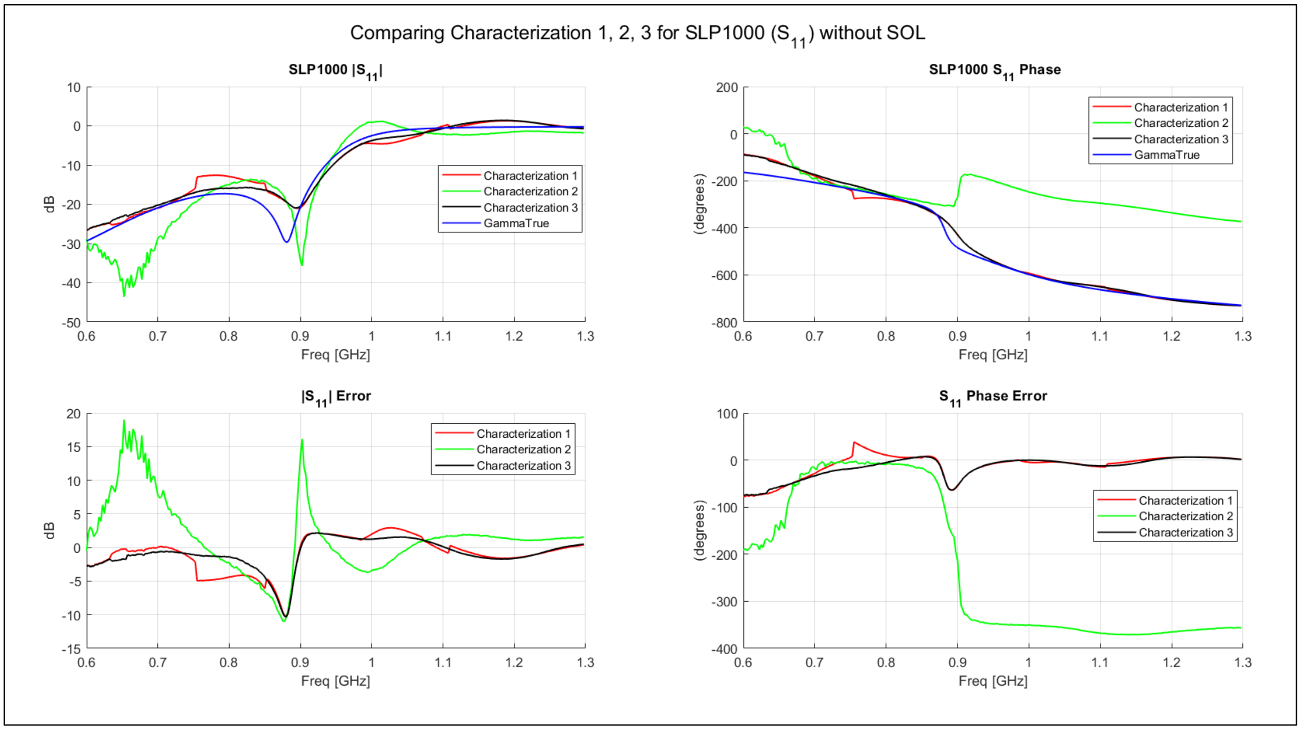

Figure 22: Comparing Characterization Techniques for SLP1000 on hardware SPR

The results in Figure 23 shows the comparison of all three characterization techniques and their comparison with the benchtop VNA measured results (mentioned as Gamma True) for a SHP 1000 as device under test.

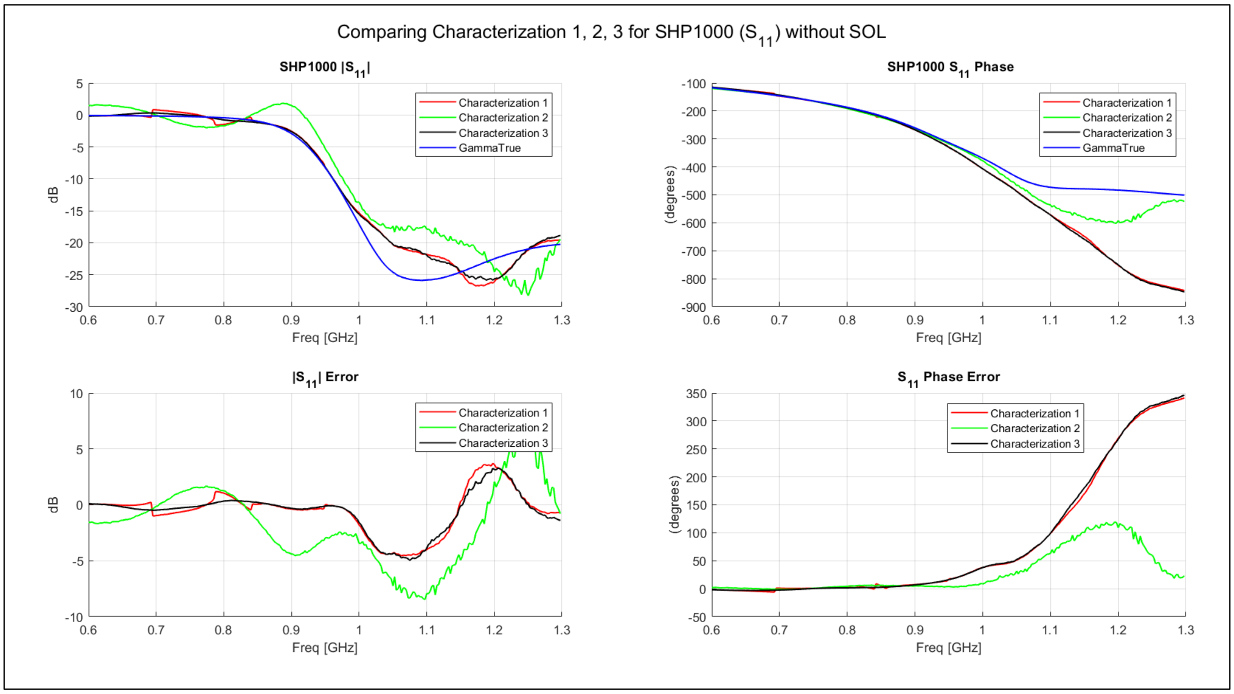

Figure 23: Comparing Characterization Techniques for SHP1000 on hardware SPR

We can observe from both Figure 22 and Figure 23 that none of the techniques used without SOL error-box correction is able to closely match the true S_{11} measured using the benchtop VNA (labelled as 'Gamma Ture' in the figure). We note that characterization-based technique 3 (Non-linear optimization using Gauss Newton) outperforms others.

Now we compare the results after SOL error-box correction. The results after SOL for the high-pass filter (SHP1000) are shown in Figure 24.

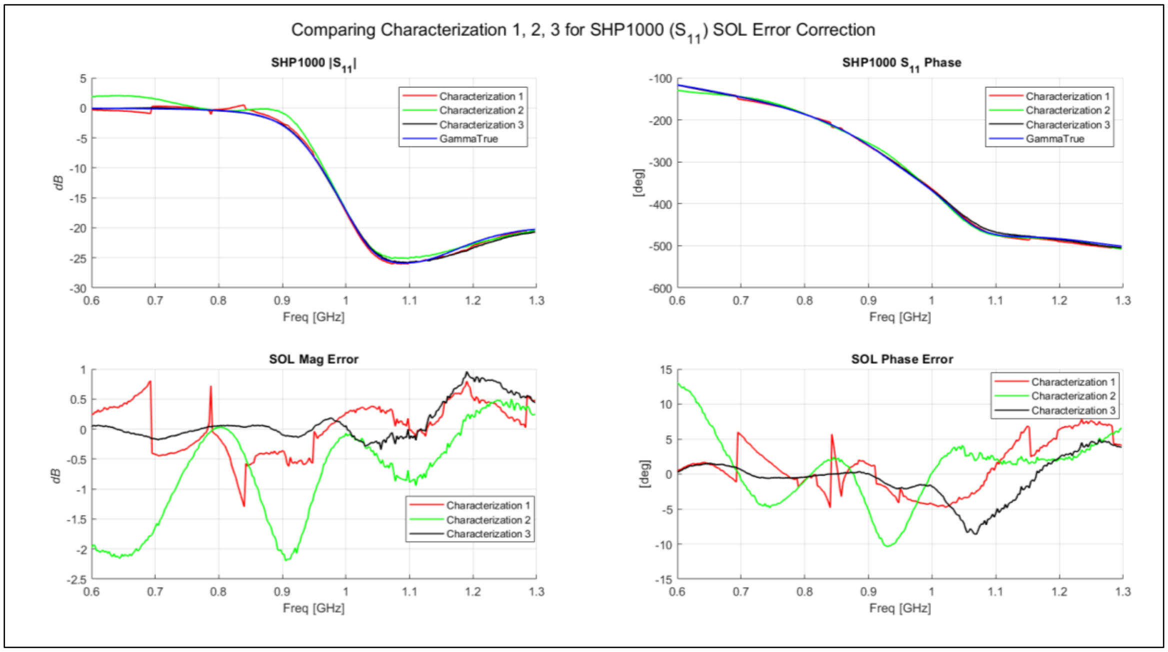

Figure 24: Comparison of Characterization techniques with SOL Correction on SHP1000 DUT

Figure 25 shows the results for the low-pass filter (SLP1000) as the device under test.

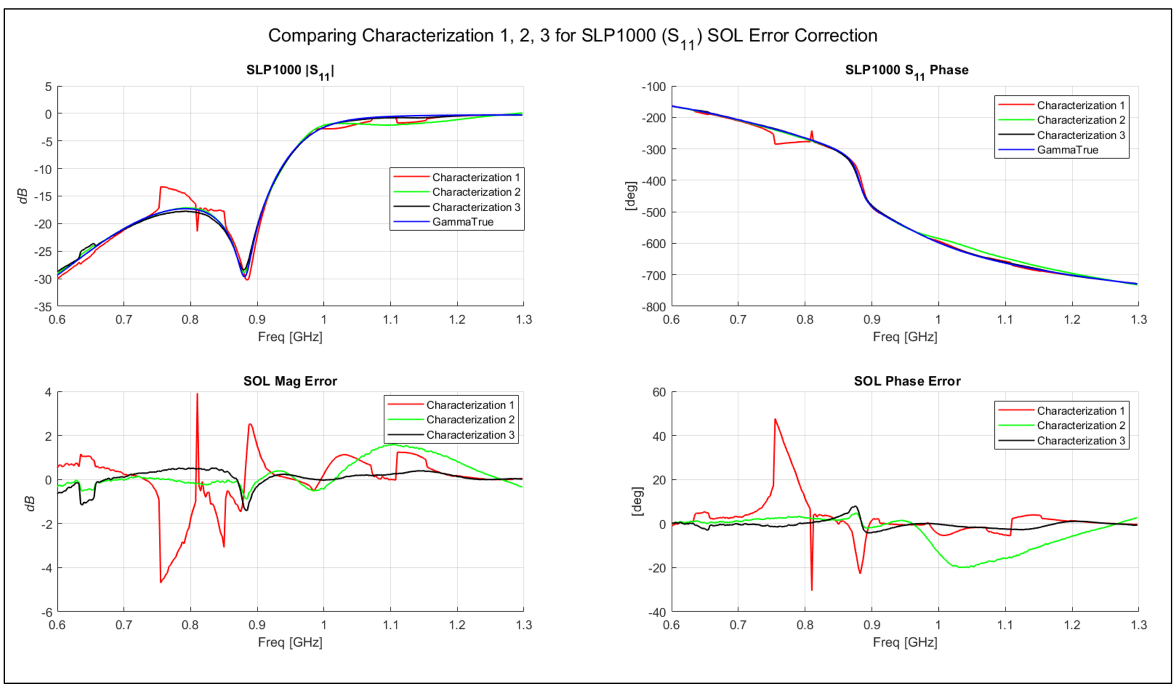

Figure 25: Comparison of Characterization techniques with SOL Correction on SLP1000 DUT

We can observe that SOL error-box correction helps improve our results with the maximum magnitude errors reducing from ±17 dB to ±4 dB. The characterization technique 3 (Gauss-Newton non-linear solution) performs the best with only ±1 dB magnitude error and ±5 degrees phase error for both the devices under test.

Characterization-based method 3 can be implemented assuming matched or unmatched ports, as described in Chapter 2. To better understand the performance between these two modeling approaches we tested Characterization technique 3 (Gauss-Newton nonlinear solution) under both assumptions. Figure 26 shows the results of using Characterization technique 3 assuming matched and unmatched port after SOL error-box correction.

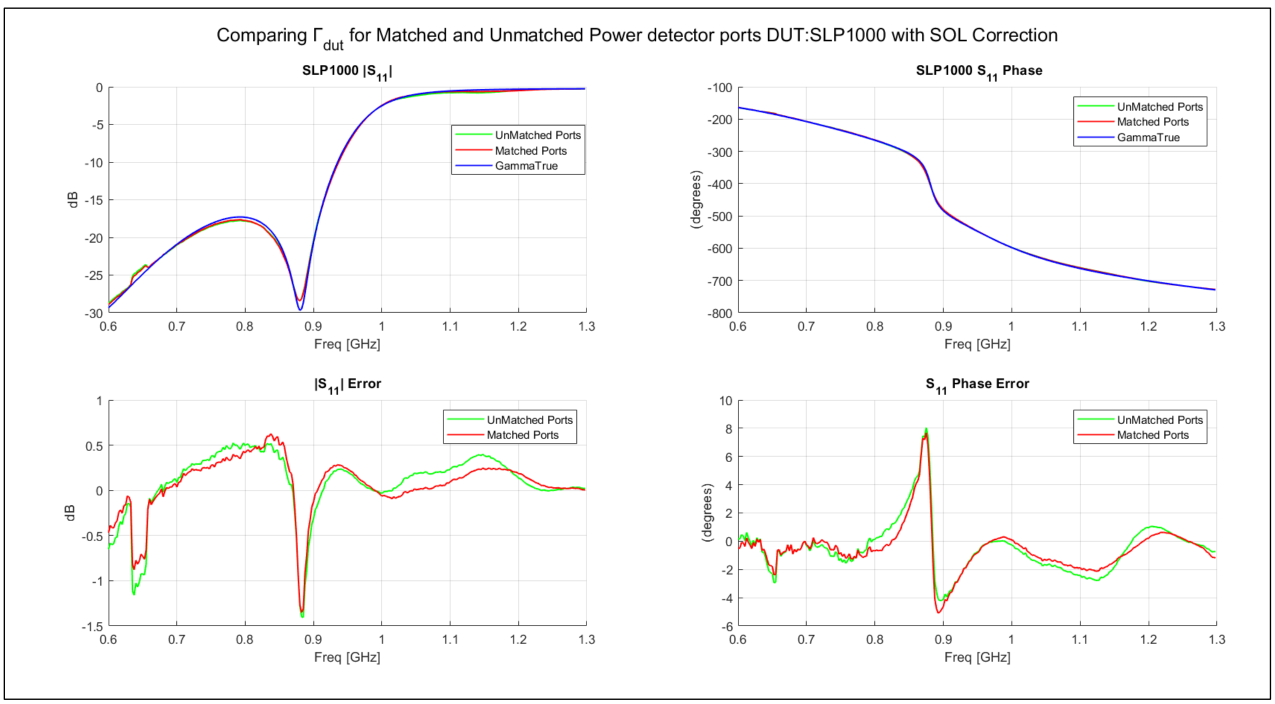

Figure 26: Comparison between matched and unmatched ports for SLP1000 DUT using Technique 3 with SOL

We can observe that the unmatched ports technique works better because the hardware does not have perfectly matched ports, and we need to account for this mismatch.

We, now compare the two calibration methods: calibration 1(8-load) and calibration 2 (9-load) as discussed in Chapter 4. Figure 27 shows the comparison between them. We can observe that none of the Calibration algorithms performs well for our hardware, this could be due to lack of proper load selection or other hardware sensitivities since they give satisfactory results in a simulation as shown before (Figure16).

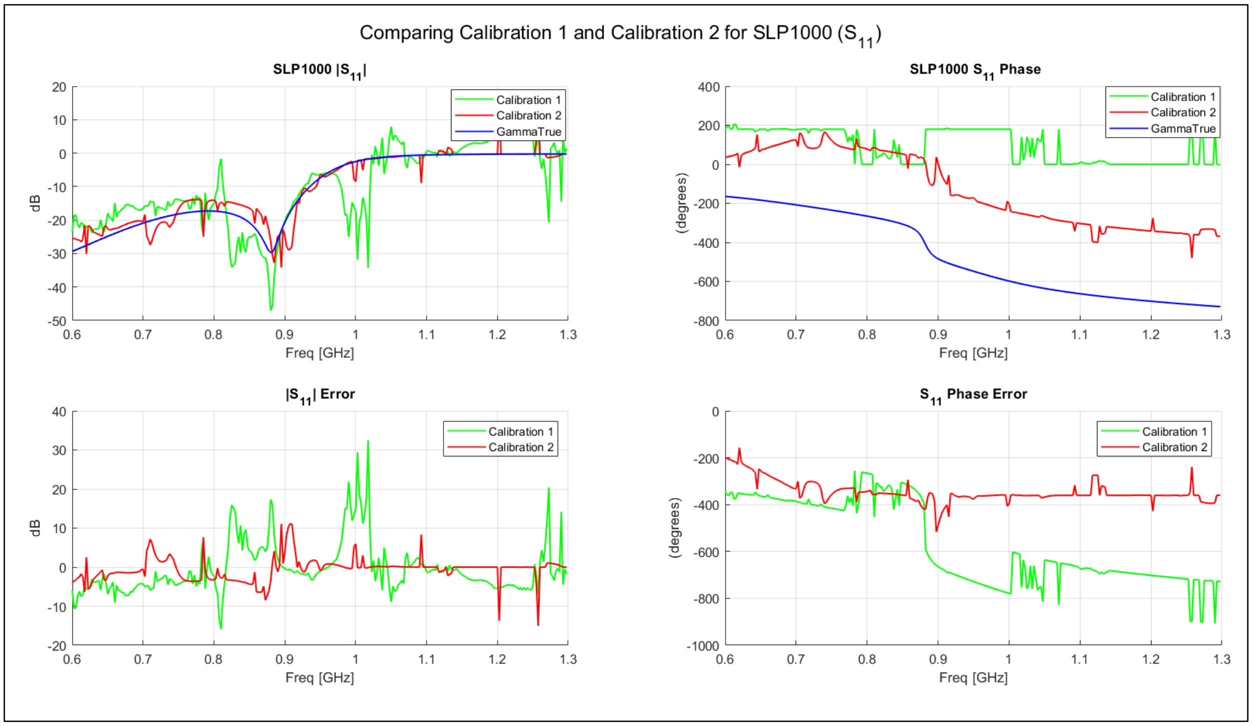

Figure 27: Comparison of Calibration Technique 1 and 2 on Hardware SPR for SLP1000 DUT

From all these comparisons, it can be concluded that characterization technique 3 (Non-linear optimization using Gauss Newton algorithm) outperforms all of the other techniques. Since the SPR-VNA depends on two accurate SPR measurements so we will be using it for our results in the SPR-VNA.

6 Distributed SPR-VNA Simulation and Hardware Results

In this chapter we discuss the performance of our proposed DSPR-VNA and the SPR-VNA. First we discuss the simulation results followed by the hardware results.

6.1 SPR-VNA Simulation:

The simulation results for a distributed two-port SPR-VNA are based on two of the same SPRs designed in the Keysight ADS software. The SPRs have independent RF Power sources and phase shifters were used to shift the phase of one of the SPRs. At least three phase shifts are required to obtain the results (using Equation 3.14, more than three phase shifts lead to an over-determined system that can be solved using least-squares). Since we are simulating ideal components in a controlled simulation environment, our results validate the algorithms and calibration techniques we use. For each SPR-VNA test that will be described, power measurements were taken using the power probes in ADS with different phase shifts applied to the P_AC in Figure 28, this is the AC power source with a configurable phase shift capability and can be used as a signal generator). We calculate three sets of Γ_1 and Γ_2 for each phase shift of the SPR-VNA to calculate S_{12} and S_{21}. We can select any arbitrary phase shift, and it does not need to be known. The key requirement of the phase shifts is that the system of equations represented by (3.14) resulting from these phase shifts has linearly independent rows (i.e. the matrix has a small condition number). The powers of the RF Signal Generators for each SPR can be different as well because it does not make any impact on the results.

Figure 28 shows the schematic diagram of the SPR-VNA we designed for simulation. The phase shifts of 0, 30 and 60 degrees were added in the RF source of SPR1. The frequency range of the simulation is 0.5 to 3 GHz. The results have been validated on various different arbitrary DUTs. For simplicity we only present results for a low-pass filter (SLP2400) as our DUT in this thesis.

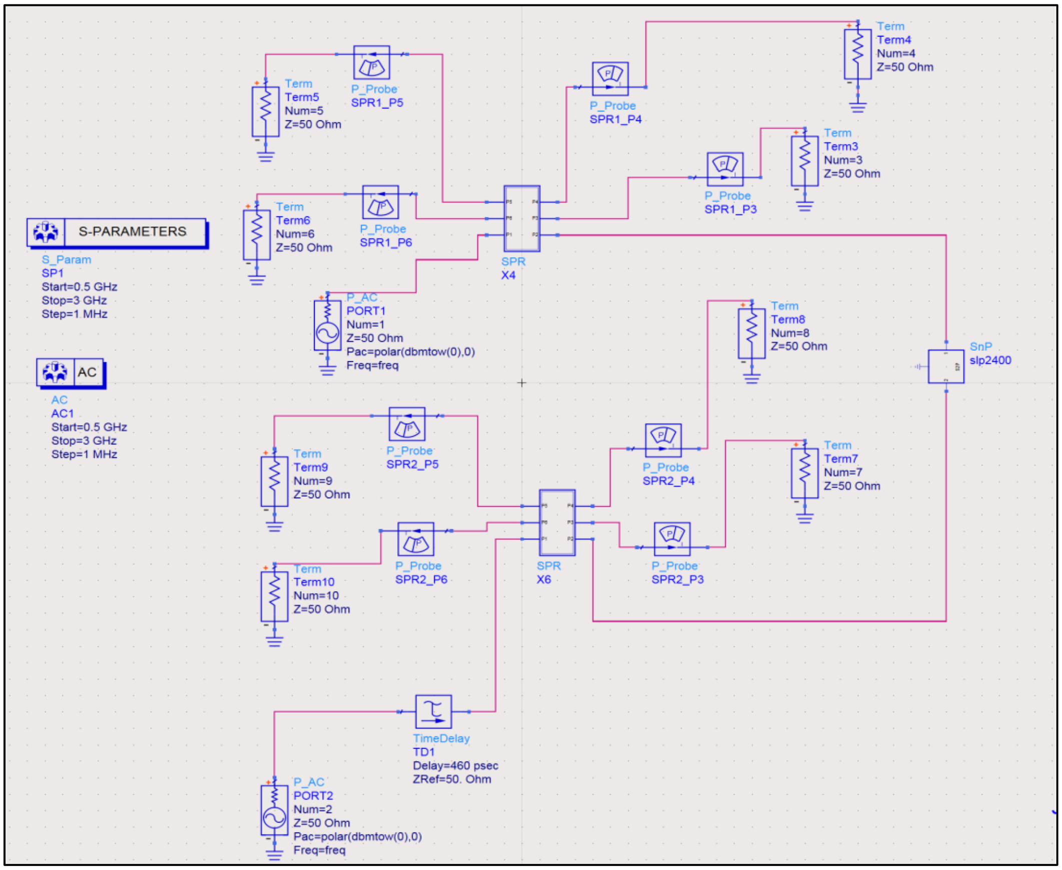

Figure 28: SPR-VNA Simulation schematic in ADS

Figure 29 shows the magnitude and phase of our S_{12} results compared with the true S_{12} measured using ADS. The plots show the comparison between ADS and the DSPR-VNA measured S_{12} magnitude and phase. The ADS values being used as reference are the ADS S-parameter simulation measurements. As was mentioned in Section 5.2, although we have performed the retrieval using all the characterization-based and calibration techniques that have been discussed, here we show result only using Characterization based technique 3 (non-linear solution) for all our DSPR-VNA. In simulation all the other techniques perform the same.

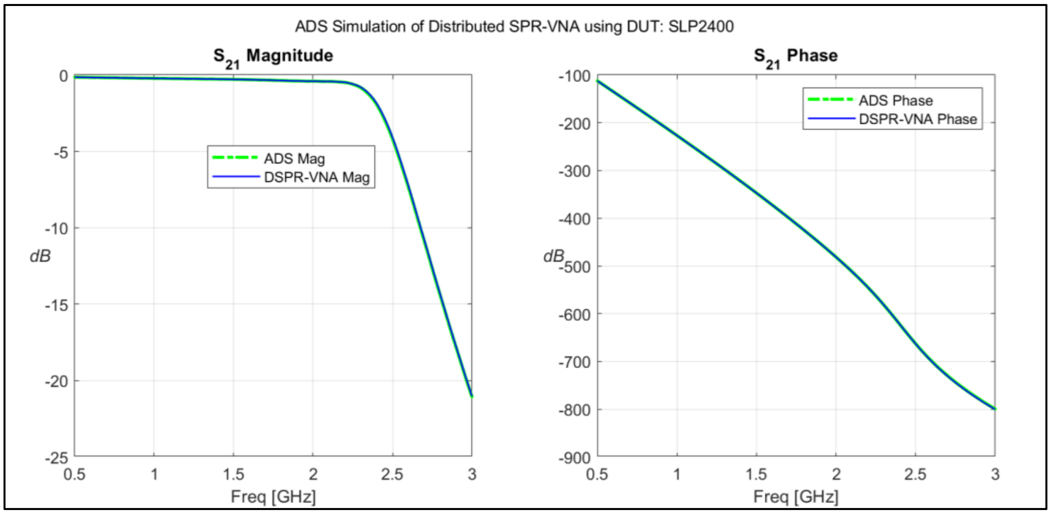

Figure 29: ADS Simulation DSPR-VNA S_12 using SLP2400 DUT

Figure 30 shows the S_{11} of the same setup.

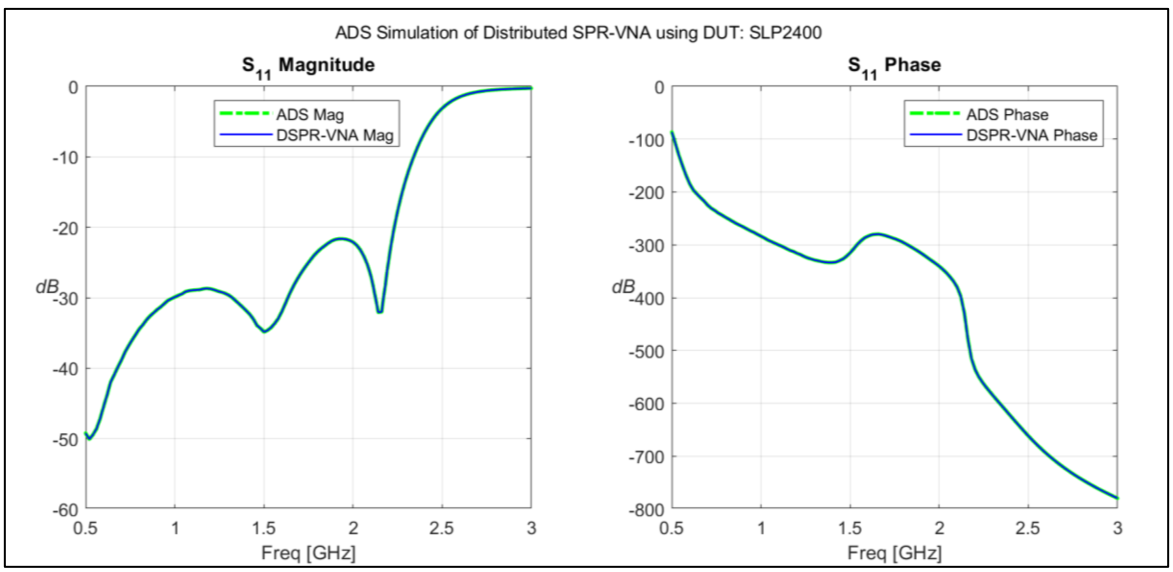

Figure 30: ADS Simulation DSPR-VNA S_11 using SLP2400 DUT

Figure 31 shows the S_{22} of the same setup. The results demonstrate that our design can perform SPR-VNA measurements similar to those of the ADS S-parameter simulation.

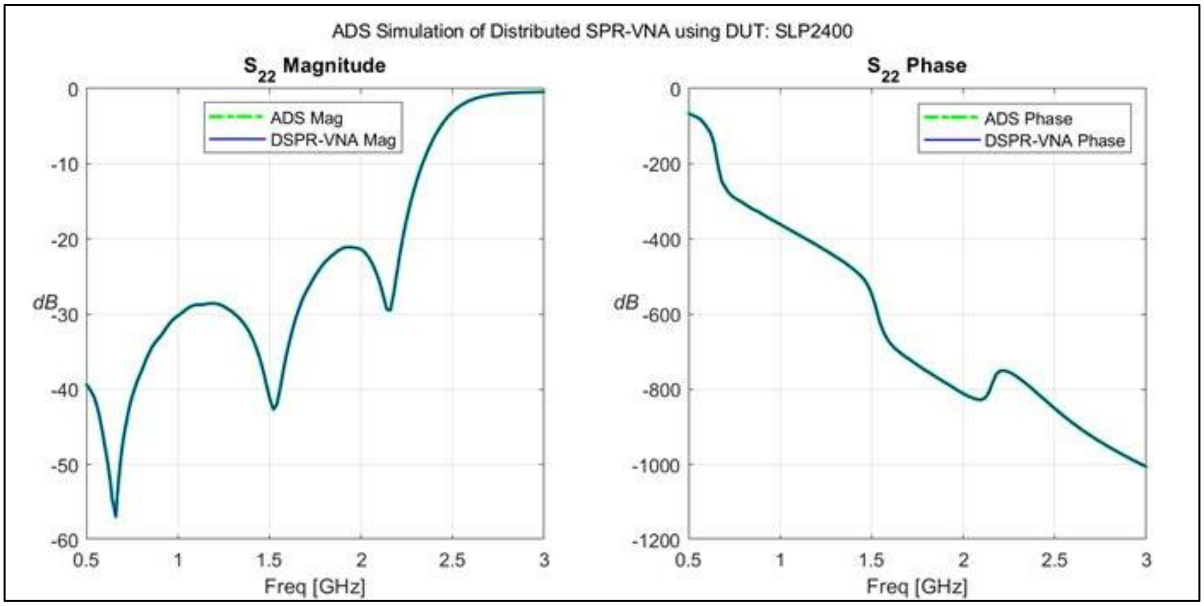

Figure 31: ADS Simulation DSPR-VNA S_22 using SLP2400 DUT

6.2 Using Time Delay for Phase Shifting in a SPR-VNA Application

As described above we need to impose variable phase shifts to the input signal of one SPR to create the SPR-VNA or DSPR-VNA. In ADS simulations this is simply a matter of assigning the phase value to the signal generator. In hardware, one could introduce the phase shifts by switching in transmission lines between the signal generator and the input of the SPR, but this would create a different phase shift at each frequency because the electrical length of the fixed-length transmission lines would be different. Taking advantage of the fact that the only requirement on the phase shifts is that the resulting condition number of Eq. 3.14 be small, here we investigate whether we can simply introduce a quasi-random time-delay on one of the signal generators by turning it on and off.

Thus, we show results of implementing the phase shifts by just switching the input signal sources on with a time difference. Figure 32 shows the DSPR-VNA schematic in ADS with 30 psec (pico-second), 90 psec and 200 psec time-delay between the two RF sources instead of using internal phase-shift of the sources. (The induced phase shift induced by these time-shifts depends on the frequency by the formula $\Delta\phi = \Delta T * 2 * \pi * f$). Instead of using the SLP-2400 low-pass filter DUT model from the ADS as our true value, we used a benchtop VNA measured S-parameter file in the ADS simulation.

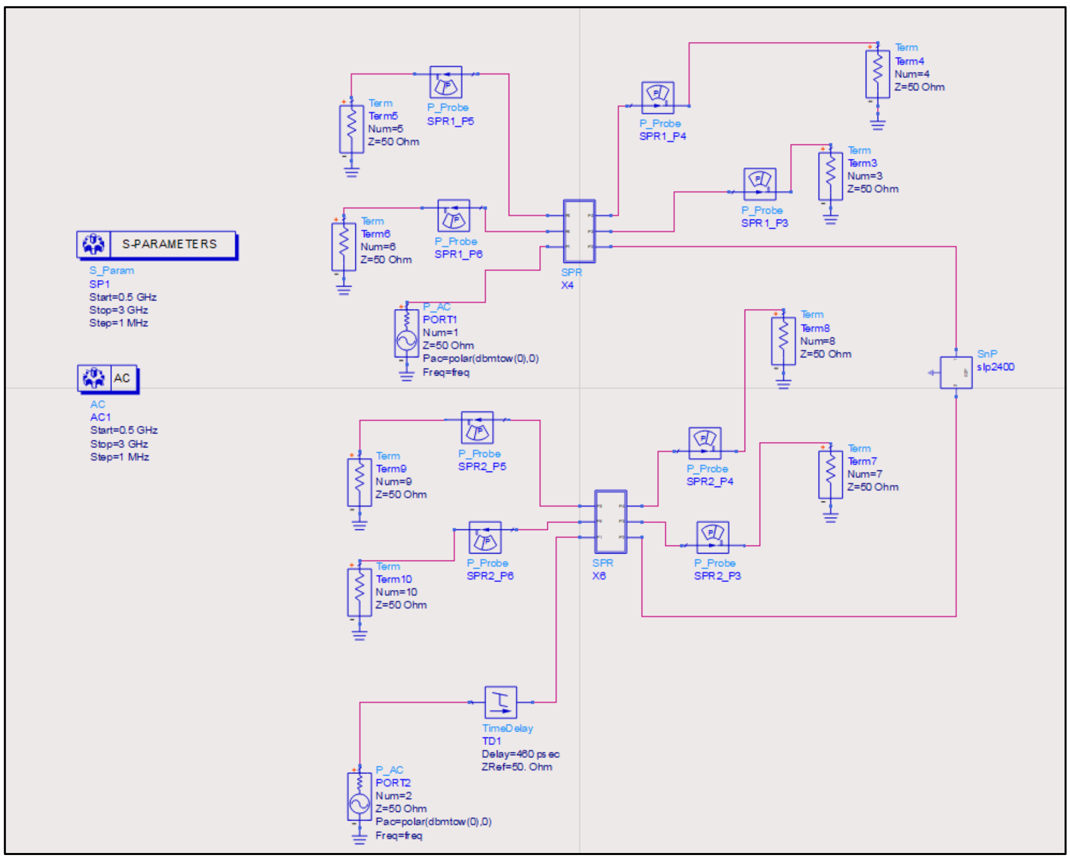

Figure 32: ADS schematic for DSPR-VNA using time delay between the input RF signals

The results are similar to the results we obtained using the direct phase shift in the RF inputs to one SPR. Figure 33 shows the magnitude and phase of our S_{12} results compared with the true S_{12} measured using a benchtop VNA.

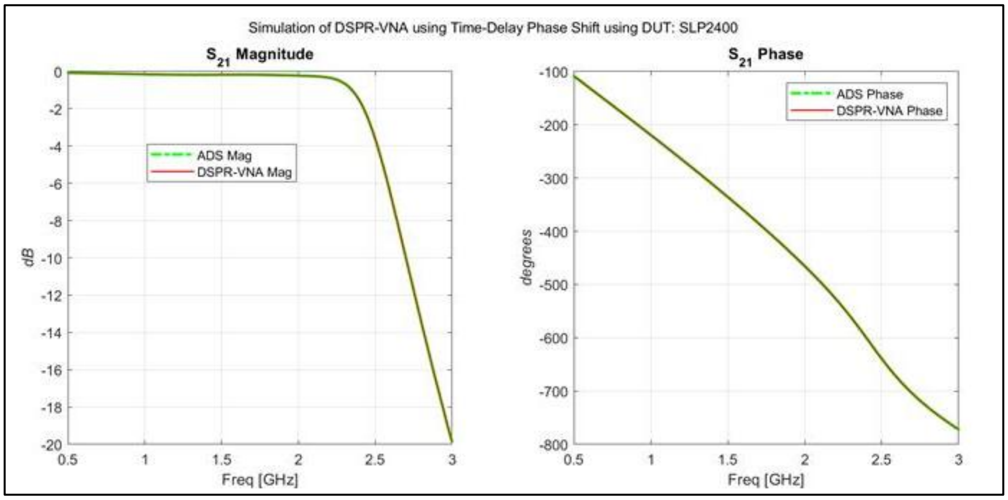

Figure 33: ADS Simulation DSPR-VNA S_12 using SLP2400 DUT with time-delay phase shift

Figure 34 shows the S_{11} of the same setup.

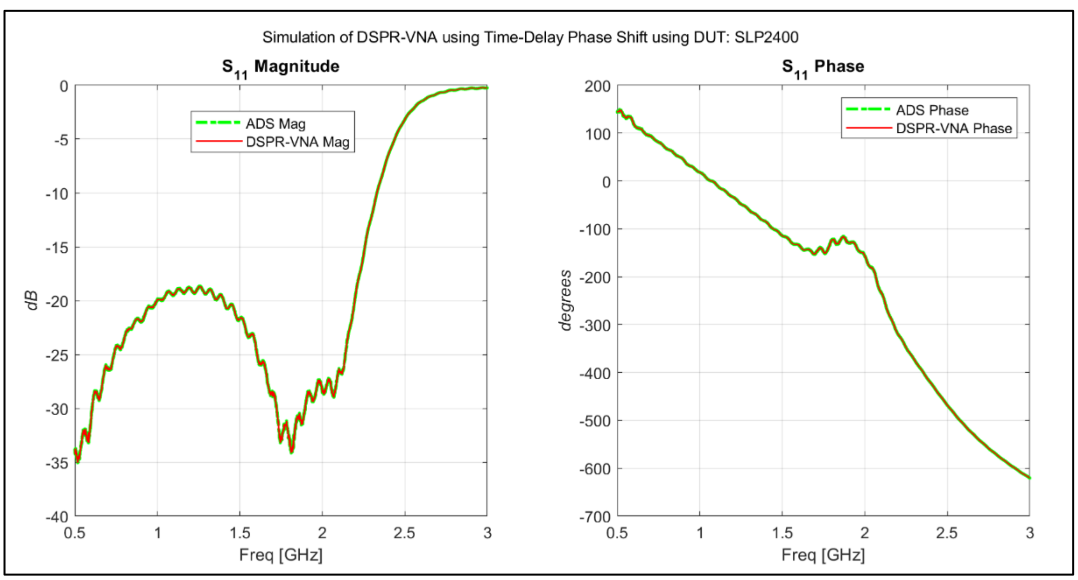

Figure 34: ADS Simulation DSPR-VNA S_11 using SLP2400 DUT with time-delay phase shift

Figure 35 shows the S_{22} of the same setup.

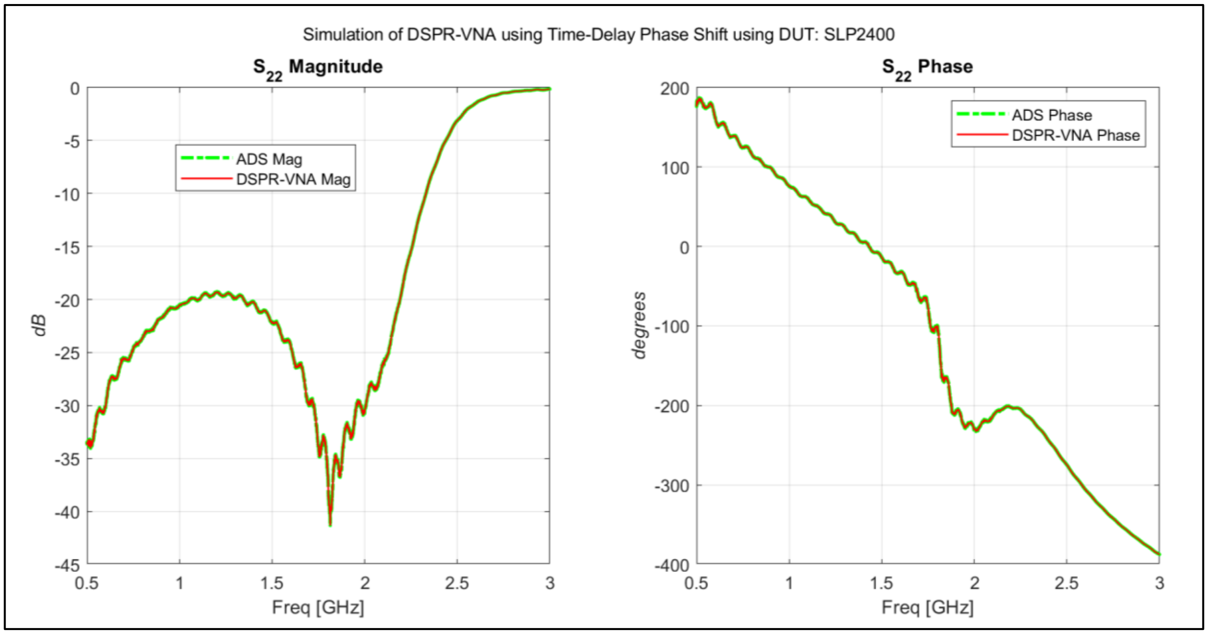

Figure 35: ADS Simulation DSPR-VNA S_22 using SLP2400 DUT with time-delay phase shift

From these results we see a new opportunity for easily shifting the phase between two RF sources of the SPR-VNA or DSPR-VNA. Unlike the conventional way of perhaps using cables of different electrical lengths or using the built-in phase shifters of the benchtop Signal Generators, we can now use a low-cost signal generator and use the time delay introduced by switching one of the signal generators on and off to create the phase-shift between the input signals to create a DSPR-VNA. This would further reduce the cost and complexity of the system when implemented in hardware.

6.3 SPR-VNA Hardware

In this Section we provide results of using two hardware SPRs as described in Section 5.2 with dependent and independent signal generators used as RF power sources to create a hardware SPR-VNA and DSPR-VNA system as implemented via ADS simulation, the results of which have been described in Section 6.1. As we have already described in this thesis, the DSPR-VNA systems have completely independent RF sources while SPR-VNA systems require dependent RF sources (signal generators in our hardware). What we mean by dependent signal generators is that we connect the Local Oscillator (LO) ports of the RF sources (available at the back of the instruments that were used). The point of this was to maintain the same frequency for both instruments as we found that without connecting the LO ports the frequency tended to drift between them. For the independent signal generator case, we attempt to compensate for the frequency drift by making several power measurements at each independent SPR and averaging them over time. The reason for this will be described when the results are presented.

As discussed in previous Chapters, frequency compensated quasi-optimal design was chosen for this project. Two SPRs with independent RF power sources are used for our DSPR-VNA system as discussed in Section 5.1. Since our network analyzer is distributed and both SPRs work independently so we do not need any additional hardware for our DSPR-VNA. Different devices under test include low-pass and high-pass filters and horn antennas to prove potential future use of the current hardware for imaging purposes.

For both dependent and independent RF signal source cases we only report on introducing the phase shift using the programmable phase-shift that was available on one of the signal generator devices. Note that only for the dependent signal generator case was additional hardware, beyond the two SPRs required: the single cable used to stabilize the frequency drift by connecting the local oscillator of one signal generator as reference to other. In the future, this frequency synchronization could be implemented using other wireless techniques.The different devices under test that we show results for, include the previously tested low-pass filters, as well as two horn antennas to prove the potential future use of the current DSPR-VNA hardware for imaging purposes.

As discussed in Section 5.2, based on our observations and comparison of different characterization techniques for our SPR hardware, we will only be using Characterization technique 3 (non-linear optimization) for our results as it has the best performance for our system. We first show the results of tests performed using two separate signal generators with the Local Oscillator connected. We used ‘Agilent Technologies E8267D PSG Vector Signal Generator’ and ‘Agilent N9310 Signal Generator’. A National Instruments PXI 9019 24-port vector network analyzer was used for S-parameter measurement of the SPRs and the DUT as reference. Since we are testing on reciprocal devices we have S_{12} = S_{21}. We used four phase shifts between the two RF inputs by changing the phase of the signal generator connected with the SPR2. Figure 36 shows the results using Mini-Circuits SLP1000 low pass filter as DUT.

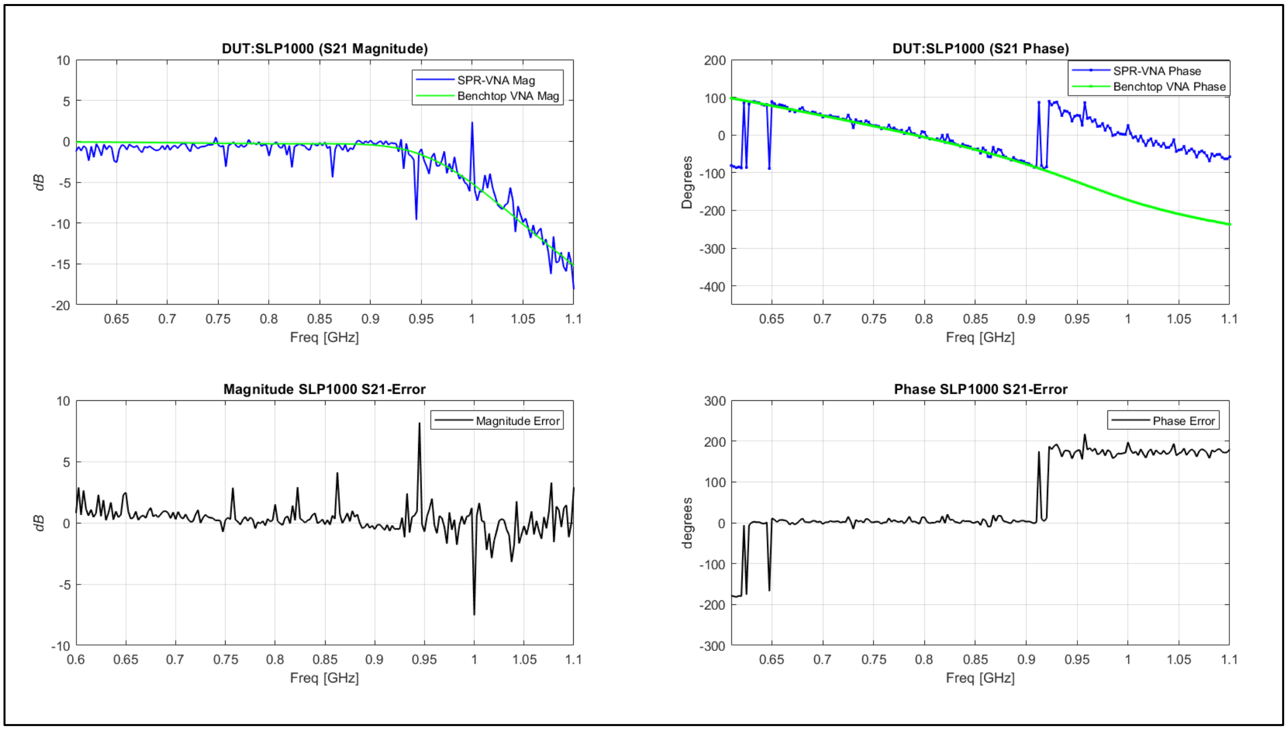

Figure 36: Two SG's with common LO using four phase shifts

As can be readily observed the phase has some systematic errors. There is a jump that looks like an "unwrapping" error, but we found that simply using the MATLAB unwrap command that shifts the phase ±n2π radians for each phase jump that is greater than π-radians did not work. Rather we found it necessary to implement a custom unwrap that introduces a -π radians jump when it detects a jump of π-0.3 or π radians jump when it detects a jump of 0.3–π. Figure 37 shows the results after performing this custom unwrapping of the phase. This jump of π-0.3 radians was determined experimentally and it was found that it is somewhat dependent on the DUT. Future work is required to come up with a robust technique to correct these jumps in phase.

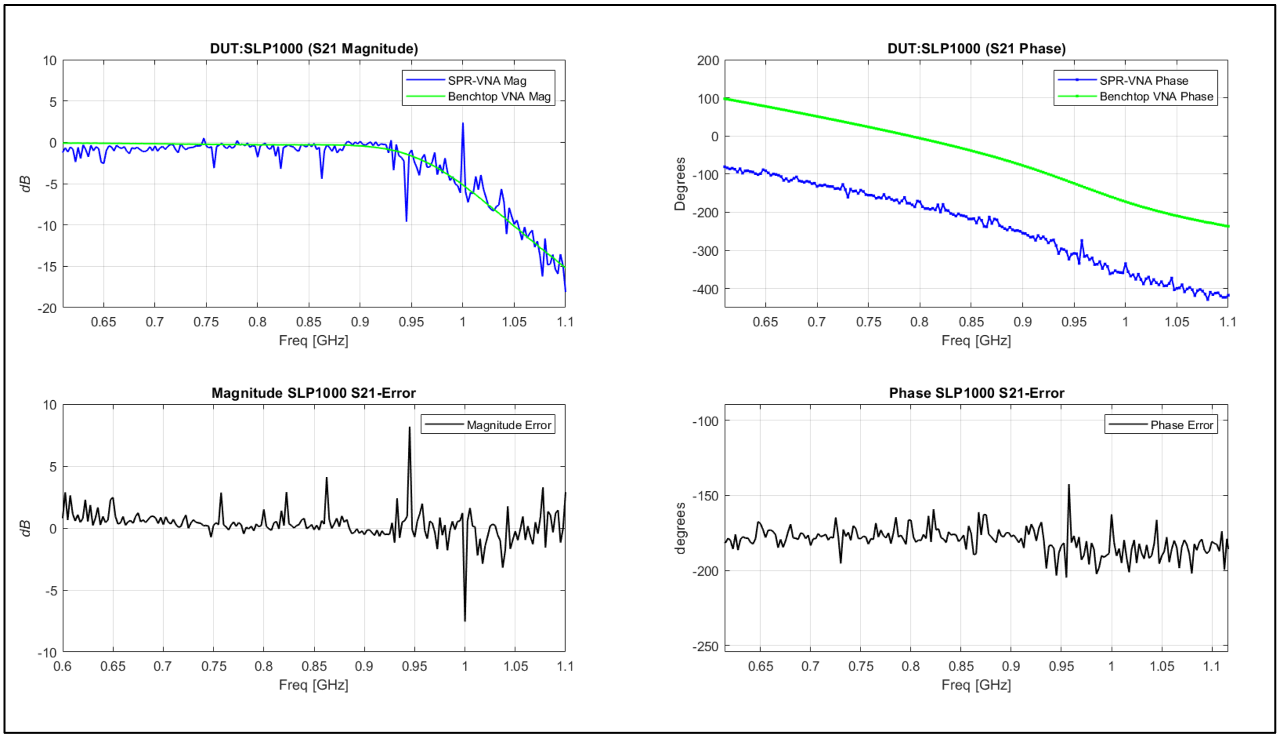

Figure 37: Two SG's with common LO using four phase shifts after phase unwrap

It can be observed that the results are very noisy with a magnitude error of ±10 dB and a phase error of -180 degrees. The phase has an actual offset of 177 degrees. If we fix the offset as shown in Figure 38 we observe that the phase error is within ±30 degrees.

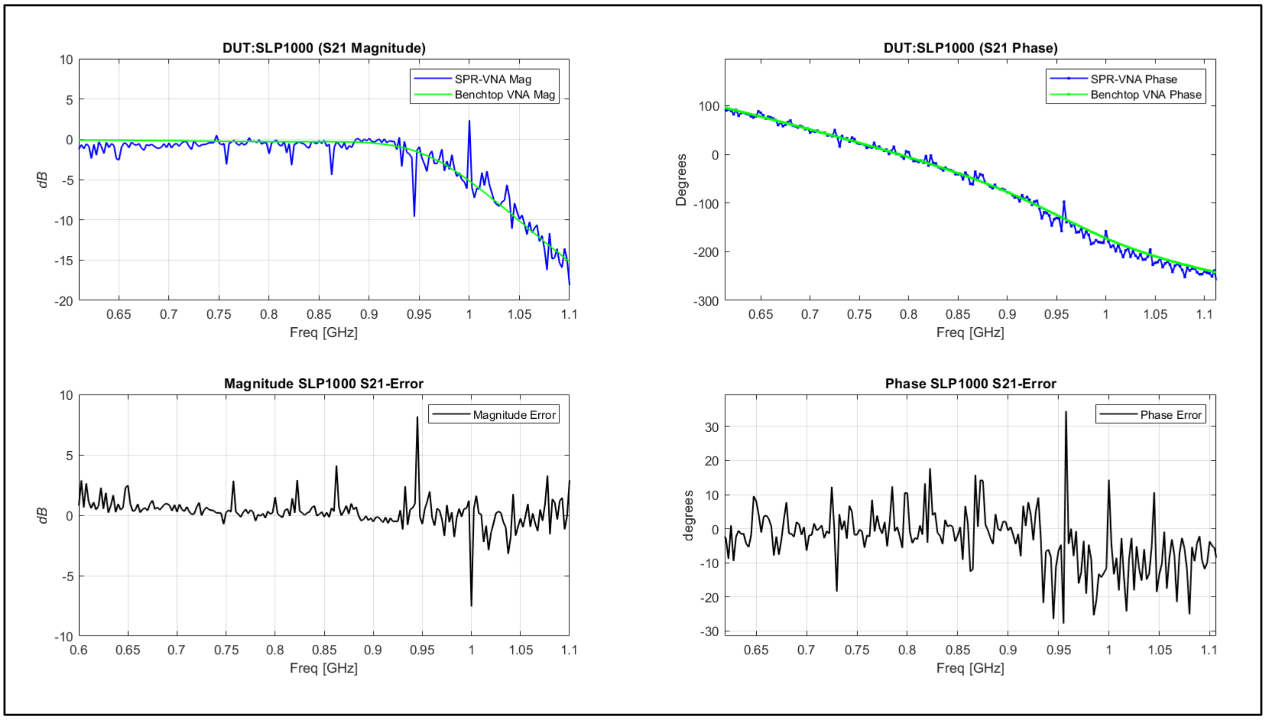

Figure 38: Two SG's with common LO using four phase shifts with phase offset

To investigate the noise in our measurements, and later to measure the frequency drift between two unsynchronized signal generators, we connected an oscilloscope to the output port of one power detector as shown in Figure 39. The detector output was measured at one of the ports 4…6 of the digital oscilloscope. Note that the power detector ports are supposed to be outputting a DC value when there is a stable and matched RF source at the input of both SPRs and DUT connected to each SPR. There will be a difference in the DC values at each port because of differences in the SPR as well as differences in the signal generators. A frequency drift between the RF sources would manifest as an oscillating signal in the difference between the dc signals at the power detector ports.

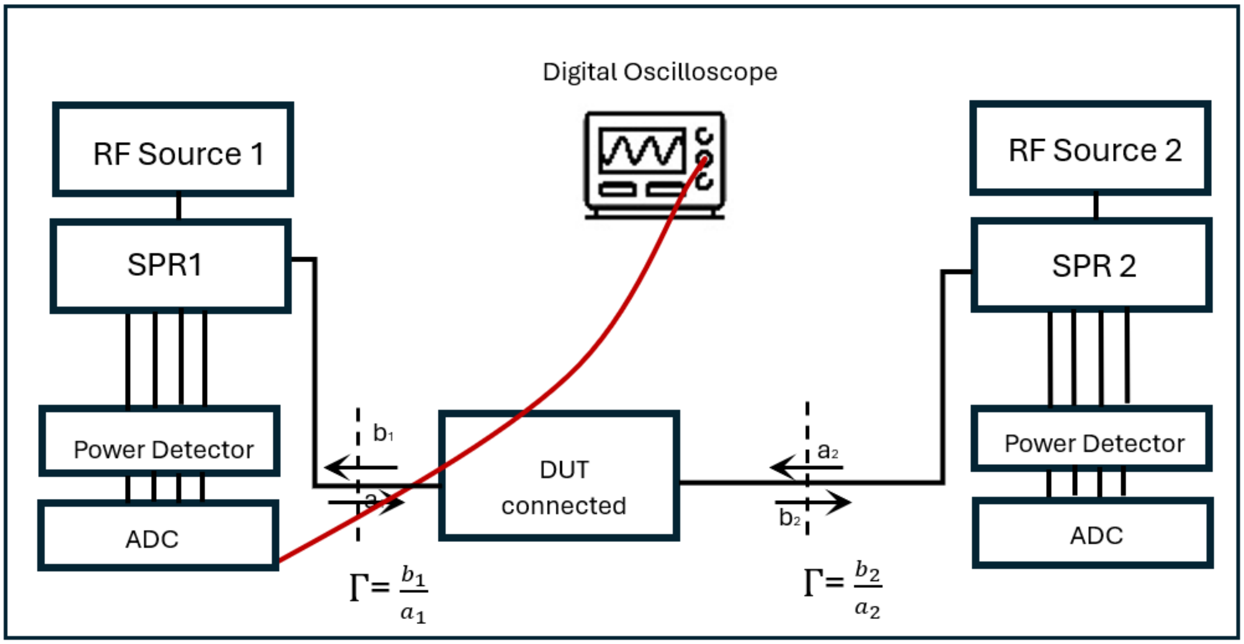

Figure 39: Schematic Diagram of measuring potential frequency drift between two RF sources

Figure 40 shows the voltage being sampled by the ADC converters of the SPRs such that one of the power measurement ports (port-4 in this case) of the SPR1 is probed with the oscilloscope. This can be done for all four power detectors at the ports of the SPR's but for simplicity we just provide the analysis of port 4. This voltage presents the frequency drift in our signal generators. Since the SPRs for Figure 40 have a common LO so we can see some very small noise in the power detector measurement.

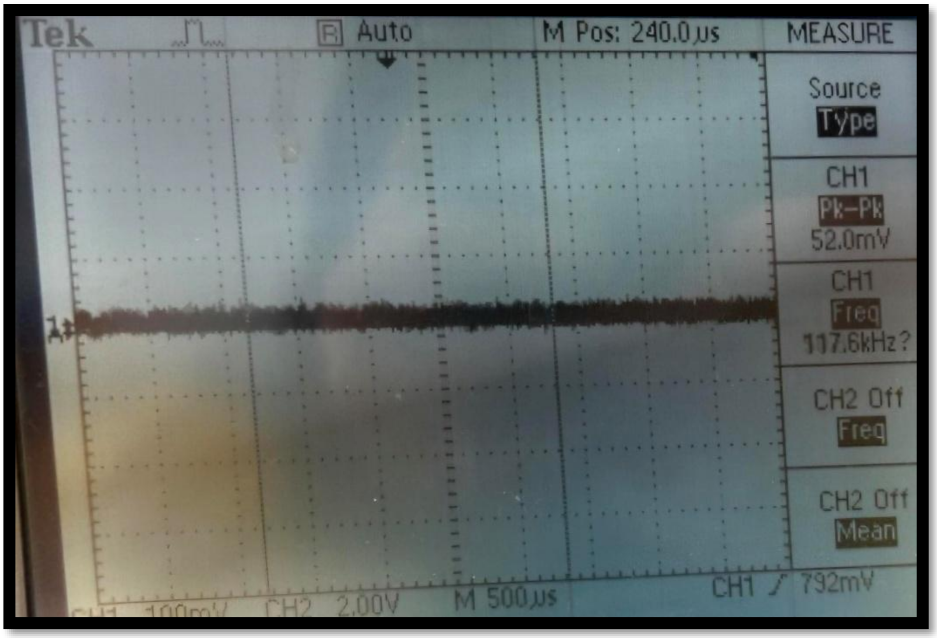

Figure 40: Voltage Difference between two LO connected SG Outputs

Figure 40 shows a 50 mV pk-pk voltage. To account for this 50mVpk-pk voltage between the two signal generators we sample our signal ten times and take the average at each frequency point. The acquisition rate of our system is 3 samples per second.

Figure 41 shows the results with the power at each frequency point averaged by ten samples and using four phase shifts instead of three.

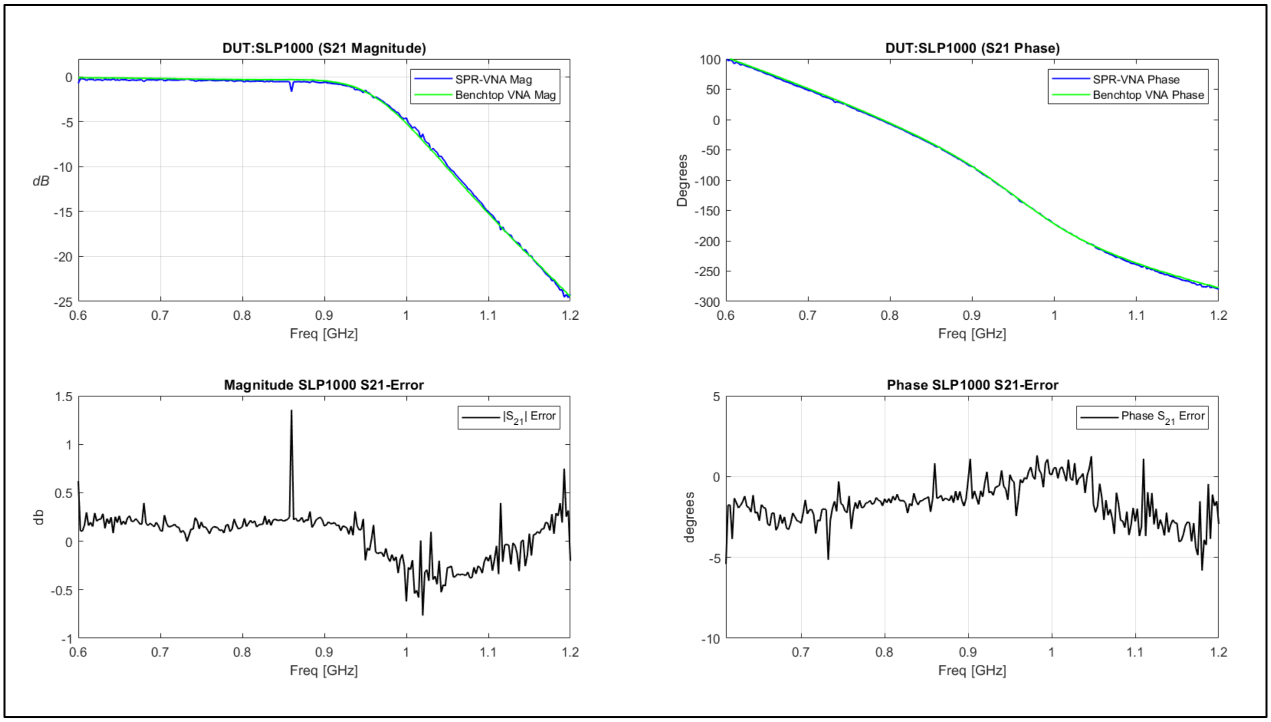

Figure 41: Two SG's with common LO using four phase shifts with average of 10 power samples

From Figure 41 we can observe that the results look promising as compared with Figure 38 in which we were not averaging out 10 powers at each frequency point. It shows the 1.4 dB magnitude error for S_{21} as compared with the benchtop VNA. This error can be reduced using higher number of phase shifts between the two RF inputs and using least-square method to get the optimal result. When we increase the number of phase shifts to 12 (applied by changing the internal phase of the signal generator connected with one SPR) and use the least squares method to solve (4.3), we get a much-improved result. The results from measuring the low-pass filter $S_{21}= S_{12}$ are shown in Figure 42. We can observe an error of only 0.3 dB to -0.5 dB in $|S_{21}|$ (magnitude of S_{21}) and 5-degree error in phase.

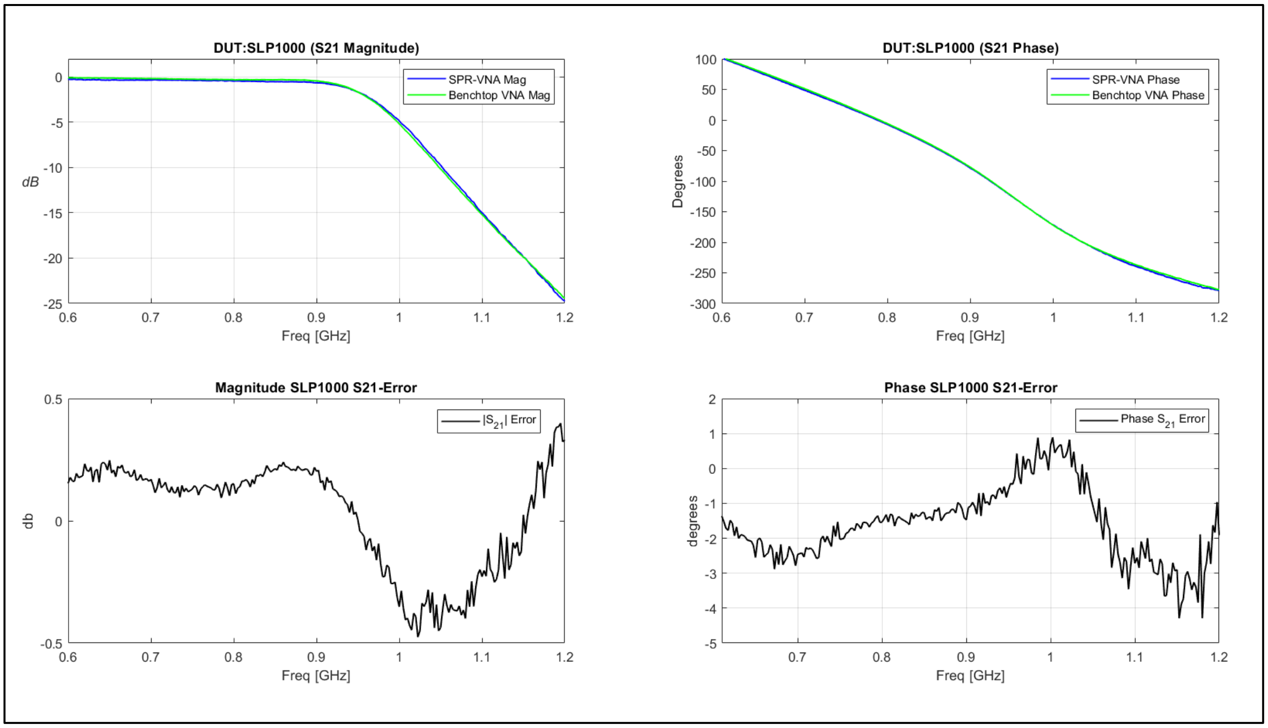

Figure 42: Two Signal Generators with LO Connected SPR-VNA S_21 with 12 phase shifts

Figure 43 shows the S_{11} using the same experimental setup.

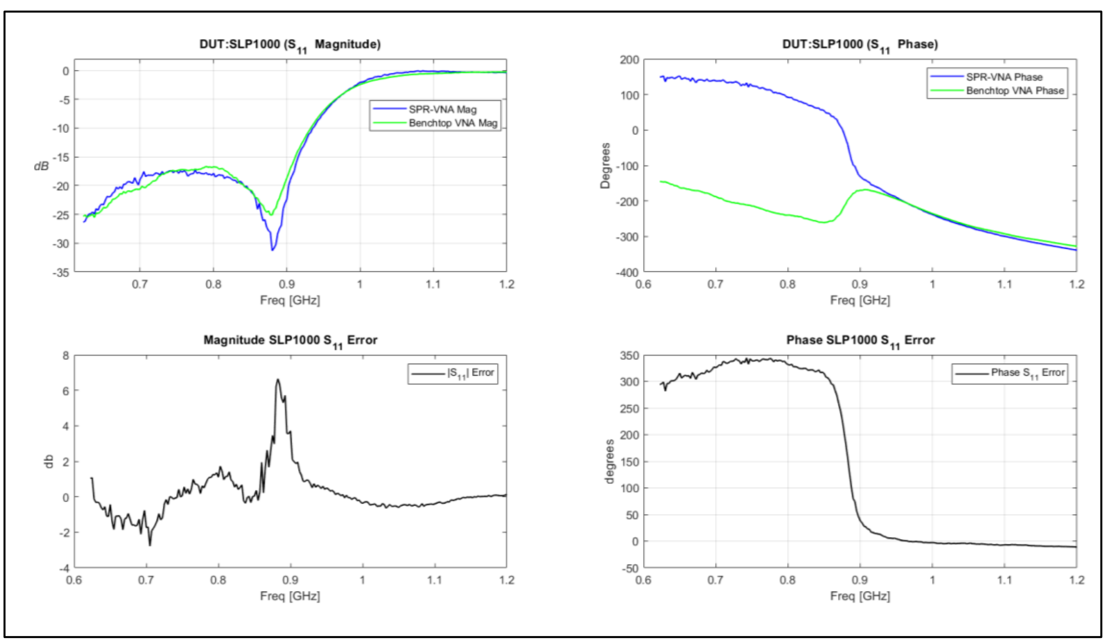

Figure 43: Two Signal Generators with LO Connected SPR-VNA S_11

Figure 44 shows the S_{22} of the low-pass filter with the same experimental setup.

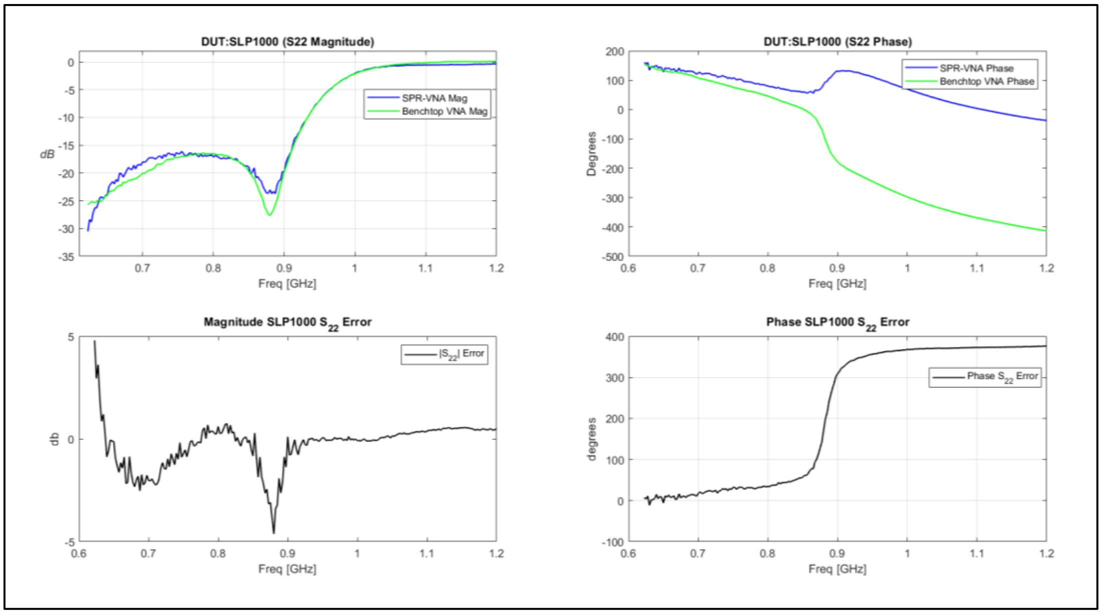

Figure 44: Two Signal Generators with LO Connected SPR-VNA measuring S22

We can observe that the magnitudes of S_{11} and S_{22} have an error of ± 5 dB but the phase are not correct. Also, at lower power levels (less than -20 dB), the magnitudes show more error.

We now turn to our results when using two completely independent signal generators with independent local oscillators (a true Distributed SPR-VNA). We first measured the frequency drift and its impact on our power readings. We used the same process as mentioned in the paragraph above and used an oscilloscope to measure the voltages being sampled by the ADC's of the SPR power measurement board such that one of ADC's port (port 4 in this case) of the SPR1 is connected with the oscilloscope. Figure 45 shows that we have a drift frequency of approximately 500Hz between the two signal generators. To overcome this, we take multiple power measurements at each frequency and average them out to find the average voltage at that frequency.

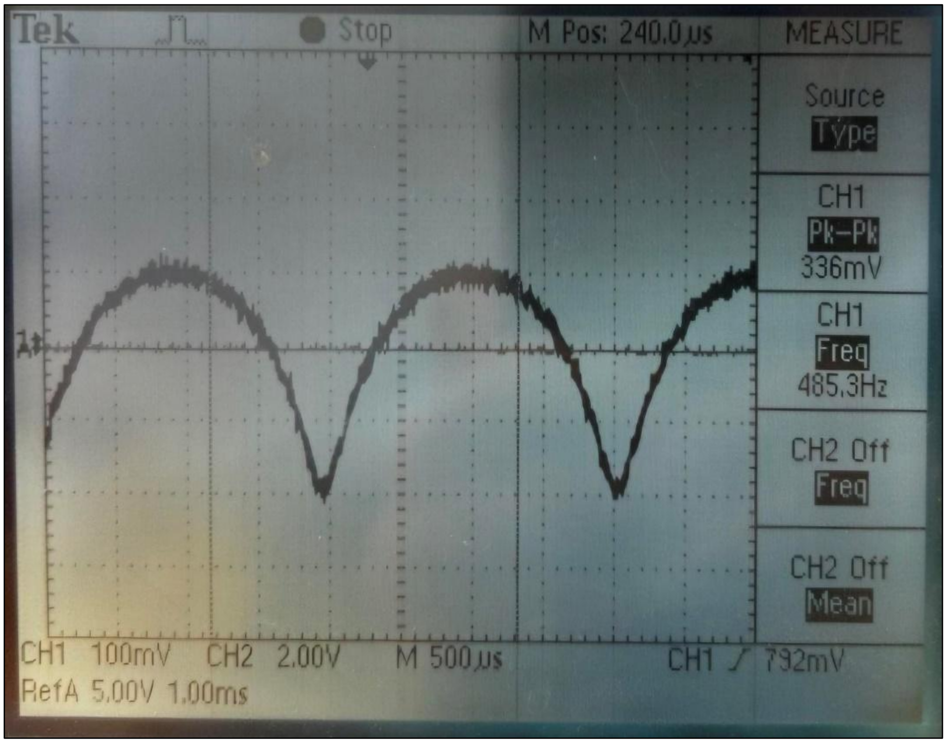

Figure 45: Independent LO noise voltage

Our ADC converter 'MCP3424' has a sample rate of 3.7 samples per second which takes a long time to collect data for averaging the powers at each frequency. Since we can observe a beat frequency of 485Hz between our independent signal generators, we need to average out the powers such that we can measure the power at an average level to overcome the beat frequency noise. We take 1000 samples at each frequency and take the average.

Figure 46 shows the results as compared to a conventional benchtop VNA. Since the simulations have proved that independent signal generators have the capability to closely match the results of LO connected source SPR-VNAs, an ADC converter with a higher sample rate can be used in future to speed up the measurement process and help in noise reduction as well as frequency drift correction.

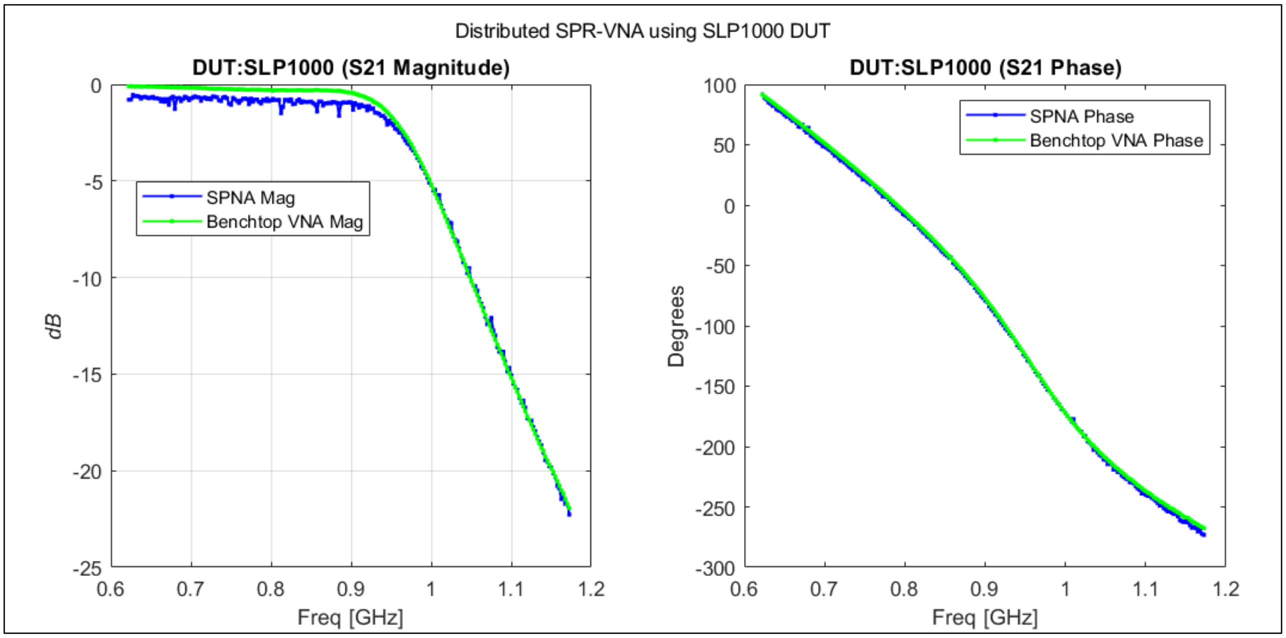

Figure 46: S_{21} completely independent RF power sources

Figure 47 shows the error in S_{21} magnitude is from -0.8 dB to 1.3 dB while the phase error is ±6 degrees.

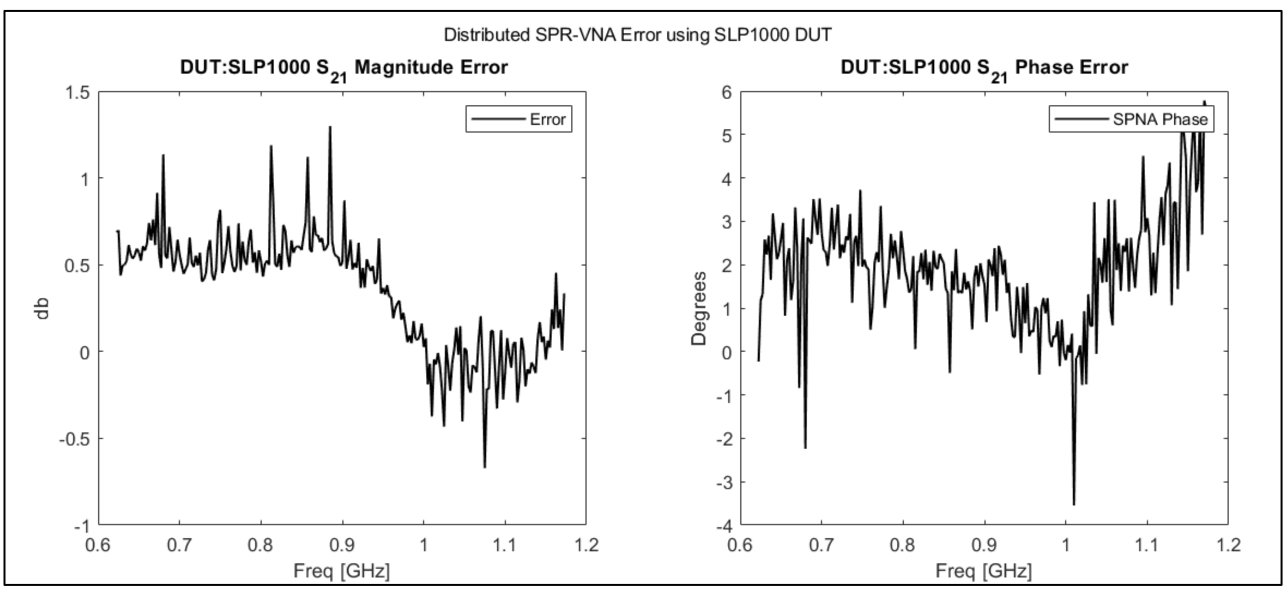

Figure 47: Error in distributed SPR-VNA S_21 Results

Figure 48 shows the magnitude and phase of S_{11} with a magnitude error from ±8 dB and the unwrapped phase error is ±400 degrees.

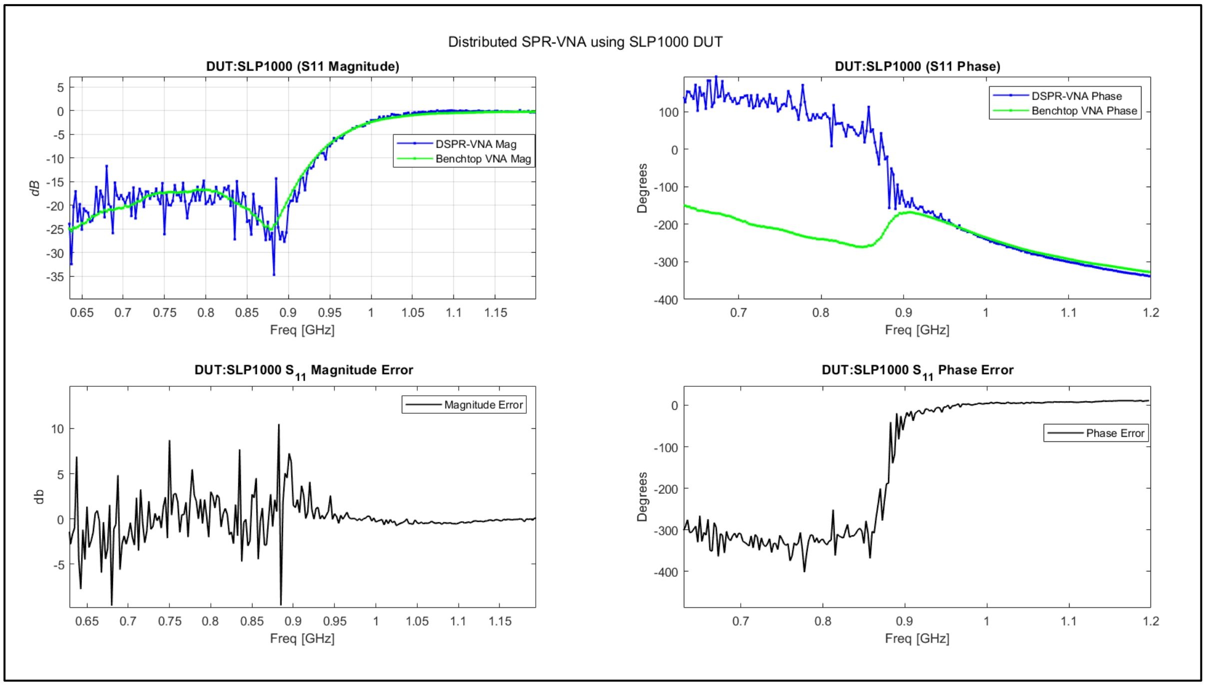

Figure 48: S_{11} Mag and Phase for SLP1000 DUT using DSPR-VNA

Figure 49 shows the magnitude and phase of S_{22} with a magnitude error from ±8 dB and the unwrapped phase error is ±400 degrees.

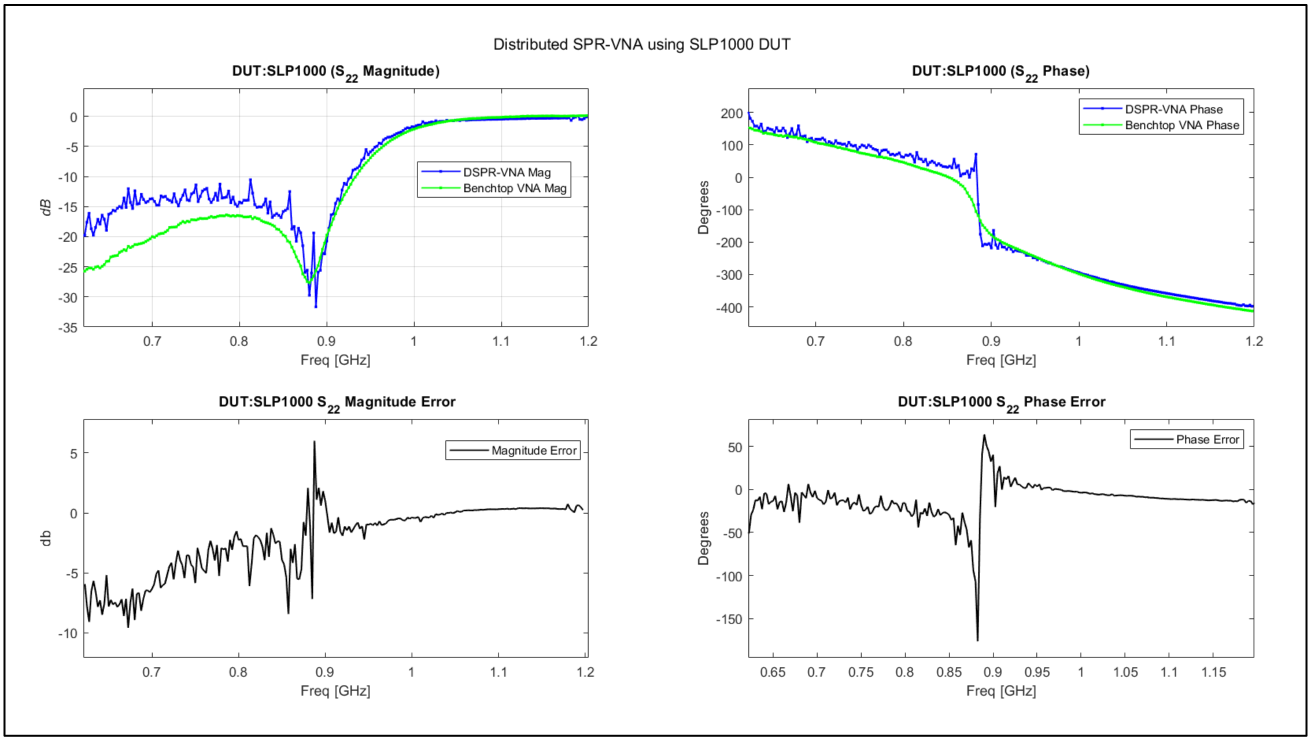

Figure 49: S_{22} Mag and Phase for SLP1000 DUT using DSPR-VNA

6.4 SPR-VNA Microwave Imaging Application

We next tested our SPR-VNA to determine if it is feasible for microwave imaging applications. For this we used two horn antennas (LB-10125-NF Broa dBand Horn Antenna) as DUTs and used a metallic rod as the object to be imaged. The antennas were placed 12 inches apart. The rod was placed between them in the center. It is important to note that our RF input signal connected with both the SPRs has a common LO. As we are not using a truly distributed SPR-VNA. We used 12 phase shifts for each frequency and averaged 10 power measurements as we explained in Section 6.3. Figure 50 shows the comparison between the measurements of SPR-VNA and the benchtop VNA for the two horn antennas when no rod was placed between them. This is referred to as the incident field measurement. We can notice that the error between the measurements taken from a commercial benchtop VNA, and our hardware is ±1 dB in magnitude and 50 degrees in phase which is promising for the potential use.

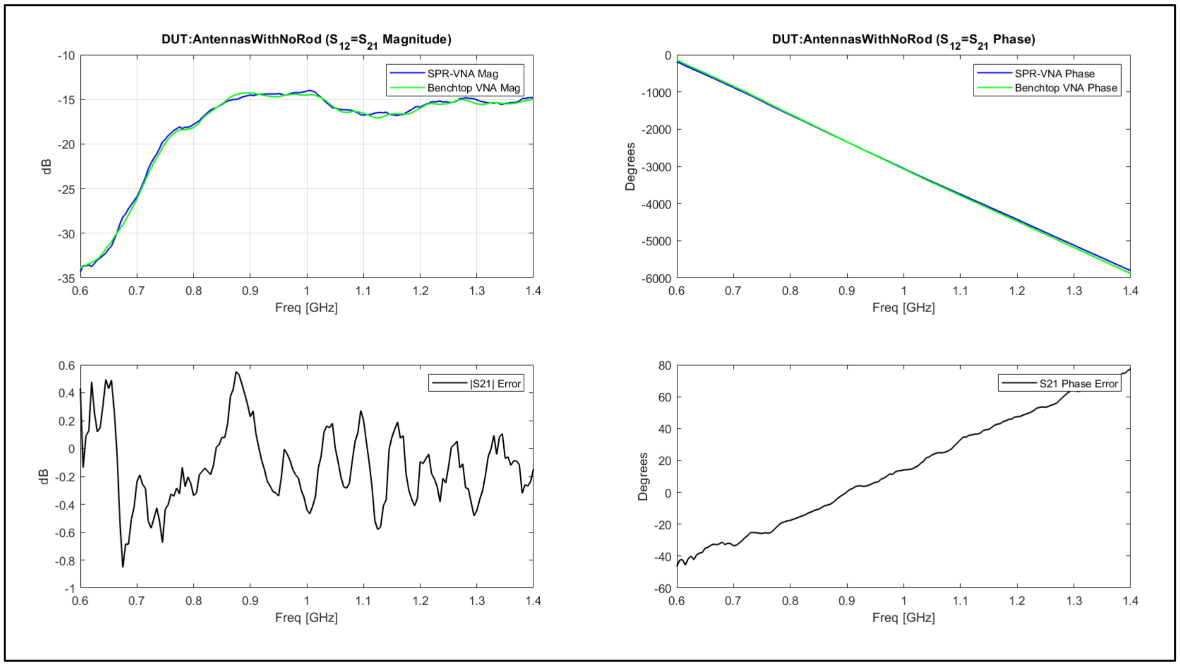

Figure 50: Comparison of SPR-VNA with a benchtop VNA using two Horn antennas

We then tested the same setup with a metallic rod placed between the two horn antennas. This is referred to as the total field measurement in imaging applications. Figure 51 shows the magnitude and phase comparison of S_{12}.

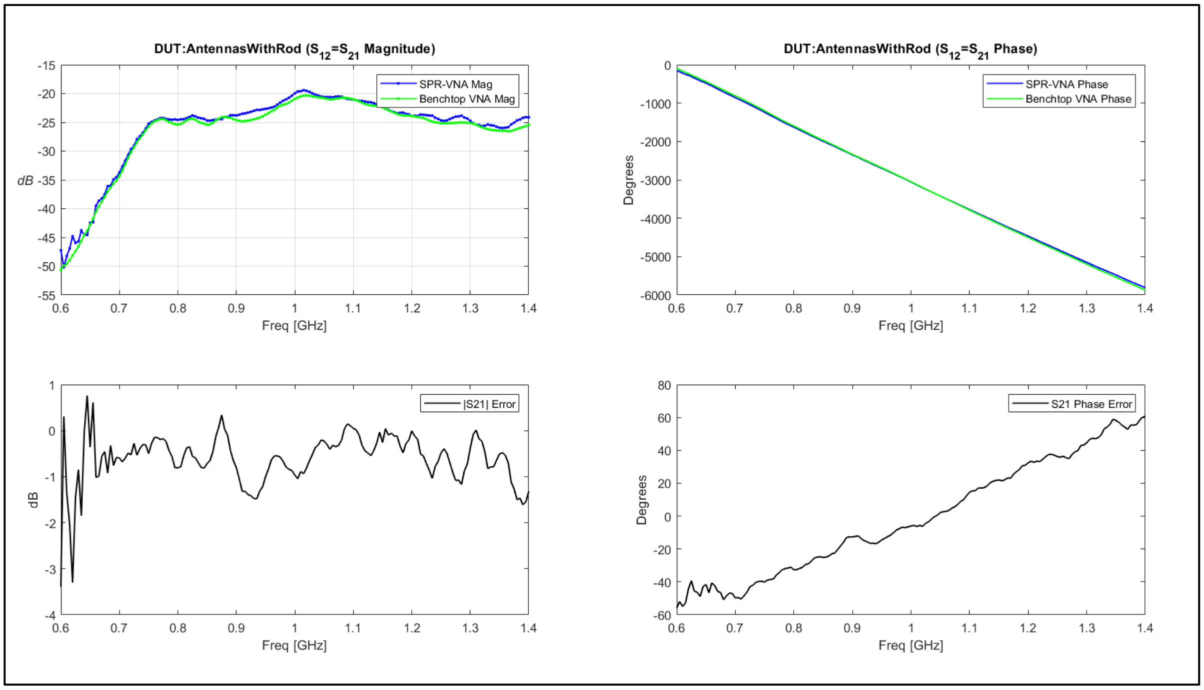

Figure 51: Comparison between SPR-VNA and Conventional VNA S_12 using two horn antennas with a metallic object

The difference between measurement made with and without the metallic rod are referred to as the scattered-field measurements. The scattered field measurements, using a benchtop VNA and the SPR-VNA, are shown in Figure 52. It is the scattered field measurements that are used in microwave imaging techniques. Figure 52 the use of an SPR-VNA shows promising results in its potential in imaging applications.

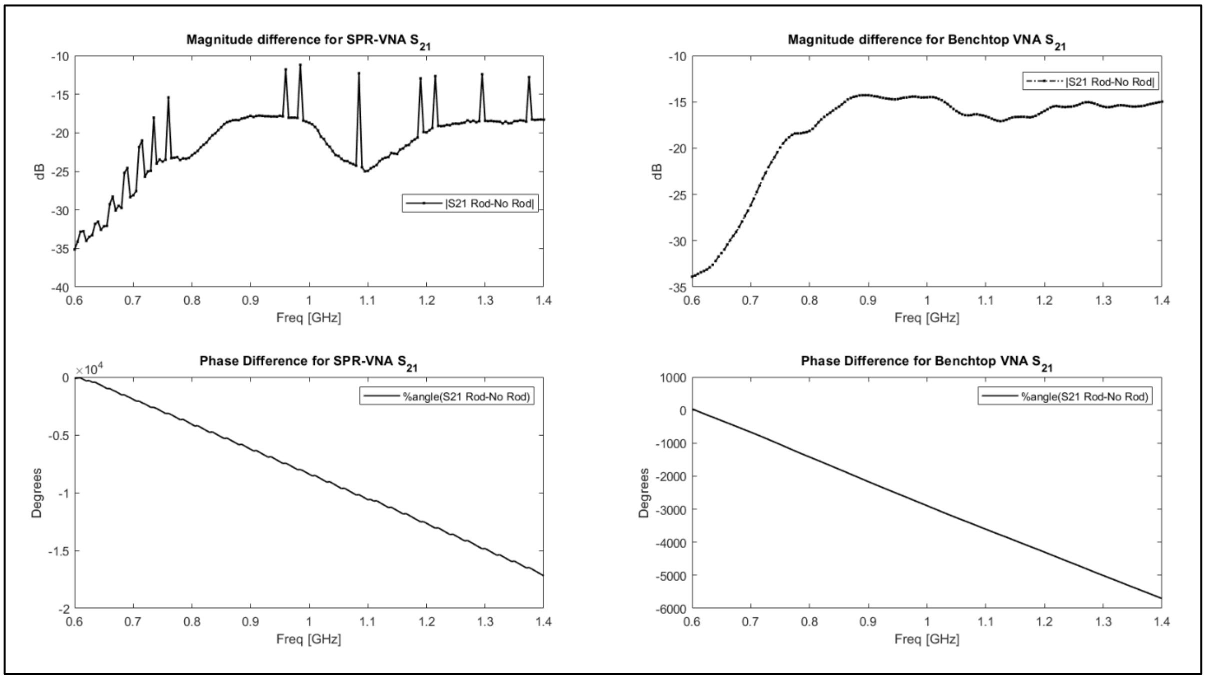

Figure 52: Comparing difference between measurements with and without rod using conventional VNA and SPR-VNA

7 Conclusion and Future Work:

This thesis presents two significant contributions to the field of microwave measurements and network analysis. The primary achievement is the worlds-first proof-of-concept non-linked SPR-VNA working to measure the S_{21}'s of microwave devices with no direct connection between each port of the device. Additionally, the thesis offers a comprehensive evaluation of various measurement techniques and introduces characterization methods for determining the full scattering parameters of a DUT. The comparative analysis of multiple characterization and calibration techniques provides valuable insights into their relative performance and applicability. Furthermore, the successful application of the distributed SPR-VNA to S-parameter measurements between two antennas opens up new possibilities in microwave imaging applications. These contributions collectively advance the state-of-the-art in microwave measurement technology, offering improved methodologies for accurate and efficient network analysis in various fields of application.

The hardware development of a low-cost power measurement board for six-port reflectometers using logarithmic voltage detectors and ADC converters is also a significant contribution since the board is much more affordable than the RF power detectors available in the market.

The future work on this thesis might be focused on improvement of measurement techniques for transmission co-efficients so the phase detection can be more precise. Also, the current system is not portable because we are using benchtop signal generators as RF input, these can be replaced with compact RF synthesizers available in the market which would further reduce the cost. Additionally, a high sample rate ADC would improve the results as discussed before, also saving the data collection time. This new distributed network analyzer has created opportunities for cable-free measurement of the S-parameters of any long-distance antenna setup or imaging chambers where a lot of cables are used for connecting them with a switching matrix.

A Appendix

A.1 Basic Components in a SPR

The two most important parts of the six-port reflectometer are the Wilkinson power dividers and the quadrature hybrid couplers [4].

The Wilkinson power divider is a passive three-port device in microwave engineering, designed for power division and combining [4]. Its basic schematic consists of an input port (port 1) connected to two output ports (ports 2 and 3) through quarter-wave transmission lines. These lines have a characteristic impedance of $\sqrt{2} \cdot Z0$, where Z0 is the system impedance (typically 50Ω). A key feature of the Wilkinson divider is the 100Ω resistor connecting the two output ports. This resistor serves two important functions:

1. It provides isolation between the output ports, minimizing crosstalk.

2. It ensures that all three ports remain matched when operating at the design frequency.

The device operates by splitting an input signal from port 1 into two equal-amplitude, in-phase outputs at ports 2 and 3. The quarter-wave transformers match the split ports to the common port, while the resistor enables port matching and isolation. The scattering matrix for a 2-way Wilkinson power divider at the design frequency is:

$$[S] = \frac{-j}{\sqrt{2}} \begin{bmatrix} 0 & 1 & 1 \\ 1 & 0 & 0 \\ 1 & 0 & 0 \end{bmatrix}$$

The Wilkinson power divider achieves excellent performance in terms of matching, isolation, and power division, making it a versatile component in various RF and microwave applications.

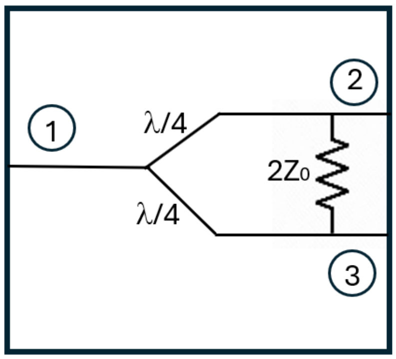

Figure A1: Wilkinson Power Divider

The quadrature hybrid coupler is a four-port passive microwave device typically constructed using microstrip transmission lines [1]. Its basic layout consists of four quarter-wavelength (λ/4) sections:

- Two sections with characteristic impedance Z0 (usually 50Ω)

- Two sections with characteristic impedance Z0/√2

Figure A2 shows the geometry of a quadrature hybrid coupler.

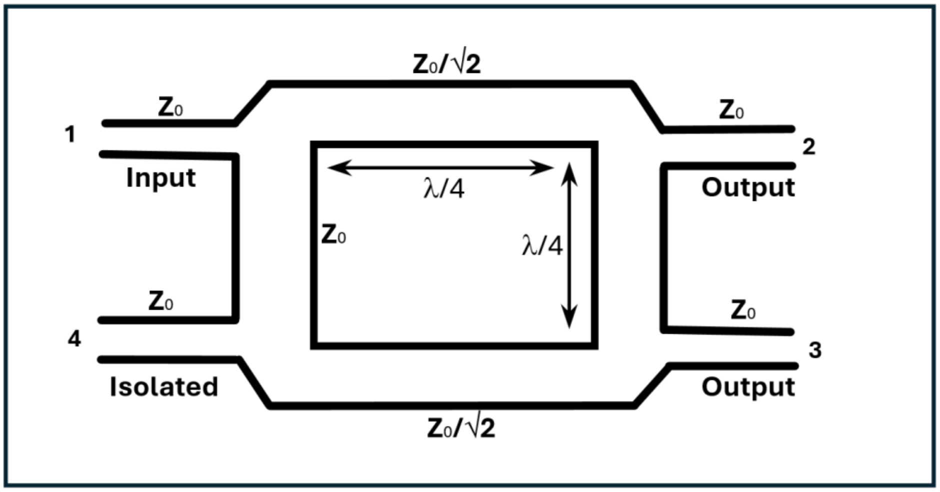

Figure A2: Geometry of a Quadrature Hybrid Coupler

These transmission line sections are arranged in a ring configuration, with each port connected to a line of impedance Z0. The device evenly splits input power between two output ports. It introduces a 90° phase difference between the two output signals. High isolation is maintained between the input and isolated port. Any port can serve as the input, with the device maintaining its operational characteristics. All ports are matched to the system impedance (typically 50Ω) when properly terminated. When all ports are matched, the usual configuration consists of an input port 1, 2 output ports between which the power is equally divided with a phase shift of 90 degree between them. No power is coupled to port 4 known as isolated port. For an ideal quadrature hybrid, the scattering matrix is:

$$[S] = \frac{-1}{\sqrt{2}} \begin{bmatrix} 0 & j & 1 & 0 \\ j & 0 & 0 & 1 \\ 1 & 0 & 0 & j \\ 0 & 1 & j & 0 \end{bmatrix}$$

This matrix illustrates the device's key properties, including equal power division, 90° phase shift, and port isolation. Their ability to provide equal power division with a precise phase shift makes them invaluable in many microwave circuit designs, particularly those requiring balanced signal processing or phase manipulation. Directional couplers separate the incident and reflected power waves which help us in our application in six-port junctions.

A.2 Graphical relationship between q_i and C_i points

The q_i depend only on the S-parameters of the designed six-port circuit. The transformation to the centers of the circles, C_i, is applied uniformly to each of the q_i. This means that if we want to keep the centers equally spaced on an equilateral triangle in the complex plane, we have the ability to do that by making sure the original q_i are so placed. We explore some graphical scenarios using MATLAB. Considering equation (2.49) for the relation between C_i and q_i, we keep the value of k_i and radius constant and increase the $|q_i|$. Figure A3 shows the comparison between different values of C_i and q_i, while we increase the magnitude of q_i. It can be observed that there is a uniform relation between the C_i and q_i points.

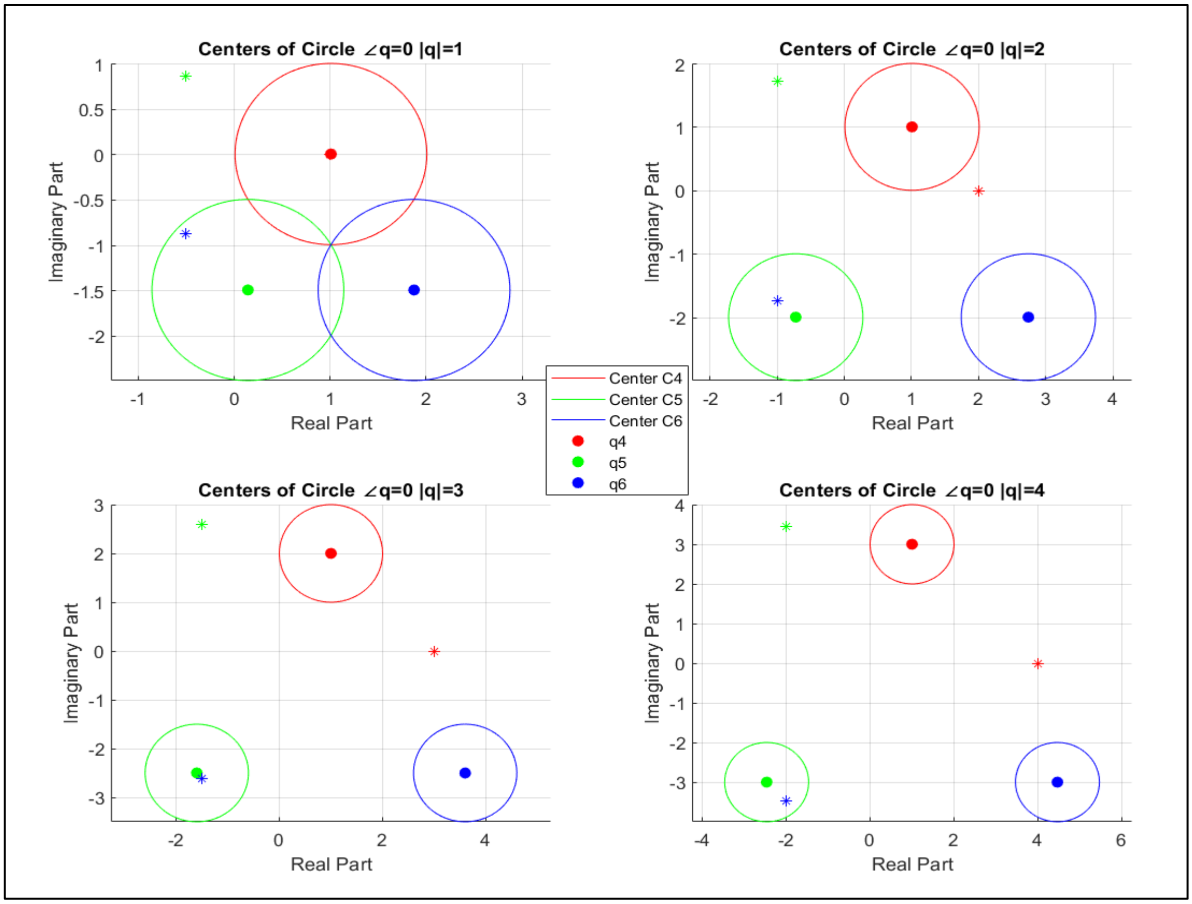

Figure A3: Changin the magnitude of qi points to observe impact on Ci

Figure A4 shows the impact of changing phase of q_i, it can be observed that the circles rotate with the same phase as q_i points.

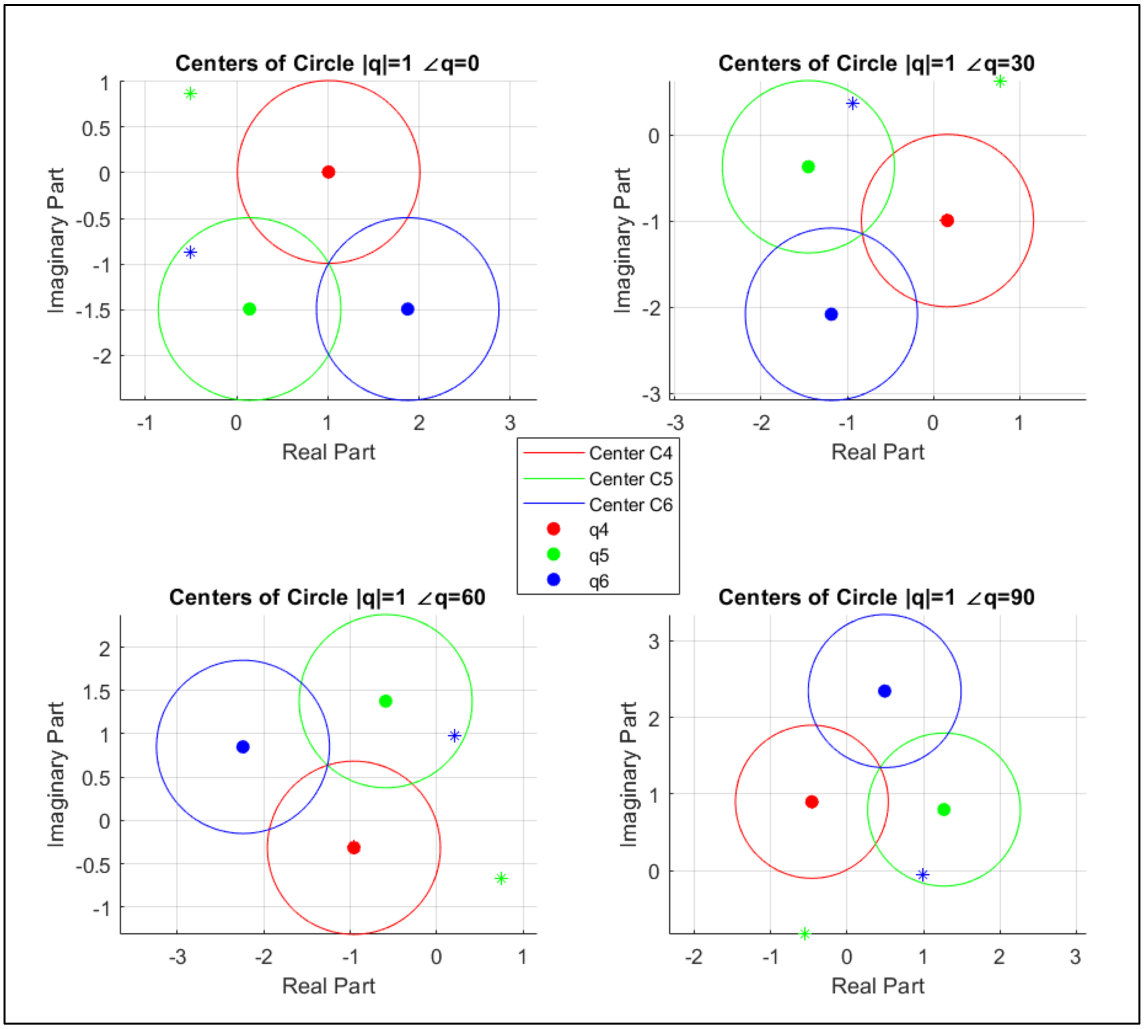

Figure A4: Changin the phase of qi points to observe impact on Ci

Hence we can conclude that the relation between C_i and q_i points is uniform. It only enlarges or compresses, and rotates the triangle based on the measurements of the DUT (via k). This leads to the design criteria for the six-port circuit.

A.3 Literature Review of Six-Port Measurement techniques, hardware and applications

Table 1 shows some prominent six-port architecture, applications and characterization techniques:

Year	**Frequency**	**Calibration Technique**	**Hardware**	**Application**
1983 [59]	18-40ghz	9loads and bi-linear transformation	mm Wave SPR	Microwave applications
1999[60]	1.3-3GHz	5loads and bilinear transformation	MMIC based SPR	Reflection coefficient measurement at microwave frequency
2002 [61]	X-band (8-12GHz)	9 load calibration	Rectangular waveguide and Schottky diodes.	High Power applications
2010 [63]	Xband,8-12 GHz	9 phase shifts followed by bilinear transformation	Waveguide SPR and Schottky diodes	Single spr based network analyzer
2016 [64]	24 GHz	Multiple distance measurements with least squares Levenberg-Marquardt	MIC surface mount	Distance measurement radar
2016 [65]	2-18GHz	Novel algorithm based on real-valued time-delay neural networks	The implemented hardware includes a six-port correlator,	Demodulating wideband IQ signals

		(RVTDNN)		
2019 [66]	60GHz	8load calibration, Fourier analysis and non-linear optimization	MMIC	Time difference of arrival
2022 [67]	2.6-3.8 GHz	Even-odd mode analysis	2 SPRs and a ring power divider MMIC fabrication	S-parameters

References

[1] D. M. Pozar, “Microwave Engineering, 4th Edition,” *John Wiley &Sons, Inc*, pp. 1–756, 2012, Accessed: Dec. 15, 2024. [Online]. Available: https://www.wiley.com/en-ca/Microwave+Engineering%2C+4th+Edition-p-9780470631553

[2] Saif Aboud, “Six-Port Reflectometer Based Vector Network Analyzer with Two Independent RF Power Sources,” University of Manitoba, WINNIPEG, 2022.

[3] “Distributed Modular 2-port Vector Network Analyzer ME7868A | Vector Network Analyzers | Anritsu Asia Pacific.” Accessed: Dec. 15, 2024. [Online]. Available: https://www.anritsu.com/en-au/test-measurement/products/me7868a

[4] Fadhel M.Gannouchi and Abbas Mohammadi, *The Six-Port Technique with Microwave and Wireless Applications | Artech eBooks | IEEE Xplore*. 2009. Accessed: Nov. 15, 2024. [Online]. Available: https://ieeexplore.ieee.org/book/9100382

[5] C. A. Hoer, “The Six-Port Coupler: A New Approach to Measuring Voltage, Current, Power, Impedance, and Phase,” *IEEE Trans Instrum Meas*, vol. 21, no. 4, pp. 466–470, 1972, doi: 10.1109/TIM.1972.4314068.

[6] G. F. Engen and C. A. Hoer, “Application of an Arbitrary 6-Port Junction to Power-Measurement Problems,” *IEEE Trans Instrum Meas*, vol. 21, no. 4, pp. 470–474, 1972, doi: 10.1109/TIM.1972.4314069.

[7] C. A. Hoer, “A Network Analyzer Incorporating Two Six-Port Reflectometers,” *IEEE Trans Microw Theory Tech*, vol. 25, no. 12, pp. 1070–1074, 1977, doi: 10.1109/TMTT.1977.1129276.

[8] G. F. Engen, “An Improved Circuit for Implementing the Six-Port Technique of Microwave Measurements,” *IEEE Trans Microw Theory Tech*, vol. 25, no. 12, pp. 1080–1083, 1977, doi: 10.1109/TMTT.1977.1129278.

[9] F. M. Ghannouchi et al. and R. G. Bosisio, “A Wideband Millimeter Wave Six-Port Reflectometer Using Four Diode Detectors Calibrated Without a Power Ratio Standard,” *IEEE Trans Instrum Meas*, vol. 40, no. 6, pp. 1043–1046, 1991, doi: 10.1109/19.119791.

[10] G. F. Engen, “Calibrating the Six - Port Reflectometer by Means of Sliding Terminations,” *IEEE Trans Microw Theory Tech*, vol. 26, no. 12, pp. 951–957, 1978, doi: 10.1109/TMTT.1978.1129527.

[11] C. A. Hoer and K. C. Roe, “Using an Arbitrary Six-Port Junction to Measure Complex Voltage Ratios,” pp. 98–99, Mar. 1975, doi: 10.1109/MWSYM.1975.1123294.

[12] J. Li, R. G. Bosisio, and K. Wu, “Dual-tone calibration of six-port junction and its application to the six-port direct digital millimetric receiver,” *IEEE Trans Microw Theory Tech*, vol. 44, no. 1, pp. 93–99, 1996, doi: 10.1109/22.481390.

[13] S. Qayyum and R. Negra, “Compact six-port junction using broadside-coupled CPW couplers for a broa dBand six-port receiver,” *European Microwave Week 2017: “A Prime Year for a Prime Event”, EuMW 2017 - Conference Proceedings; 47th European Microwave Conference, EuMC 2017*, vol. 2017-January, pp. 347–350, Dec. 2017, doi: 10.23919/EUMC.2017.8230866.

[14] W. Zhang, A. Hasan, F. M. Ghannouchi et al., M. Helaoui, Y. Wu, and Y. Liu, "Concurrent dual-band receiver based on novel six-port correlator for wireless applications," *IEEE Access*, vol. 5, pp. 25826–25834, Oct. 2017, doi: 10.1109/ACCESS.2017.2768364.

[15] J. Li, R. G. Bosisio, and K. Wu, "Collision avoidance radar using six-port phase/frequency discriminator (SPFD)," *Proceedings of the IEEE National Telesystems Conference*, pp. 55–58, 1994, doi: 10.1109/NTC.1994.316694.

[16] D. Roscoe and R. G. Bosisio, "A Direction-Finding Antenna System Using an Integrated Six-Port Circuit," *IEEE Trans Antennas Propag*, vol. 43, no. 12, pp. 1508–1512, 1995, doi: 10.1109/8.475948.

[17] S. Sun, Y. Wu, M. Li, W. Zhang, Y. Liu, and S. Huang, "A novel wideband six-port correlator with filter-integration and DC-block functions," *IEEE International Symposium on Electromagnetic Compatibility*, vol. 2017-October, pp. 1–4, Jan. 2018, doi: 10.1109/EMC-B.2017.8260417.

[18] F. M. Ghannouchi et al., R. G. Bosisio, and Y. Demers, "Load-pull characterization method using six-port techniques," pp. 536–539, 1989, doi: 10.1109/IMTC.1989.36918.

[19] V. Bilik, V. Raffaj, and J. Bezek, "New extremely wideband lumped six-port reflectometer," *Conference Proceedings - European Microwave Conference*, vol. 2, no. 20, pp. 1473–1478, 1990, doi: 10.1109/EUMA.1990.336275.

[20] F. Wiedmann, B. Huyart, E. Bergeault, and L. Jallet, "New structure for a six-port reflectometer in monolithic microwave integrated-circuit technology," *IEEE Trans Instrum Meas*, vol. 46, no. 2, pp. 527–530, 1997, doi: 10.1109/19.571902.

[21] X. T. Fang, X. C. Zhang, and C. M. Tong, "A novel miniaturized micro-strip six-port junction," *Progress In Electromagnetics Research Letters*, vol. 23, pp. 129–135, 2011, doi: 10.2528/PIERL11032302.

[22] B. Neumeyer, "A New Analytical Method for Complete Six-Port Reflectometer Calibration," *IEEE Trans Instrum Meas*, vol. 39, no. 2, pp. 376–379, 1990, doi: 10.1109/19.52518.

[23] U. Stumper, "Finding Initial Estimates Needed for the Engen Method of Calibrating Single Six-Port Reflectometers," *IEEE Trans Microw Theory Tech*, vol. 38, no. 7, pp. 946–949, 1990, doi: 10.1109/22.55790.

[24] C. Akyel, F. M. Ghannouchi et al., and M. Caron, "A New Design for High-Power Six-Port Reflectometers Using Hybrid Stripline/Waveguide Technology," *IEEE Trans Instrum Meas*, vol. 43, no. 2, pp. 316–321, 1994, doi: 10.1109/19.293441.

[25] H. How, T. M. Fang, C. Vittoria, and R. Schmidt, "Design of Six-Port Stripline Ferrite Junction Circulators," *IEEE Trans Microw Theory Tech*, vol. 42, no. 7, pp. 1272–1275, 1994, doi: 10.1109/22.299767.

[26] J. R. Juroshek and C. A. Hoer, "A Dual Six-Port Network Analyzer Using Diode Detectors," *IEEE Trans Microw Theory Tech*, vol. 32, no. 1, pp. 78–82, 1984, doi: 10.1109/TMTT.1984.1132615.

[27] H. M. Cronson and L. Susman, "DUAL SIX-PORT AUTOMATIC NETWORK ANALYZER.," *IEEE MTT-S International Microwave Symposium Digest*, pp. 434–436, 1980, doi: 10.1109/MWSYM.1980.1124312.

[28] H. M. Cronson and L. Susman, "A Six-Port Automatic Network Analyzer," *MTT-S International Microwave Symposium Digest*, vol. 77, pp. 50–52, 1977, doi: 10.1109/MWSYM.1977.1124354.

[29] L. Kaliouby and R. G. Bosisio, "A New Method for Six-Port Swept Frequency Automatic Network Analysis," *IEEE Trans Microw Theory Tech*, vol. 32, no. 12, pp. 1678–1681, 1984, doi: 10.1109/TMTT.1984.1132926.

[30] G. F. Engen and C. A. Hoer, "Thru-Reflect-Line: An Improved Technique for Calibrating the Dual Six-Port Automatic Network Analyzer," *IEEE Trans Microw Theory Tech*, vol. 27, no. 12, pp. 987–993, 1979, doi: 10.1109/TMTT.1979.1129778.

[31] J. R. Juroshek and C. A. Hoer, "A High-Power Automatic Network Analyzer for Measuring the RF Power Absorbed by Biological Samples in a TEM Cell," *IEEE Trans Microw Theory Tech*, vol. 32, no. 8, pp. 818–824, 1984, doi: 10.1109/TMTT.1984.1132777.

[32] D. Woods, "Analysis and calibration theory of the general 6-port reflectometer employing four amplitude detectors," *Proceedings of the Institution of Electrical Engineers*, vol. 126, no. 2, pp. 221–228, 1979, doi: 10.1049/PIEE.1979.0051.

[33] N. A. El-Deeb, "On the Use of a Microstrip Three-Line System as a Six - Port Reflectometer," *IEEE Trans Microw Theory Tech*, vol. 27, no. 10, pp. 847–853, 1979, doi: 10.1109/TMTT.1979.1129747.

[34] A. L. Cullen and S. P. Yeo, "Six-port reflectometer theory for symmetrical five-port junction with directional coupler," *IEE Proceedings H (Microwaves, Antennas and Propagation)*, vol. 133, no. 4, pp. 277–287, 1986, doi: 10.1049/IP-H-2.1986.0049.

[35] M. Malkomes, R. Walsdorf, and H. J. Schmitt, "INTEGRATED FIN-LINE 6-PORTS FOR mm-WABVE NETWORK ANALYZERS.," *Proceedings of the Colloquium on Microwave Communication*, pp. 259–260, 1986, doi: 10.1109/MWSYM.1986.1132277.

[36] S. K. Judah and A. S. Wright, "Second generation dual six-port network analyser.," *IEEE MTT-S International Microwave Symposium Digest*, vol. 1988, pp. 295–296, 1988, doi: 10.1109/MWSYM.1988.22034.

[37] I. Ohta, "A New Six-Port Microwave Network: Six-Port Magic Junction," *IEEE Trans Microw Theory Tech*, vol. 36, no. 5, pp. 859–864, 1988, doi: 10.1109/22.3605.

[38] M. Berman, P. I. Somlo, and M. J. Buckley, "A Comparative Statistical Study of some Proposed Six-Port Junction Designs," *IEEE Trans Microw Theory Tech*, vol. 35, no. 11, pp. 971–977, 1987, doi: 10.1109/TMTT.1987.1133794.

[39] G. P. Riblet and E. R. B. Hansson, "Aspects of the Calibration of a Single Six-Port Using a Load and Offset Reflection Standards," in *MTT-S International Microwave Symposium Digest*, MTT005, 1982, pp. 316–318. doi: 10.1109/MWSYM.1982.1130704.

[40] G. Riddels and V. F. Fusco, "A quasilumped six-port reflectometer for cellular radio use," *Microw Opt Technol Lett*, vol. 4, no. 5, pp. 191–194, Apr. 1991, doi: 10.1002/MOP.4650040506.

[41] D. J. Bannister, J. P. Ide, and M. Perkins, "Improved six-port reflectometer based on symmetrical five-port junction," *Electron Lett*, vol. 28, no. 4, pp. 406–408, 1992, doi: 10.1049/EL:19920255.

[42] C. M. Potter and G. Hjipieris, “Robust six- to four-port reduction algorithm,” *IEEE MTT-S International Microwave Symposium Digest*, vol. 3, pp. 1263–1266, 1993, doi: 10.1109/MWSYM.1993.277103.

[43] I. T. Sylla, R. Hajji, and F. M. Ghannouchi et al., “CAD of an integrated six-port reflectometer in MMIC technology,” *Canadian Conference on Electrical and Computer Engineering*, vol. 2, pp. 1170–1172, 1995, doi: 10.1109/CCECE.1995.526670.

[44] A. M. Affandi and A. M. Rushdi, “Accurate six-port microstrip reflectometer,” *SBMO/IEEE MTT-S International Microwave and Optoelectronics Conference Proceedings*, vol. 2, pp. 563–568, 1995, doi: 10.1109/SBMOMO.1995.509680.

[45] C. Y. Lee *et al.*, “Enhanced five-port ring circuit reflectometer for synthetic breast tissue dielectric determination,” *Progress In Electromagnetics Research C*, vol. 69, pp. 83–95, 2016, doi: 10.2528/PIERC16081302.

[46] S. Julrat and S. Trabelsi, “Portable six-port reflectometer for determining moisture content of biomass material,” *IEEE Sens J*, vol. 17, no. 15, pp. 4814–4819, Aug. 2017, doi: 10.1109/JSEN.2017.2718659.

[47] K. Staszek, A. Rydosz, E. Maciak, K. Wincza, and S. Gruszczynski, “Six-port microwave system for volatile organic compounds detection,” *Sens Actuators B Chem*, vol. 245, pp. 882–894, Jun. 2017, doi: 10.1016/J.SNB.2017.01.194.

[48] D. Kissinger, B. Laemmle, I. Nasr, and R. Weigel, “Millimeter-wave integrated reflectometer architectures for biomedical applications,” *BioWireleSS 2013 - Proceedings: 2013 IEEE Topical Conference on Biomedical Wireless Technologies, Networks, and Sensing Systems - 2013 IEEE Radio and Wireless Week, RWW 2013*, pp. 61–63, 2013, doi: 10.1109/BIOWIRELESS.2013.6613675.

[49] S. Z. Ibrahim, M. S. Razalli, W. F. Hoon, and M. N. A. Karim, “Six-Port interferometer for direction-of-Arrival detection system,” *ISSE 2016 - 2016 International Symposium on Systems Engineering - Proceedings Papers*, Nov. 2016, doi: 10.1109/SYSENG.2016.7753161.

[50] K. Fujiwara, K. Tokita, M. Yoshida, and T. Yakabe, “Transmission Coefficient Measurement Based on Six-port Correlator in 28-GHz-band,” *2022 24th International Microwave and Radar Conference, MIKON 2022*, 2022, doi: 10.23919/MIKON54314.2022.9924995.

[51] Barakat Rabih, “Measurement techniques of scattering parameters based on six-port technology for microwave applications - Espace ETS,” ETS, 2022. Accessed: Nov. 15, 2024. [Online]. Available: https://espace.etsmtl.ca/id/eprint/2999/

[52] A. K. Sahoo and K. Rawat, “Full 2-Port Vector Network Analyzer using Nonlinear Calibration of Six-Port Reflectometer,” *2019 IEEE MTT-S International Wireless Symposium, IWS 2019 - Proceedings*, May 2019, doi: 10.1109/IEEE-IWS.2019.8803965.

[53] K. Haddadi, M. M. Wang, D. Glay, and T. Lasri, “Performance of a compact dual six-port millimeter-wave network analyzer,” *IEEE Trans Instrum Meas*, vol. 60, no. 9, pp. 3207–3213, Sep. 2011, doi: 10.1109/TIM.2011.2124690.

[54] C. A. Hoer, “Using six-port and eight-port junctions to measure active and passive circuit parameters:,” Gaithersburg, MD, 1975. doi: 10.6028/NBS.TN.673.

[55] J. D. Hunter and P. I. Somlo, "An Explicit Six-Port Calibration Method using Five Standards," *IEEE Trans Microw Theory Tech*, vol. 33, no. 1, pp. 69–72, 1985, doi: 10.1109/TMTT.1985.1132950.

[56] "How can I find the points at which two circles intersect? - Mathematics Stack Exchange." Accessed: Dec. 15, 2024. [Online]. Available: https://math.stackexchange.com/questions/256100/how-can-i-find-the-points-at-which-two-circles-intersect

[57] K. Haddadi and T. Lasri, "Formulation for complete and accurate calibration of six-port reflectometer," *IEEE Trans Microw Theory Tech*, vol. 60, no. 3 PART 1, pp. 574–581, Mar. 2012, doi: 10.1109/TMTT.2011.2181861.

[58] "AD8313 Datasheet and Product Info | Analog Devices." Accessed: Dec. 15, 2024. [Online]. Available: https://www.analog.com/en/products/ad8313.html

[59] F. M. Ghannouchi et al. and R. G. Bosisio, "A Wideband Millimeter Wave Six-Port Reflectometer Using Four Diode Detectors Calibrated Without a Power Ratio Standard," *IEEE Trans Instrum Meas*, vol. 40, no. 6, pp. 1043–1046, 1991, doi: 10.1109/19.119791.

[60] F. Wiedmann, B. Huyart, E. Bergeault, and L. Jallet, "A new robust method for six-port reflectometer calibration," *IEEE Trans Instrum Meas*, vol. 48, no. 5, pp. 927–931, Oct. 1999, doi: 10.1109/19.799649.

[61] Vladmir Bilik, "SIX-PORT MEASUREMENT TECHNIQUE : PRINCIPLES , IMPACT , APPLICATIONS," Bratislava: Radioelektronica, May 2002.

[62] Colin Gilmore, Mohammad Asefi, Jitendra Paliwal, Joe LoVetri, Industrial scale electromagnetic grain bin monitoring, Computers and Electronics in Agriculture, Volume 136, 2017, Pages 210-220, ISSN 0168-1699

[63] M. A. Abou-Khousa, M. A. Baumgartner, S. Kharkovsky, and R. Zoughi, "Novel and simple high-frequency single-port vector network analyzer," *IEEE Trans Instrum Meas*, vol. 59, no. 3, pp. 534–542, Mar. 2010, doi: 10.1109/TIM.2009.2024701.

[64] K. Staszek, S. Linz, F. Lurz, S. Mann, R. Weigel, and A. Koelpin, "Improved calibration procedure for six-port based precise displacement measurements," *WiSNet 2016 - Proceedings, 2016 IEEE Topical Conference on Wireless Sensors and Sensor Networks*, pp. 60–63, Mar. 2016, doi: 10.1109/WISNET.2016.7444322.

[65] W. Zhang, A. Hasan, F. M. Ghannouchi et al., M. Helaoui, Y. Wu, and Y. Liu, "Novel Calibration Algorithm of Multiport Wideband Receivers Based on Real-Valued Time-Delay Neural Networks," *IEEE Trans Microw Theory Tech*, vol. 64, no. 11, pp. 3540–3548, Nov. 2016, doi: 10.1109/TMTT.2016.2604809.

[66] C. Loyez, M. Bocquet, and K. Haddadi, "A 60-GHz Six-port system for localization based on Time Difference Of Arrival," in *2019 IEEE Radio and Wireless Symposium (RWS)*, IEEE, Jan. 2019, pp. 1–4. doi: 10.1109/RWS.2019.8714390.

[67] R. Barakat, "Measurement techniques of scattering parameters based on six-port technology for microwave applications," École de technologie supérieure, Montreal, 2022.